PSI - BESCHLEUNIGER HEUTE UND MORGEN

U.Schryber, PSI Paul Scherrer Institut
CH - 5232 VILLIGEN, Schweiz

Zusammenfassung

Die PSI-Beschleunigeranlage wurde für hohe Protonenströme konzipiert zur Erzeugung intensiver Pionen- und Muonenstrahlen. Die Beschleunigung der Protonen erfolgt in einer ersten Stufe in einem der beiden Injektorzyklotrons 1 oder 2 auf eine Energie von 72 MeV, dann im Ringzyklotron auf die Endenergie von 590 MeV. Die Anlage wird routinemässig mit Strömen von 250 µA betrieben. Die Strahlverluste im Ringzyklotron sind praktisch vernachlässigbar; dies dank der erstmals in einem Zyklotron angewendeten Flattop - Beschleunigung.

Neben der kern- und teilchenphysikalischen Nutzung wird die Anlage in zunehmendem Masse für Untersuchungen in der Festkörperphysik (µSR-Experimente), in der Medizin (Behandlung von Tumoren mit Pionen und Protonen) und die Isotopenproduktion verwendet. Mit der geplanten Spalationsneutronenquelle SINQ wird in Zukunft der "Abfallstrahl" nach den Targetstationen E und M für Neutronenstreuexperimente genutzt. Die SINQ wird 1994 in Betrieb gesetzt.

Die SINQ bedingt Protonenströme > 1 mA, was den Ausbau des Ringzyklotrons [1] [2] und den Neuaufbau der Targetstation E voraussetzt. Die Target M wurde bereits 1985 an die zukünftigen Verhältnisse angepasst. Der Schwerpunkt des Ring-Ausbauprogramms, welches sich über mehrere Jahre erstreckt, ist die Erhöhung der verfügbaren Hochfrequenzleistung von 800 kW auf total 2400 kW.

Der Injektor 1 mit seinen hervorragenden Eigenschaften als Quelle polarisierter Protonen und Deuteronen ist nach wie vor die Basis für ein reichhaltiges Niederenergie-Experimentierprogramm. Die Ergänzung des Injektors 1 durch eine ECR-Quelle, wodurch die Beschleunigung schwerer Jonen ermöglicht würde, steht gegenwärtig zur Diskussion.

[1] W. Joho, Proceedings of the 11th. Int. Conf. on Cyclotrons and their Applications, Tokyo 1986, p.31
[2] U. Schryber, Proceedings of the 12th. Int. Conf. on Cyclotrons and their Applications, Berlin 1989, to be published.

Die Spallationsquelle:
ein Instrument für die Physik der kondensierten Materie

W.E. Fischer, Paul Scherrer Institut
CH – 5232 Villigen PSI, Schweiz

Abstract: Der Bericht beschreibt die am PSI im Bau befindliche Spallations-Neutronenquelle mit ihrem wissenschaftlichen Potential und umreisst die Entwicklungen zur Leistungssteigerung auf dem Gebiet der kalten Neutronen.

1. Einleitung

Das Prinzip eines Neutronen-Streuexperimentes zur Untersuchung von Anregungszuständen in kondensierter Materie ist aus Abb. 1a ersichtlich.
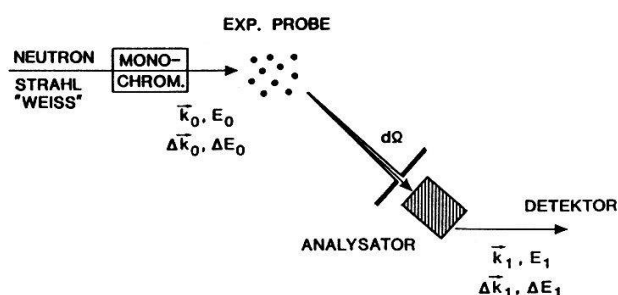

$$\vec{Q} = \vec{k}_0 - \vec{k}_1$$
$$h\omega = E_0 - E_1$$

$$\frac{d^2\sigma}{d\Omega dE_1} = \frac{k_1}{k_0} S(\vec{Q}, \omega)$$

Abb. 1a
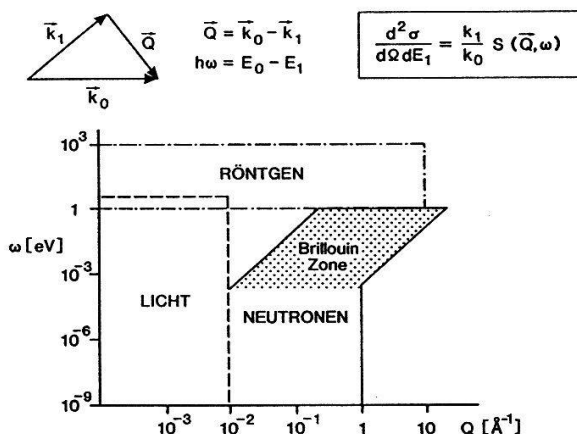*Prinzip eines Streuexperimentes für inelastische Neutronenstreuung*

Abb. 1b
Kinematische Region, welche der Neutronenstreuung zugänglich ist, im Vergleich mit anderen Methoden

Durch Streuung eines monochromatischen Neutronenstrahls an der Probe und anschliessende Energieimpuls-Analyse am Neutron werden die Anregungszustände des Probenmaterials sondiert. Die Streufunktion $S(\vec{Q}, \omega)$, die durch den differentiellen Wirkungsquerschnitt bestimmt wird, ist die Fourier-Transformation der räumlichen und zeitlichen Paarkorrelationsfunktion der Atome in der Materie. Für langsame Neutronen mit Wellenlängen derselben Grössenordnung wie die Atomabstände ($\lambda \gtrsim 1$ Å) ist der Energieübertrag im allgemeinen vergleichbar oder grösser als die Anfangsenergie. Dadurch kann mit dieser Methode die ganze Brillouin-Zone im reziproken Gitter eines Festkörpers eschlossen werden (Abb. 1b). Durch die Wechselwirkung über das magnetische Moment können zudem magnetische Ueberstrukturen und ihre Anregungen untersucht werden. Damit werden Neutronen zum geeigneten experimentellen Werkzeug für verschiedene Gebiete der Naturwissenschaften und der Materialtechnologie. Einige Themen sind in der Tabelle auf der folgenden Seite aufgeführt.

2. Produktion der Neutronen (Spallationsreaktion)

Grundsätzlich gibt es zwei Möglichkeiten, Neutronen in grosser Menge und im Energiebereich von 1 MeV aus Kernen freizulegen:

- Kernspaltung von spaltbarem Material in einem Reaktorkern

- Spallation von schweren Kernen durch einen hochenergetischen Protonenstrahl

Festkörperphysik	- Kristallstrukturen
	- Schwingungsdynamik des Kristallgitters
	- magnetische Strukturen und Dynamik
Flüssigkeiten und Gläser	- Korrelation zwischen den Atomen
	- Bewegung der Atome
Chemie	- molekulare Strukturen
	- Schwingung von Molekülen
Biologie	- molekularer Aufbau von komplexen Molekülen mit biologischer Funktion (Proteine, Riobosomen, Viren usw.)
	- molekulare Aenderungen bei Wechselwirkung mit Licht
Materialforschung	- Textur im Materialaufbau
	- Fehler im kristallinen Aufbau

Beim Beschuss von schweren Kernen mit einem Proton (Energie typisch 600 MeV) werden einige Protonen oder Neutronen durch direktes Knock-out mit hoher Energie herausgeschossen. Diese Nukleonen führen in einem dicken Target zu weiteren Stossprozessen derselben Art (internukleare Kaskade). Nach jedem solchen Stoss bleibt ein hochangeregtes Nukleid zurück, dessen Anregungsenergie auf das ganze Kernvolumen dissipiert wird. Dieses thermische Gleichgewicht hat zur Folge, dass in der nächsten Prozessstufe Neutronen mit einem Maxwell-Spektrum emittiert werden. Die mittlere Energie dieser Neutronen liegt zwischen 1 und 2 MeV. Dieser Anteil des Neutronenspektrums ist demjenigen aus der Kernspaltung in einem Reaktorkern sehr ähnlich. Bei einer Protonenenergie von 590 MeV werden in einem dicken Schwermetalltarget (z.B. W, Pb oder Bi) pro Proton etwa zehn Verdampfungsneutronen freigesetzt.

Nach Emission von prompten Gammas zerfallen die Restkerne über Betazerfall (vor allem Elektroneneinfang).

In einem Wasser- oder Schwerwassermoderator lassen sich die Verdampfungsneutronen effizient auf thermische Energien ($\sim$ 20 meV) moderieren.

3. Aufbau der Spallationsquelle

Nach dem Ausbau der PSI Beschleuniger- und Experimentieranlage werden Strahlströme über 1 mA benützt werden können. Der Strahl wird durch zwei Mesonentargets geführt und kann dann zur Speisung einer Spallationsneutronenquelle genutzt werden. Damit sollen thermische und subthermische Neutronen erzeugt werden. Die Quelle besteht im Prinzip aus:

- einem Schwermetalltarget (Blei-Wismut-Eutektikum)
- einem Moderator (D_2O) und speziellen kalten Moderatoren (flüssiges H_2 und D_2)
- einer massiven Abschirmung

Die Anlage wird in der Verlängerung des heutigen Protonenstrahls, in einem neuen Gebäudekomplex an der Ostseite der Experimentierhalle, untergebracht. Das Konzept der Quelle mit dem vertikalen Einschuss des Protonenstrahls von unten ist aus Abb. 2 ersichtlich.

Das Spallationstarget besteht aus einem zylindrischen Gefäss, welches mit geschmolzenem Blei-Wismut-Eutektikum gefüllt ist. Zur Abfuhr der Wärme, die im Abbremsbereich von 30 cm in das Targetmaterial deponiert wird, nutzen wir die Naturkonvektion des flüssigen Eutektikums. Durch die Auftriebskräfte wird das Material nach oben zum Wärmeaustauscher getrieben und sinkt, durch diesen gekühlt, entlang der Zylinderwände wieder ab. Mit dieser Naturzirkulation erwarten wir bei einer Strahlleistung von 1 MWatt Temperaturdifferenzen im Target von weniger als 300^{0}C. Um

das Target herum ist der D_2O-Moderator in einem Tank von ca. 6 m^3 untergebracht. Zur Moderation der Neutronen auf subthermische Energien sind zwei kalte Quellen – eine 20 l D_2- und eine 0.5 l H_2-Quelle – vorgesehen.
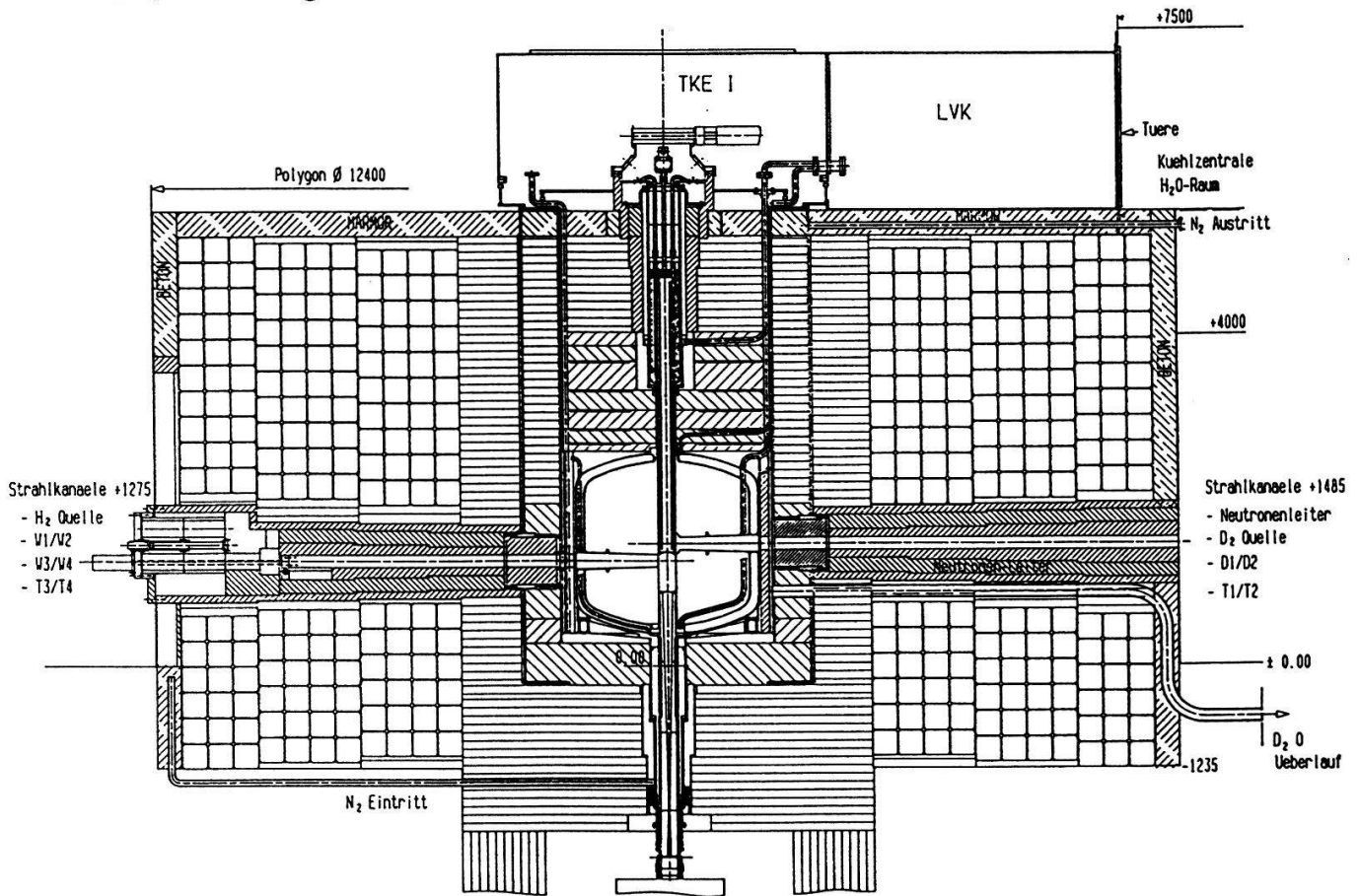
Abb. 2
Vertikalschnitt durch den Targetblock mit Target, Moderatortank und Hauptabschirmung

Der D_2O-Tank ist von einer Abschirmung aus etwa 5 m Stahl und Beton umgeben. Diese massive Abschirmung ist vor allem wegen der hochenergetischen Neutronen aus der ersten Stufe des Spallationsprozesses, die aus dem Target entweichen können, notwendig.

4. Kalte Neutronen

Die Dichte der Zählrate am Detektor eines Experimentes (wie in Abb. 1a) ist gegeben durch:

$$\Delta J = \frac{\Phi}{2\pi}\exp\left(-\frac{\hbar^2}{2m}\frac{k_0^2}{k_BT}\right)\frac{k^4}{k_T^4} \qquad \text{Leuchtdichte der Quelle}$$

$$\times \qquad \Delta F \qquad \text{leuchtende Fläche}$$

$$\times \qquad \frac{dk_{0x}\,dk_{0y}}{k_0{}^2} \qquad \text{Raumwinkel des Strahls}$$

$$\times \qquad \frac{dk_{0z}}{k_0} \qquad \text{Impulsbreite des Strahls}$$

$$\times \qquad d^3k_1 \qquad \text{vom Detektor akzeptierter Impulsphasenraum}$$

$$\times \qquad S(\vec{k_1}-\vec{k_0};\omega) \qquad \text{interessierende Streufunktion}$$

Der Vorteil der Nutzung kalter Neutronen ist unmittelbar ersichtlich:

1. Mit $k_T^4 \sim T^2$ wird die Leuchtdichte mit sinkender Temperatur grösser. Die Kühlung der Neutronen bewirkt eine Phasenraumkompression.

2. Für eine verlangte Energieauflösung $\Delta E \sim k \Delta k$ kann bei tiefer Neutronenenergie ein grösseres Phasenraumelement Δk benützt werden.

Für hochauflösende Experimente in einem beschränkten $(\vec{Q}, \omega)$-Bereich bieten somit kalte Neutronen einen wesentlichen Vorteil.

Dies ist einer der Gründe, warum wir beim SINQ-Projekt starkes Gewicht auf eine möglichst effiziente kalte Quelle legen. Abbildung 3 zeigt die spektralen Neutronenflüsse ausserhalb der Abschirmung an Strahlrohren, die bei der Position des Monochromators erwartet werden können. Der Flussgewinn im Wellenlängenbereich von $\lambda > 3$ Å durch die kalte D_2-Quelle ist klar ersichtlich.
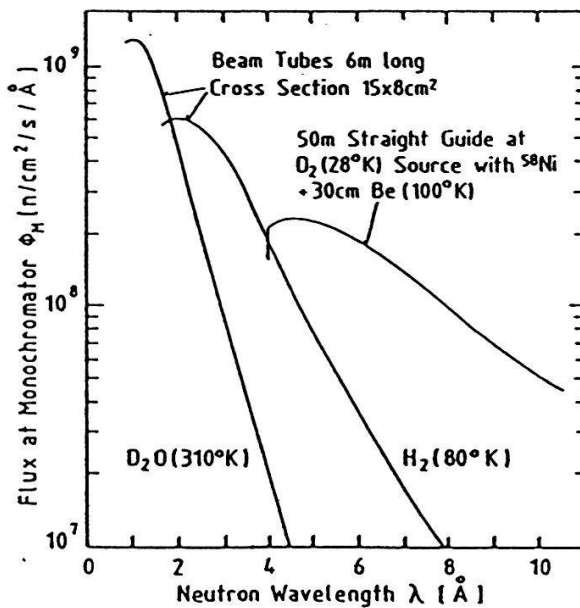
Abb. 3
Spektraler Neutronenfluss an den Monochromatorpositionen im thermischen und kalten Bereich

5. Neutronenleiter

Das Phänomen der Totalreflexion von Neutronen an glatten Oberflächen gestattet ein anderes Konzept des Neutronentransports als den freien Flug durch ein Strahlrohr. Der Brechungsindex für Neutronenwellenpakete ist gegeben durch

$$n = 1 - \frac{\lambda^2}{2\pi} \cdot N \cdot \sigma_{coh}$$

N ist die Atomdichte des Materials.

Die kohärente elementare Streulänge ist für die meisten Kerne positiv. Daher wird der Brechungsindex n < 1. Totalreflexion unterhalb eines kritischen Einfallwinkels $\varphi_c = \sqrt{2(1-n)}$ am optisch dichteren Medium ist die Folge. In einem planparallelen Kanal ergibt sich daher ein Akzeptanzwinkel für Neutronentransport durch Totalreflexion von

$$\delta = 2k \cdot \lambda$$

k ist vom Material abhängig und beträgt für

$$Ni \quad : k = 1.73 \text{ mrad}/\text{Å}$$
$$^{58}Ni \quad : k = 2.05 \text{ mrad}/\text{Å}$$

Für Neutronen mit Wellenlängen $\lambda > 4$ Å wird damit der Akzeptanzwinkel in einem Neutronenleiter grösser als der offene Raumwinkel eines 6 m langen Flugrohrs mit einem Durchmesser von 10 cm.

Das geplante Neutronenleitersystem und seine Instrumentierung für die Nutzung kalter Neutronen ist aus Abb. 4 ersichtlich. Diese Standorte der Instrumente sind natürlich besonders günstig bezüglich des Untergrunds.

Abb. 4
Auslegung der Quelle und der Experimente in der Neutronen- und Leiterhalle

Abb. 5
TEM-Aufnahme einer Ni/Ti/Schichtfolge (60 Å)aus der Superspiegel-Entwicklung

Einige Instrumente könnten durchaus eine höhere Divergenz des einfallenden Neutronenstrahls auf-
nehmen. Die dabei erzielte Flusserhöhung wäre sehr willkommen. Durch den Einsatz von Super-
spiegeln lässt sich dieses Ziel erreichen. Abbildung 5 zeigt eine TEM-Aufnahme einer gesputterten
Schichtfolge von je 60 Å Dicke der beiden Materialien Ni und Ti. Diese beiden Elemente haben
sehr verschiedene Streulängen für Neutronen; die Schichtfolge wirkt deshalb als Schichtgitter für
Bragg-Reflexionen.

Die Möglichkeiten zur Ausdehnung des Totalreflexionswinkels mit Schichtfolgen variabler Dicke
werden durch die Reflexionsdaten in Abb. 6 evident. Die schlecht reflektierenden Zwischenbereiche
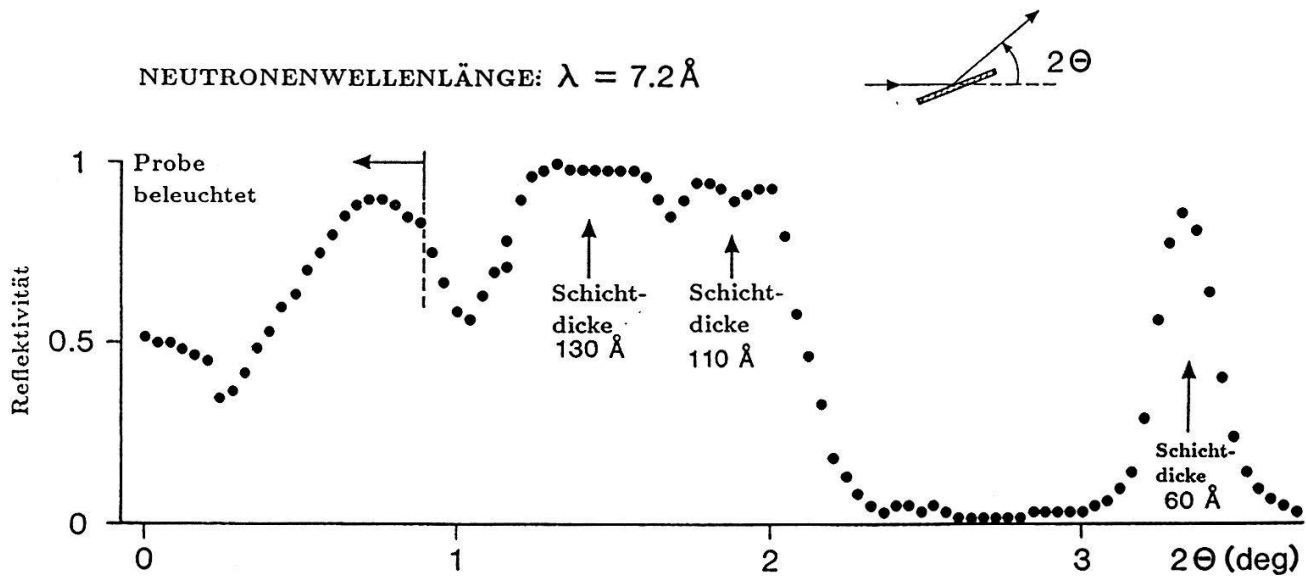sollen durch weitere Schichtfolgen "aufgefüllt" werden.

Abb. 6
Reflexionsdaten für Neutronen einer Multi-Schichtfolge

SELFSIMILARITY
A BASIC PRINCIPLE OF NATURE - FROM GEOMETRY TO ANALYSIS

S.Grossmann, Fachbereich Physik der Philipps-Universität
Renthof 6, D-3550 Marburg, Federal Republic of Germany*

Abstract: The superposition principle of linear physics is replaced by the scaling principle in nonlinear physics. Selfsimilarity together with structure implies fractality. It is the combination of nonlinear and linear terms which allows for differential laws in a fractal world. Various applications are pointed out, in particular a new analysis of fully developed turbulent fluid flow by a Fourier-Weierstrass decomposition which, for the first time, allows to realize Reynolds numbers as high as 10^6.

1.   Superposition vs scaling

Linear physics like electro-magnetism, quantum physics etc. is governed by the superposition principle. It says: given two solutions $x_1(t)$ and $x_2(t)$, then the sum $x_s(t) = x_1(t) + x_2(t)$ also is a possible solution. Huyghens' principle, holography, Fourier decomposition, etc., rest on this fact. Superposition is a consequence of a linear equation of motion. Consider as a most simple but typical example

$$dx/dt = - ax. \qquad (1)$$

Its significant features are: The amplitude's size is arbitrary; the parameter defines a characteristic time scale a^{-1}.

Typical nonlinear laws as

$$dx/dt = - bx^n, \ n \neq 1 \qquad (2)$$

do   n o t   allow superposition, they are   n o t   homogeneous, and they do n o t define a time scale. The simultaneous rescaling $x \rightarrow \alpha x$, $t \rightarrow \beta t$ leaves (2) form-invariant, with the same b, if only $\alpha = \beta^{1/(1-n)}$. This is reflected in the solution $x(t) = [(n-1)bt]^K$, with the "similarity exponent" $K = 1/(1-n)$. This holds if $(n-1)btx_0^{(n-1)} \gg 1$, i.e., if the initial value does not externally put a scale.

The characteristic general law of nonlinear physics which holds instead of the additive superposition rule in linear physics reads

$$x(\lambda t) = \lambda^K x(t). \tag{3}$$

In the simple example of eq.(2) $K = 1/(1-n)$. The scaling law (3) is equivalent to $x(t) \propto t^K$. It expresses the absence of any natural scale and is also denoted as allometric law. For more details compare reference [1].

2. Fractality

The solution of eq.(2) is not very exciting. It has no structure but decays monotonously. What happens if there would be some structure, say a hump. If selfsimilarity shall be maintained this hump has to be present everywhere and on all scales. The resulting object is a fractal. So one looses differentiability, since between arbitrary close points on the curve there cannot be a tangent, as the same (rescaled) hump must be still in between. The curves are no longer rectifiable, i.e., their length depends on the scale of the measuring stick [2].

Selfsimilarity a n d structure as simultaneous features of a physical phenomenon necessarily imply fractality. This automatically seems to exclude differential laws like e.g.(2). Fractal objects are all around us, artificial ones like Koch curves, Julia sets and the like or physical ones like Lichtenberg figures, electro-deposition trees, surfaces of clouds [3], organs of mammals [4], Brownian paths [2], etc.

Instead of using differential laws one usually characterizes them by algorithms [5], iterations and all that. Quantitative properties are condensed in selfsimilarity exponents K, sets of those in the multifractal case, in the Hausdorff-dimension D_H, etc.

Two questions arise: First, there seems to be an unsurmountable gap between the differential laws of nature and the algorithms of the fractal world. How do they come together? In reality they do, as for example any turbulent flow shows, that does both, satisfy the partial differential equation of Navier and Stokes and has hierarchical cascade structure. Second, why are there nonlinear laws that do n o t seem to imply selfsimilar solutions? Both questions are related.

3. Restricted selfsimilarity [1]

Laws of nature generally combine (1) and (2),

$$dx/dt = - ax - bx^3. \tag{4}$$

A more physical example is the Navier-Stokes equation for the Eulerian flow field $u_i(\vec{x}, t)$

$$\partial_t u_i = - \vec{u} \cdot \nabla u_i - \partial_i p + \nu \Delta u_i + f_i, \tag{5}$$

plus appropriate boundary conditions. Equation (4) can still be solved analytically (in contrast to (5)) to give

$$x(t) = \sqrt{a/b} / \sqrt{(a/bx_0^2 + 1)e^{2at} - 1}. \tag{6}$$

One easily notes various regimes, provided the "Reynolds number" composed of the parameters of the equation and of the external conditions (here the initial value) is large.

$$\text{"Re"} := bx_0^2/a \gg 1. \tag{7}$$

Initially, $x(t=0) = x_0$, and shortly after start $x(t)$ decreases as $x_0[1 - bx_0^2t]$, i.e., we have an initial value dominated regime. After long time, if $2at$ is sufficiently large, the decay is exponential, $x(t) = \sqrt{a/b} \exp(-at)$. The nonlinearity now is irrelevant, there is pure linear behaviour but with a universal amplitude independent of x_0. For sufficiently small $x(t)$ always the linear term wins and guarantees differentiability. Of course, this costs scaling and selfsimilarity; there is a natural time scale a^{-1} in this "viscous" or "linear" range.

If Re were small, $\ll 1$, the two discussed regimes would fit together. $x(t) = x_0(1-at)$ for small t and $x(t) = x_0\exp(-at)$ for large t. But under the large Re condition (7), there is a u n i v e r s a l   s e l f s i m i l a r   s c a l i n g range in between,

$$\sqrt{a/b} \ll x \ll x_0 \quad \text{or} \quad (2bx_0^2)^{-1} \ll t \ll (2a)^{-1}, \tag{8}$$

in which the solution is approximately

$$x(t) = 1/\sqrt{2bt}. \tag{9}$$

It is independent of the initial condition, has no natural scale, and satisfies (3) with $K = -1/2$. The linear component of the differential equation (4) is invisible in this range.

The condition for its existence is the large Reynolds-like number (7), containing the initial value as well as the physical parameters of the equation of motion (cf.[1]).

This example makes clear why selfsimilarity is compatible with differentiability, why we meet in reality scaling invariance in restricted ranges only, why despite of nonlinear equations selfsimilarity might be absent at all (Re $\ll$ 1), and why there might be different scaling behaviour in different ranges (if several nonlinearities are present). Note finally that there are nonlinearities which never allow an extended scaling range, as e.g. a step function.

4.   Developed turbulence

If the physical Reynolds number $Re = UL/\nu$ is large, one finds an eddy cascade that constitutes the chaotic flow field. This should solve equation (5) without the viscous term $\propto \nu$, although small changes in $\vec{u}$ must still be dominated by viscosity in order to maintain differentiability, the prerequisite to have the Navier-Stokes equation valid at all. In order to analyse the selfsimilar structure one evidently has to introduce a scale, say r (the distance between two positions in the flow field), which does not appear in the Navier-Stokes equation (5).

There are presently three possible methods to introduce the scale r.

1) The variable scale decomposition [6]

$$u_i^{(r)}(\vec{x},t) = \int_{V_r} u_i(\vec{x}+\vec{y},t)\,dV(y)/V_r, \tag{10}$$

which averages over spheres with radius r and separates the large scales ($\geqslant$r) in $u_i^{(r)}$ from the subscales ($\leqslant$r) in $\tilde{u}_i^{(r)} = u_i - u^{(r)}$. Scanning through all scales one can analyse all ranges in the flow field, the viscous subrange $0 \leq r \leqslant 9\eta = 9(\nu^3/\varepsilon)^{1/4}$, the universal inertial nonlinear range $9\eta \leqslant r \leqslant L$ up to the input (boundary) range $r \cong L$. In a meanfield like treatment [6] of the Navier-Stokes equation one can describe the structure of turbulence quantitatively without any fit parameter. In particular, the inertial range structure function is

$$\langle\langle |\vec{u}(\vec{x}+\vec{r}) - \vec{u}(\vec{x})|^2 \rangle\rangle = b\varepsilon^{2/3}r^{2/3} \tag{11}$$

with b = 6.3, near the experimental value $\approx$ 8.4. The transition between linear (viscous) and nonlinear (inertial) range is calculated to be $r_t \approx 9\eta$. Contaminant diffusion, eddy viscosity, turbulent Prandtl number can be dealt with quantitatively [7].

2) Another powerful method to analyse fluid flow with respect to its scaling properties is the wavelet transform [8], [9].

$$u_w(x,r) = \int dy\, u(y) w((x-y)/r), \tag{12}$$

with a wavelet w(z) scanning all scales r and all positions x. Due to $\int w(z)dz = 0$ the wavelet transform filters predominantly the scales of size r, present at position x. The spottiness of fractal homogeneous turbulence is visible as a function of x, the scaling behaviour becomes apparent when varying r (in cone-like structures).

3) Quite recently we introduced a Fourier-Weierstrass decomposition to analyse the Navier-Stokes solutions [10]. The Euler velocity field $u_i(\vec{x},t)$ is Fourier analysed

$$u_i(\vec{x},t) = \sum_{\vec{p}\varepsilon k} u_i(\vec{p},t) e^{i\vec{p}\cdot\vec{x}}, \tag{13}$$

but only the wave vectors $\vec{p}$ from a set of geometrically scaling eddies are admitted, $K = UK_l$, the $\vec{p}\varepsilon K_l$ are related to those in K_{l+1} by a factor of $\lambda(=2)$. Hence, the sequence $p \sim \lambda^l$ defines a Weierstrass function like selfsimilar structure from the very beginning. The amplitudes $u_i(\vec{p},t)$ are then determined by (numerically) solving the coupled set of o.d.e.'s resulting from the Navier-Stokes equations.

We treated 572 (or 836) mode systems, have Reynolds numbers as high as $Re \cong 10^6$, there are about 3 decades of wave lengths (eddy sizes) on 11 eddy levels. The solutions are chaotic, time correlations decay, the interlevel transfer fluctuates wildly but in the mean it stays constant in the ISR. The amplitudes $u(\vec{p})$ scale $\propto 2^{-l/3}$ if $\vec{p}\varepsilon K_l$, the typical chaotic time scale behaves $\propto 2^{-2l/3}$. We numerically determined the moment exponents $\zeta(m)$ of

$$\langle\langle |\vec{u}(\vec{x}+\vec{r}) - \vec{u}(\vec{x})|^m \rangle\rangle \propto r^{\zeta(m)}. \tag{14}$$

Although one expects deviations from the classical scaling $\zeta(m) = m/3$, as typically found in hierarchical diffusion models [11], in our solutions the deviations $\delta\zeta(m) = \zeta(m) - m/3$ turned out to be less than the statistical error, so are well compatible with $\delta\zeta(m) \cong 0$.

5.   Concluding remarks

Selfsimilarity is t h e   signature of nonlinear physics. We are just probing methods to analyse and elucidate the scaling properties for given nonlinear differential equations. The task is to go beyond abstract algorithms, describing abstract systems which model real physical systems only more or (better) less. To state it differently, an analytical theory of fractal geometry is wanted. Various properties of what this analytical theory should ultimately possess have been discussed, the restricted range of selfsimilarity in particular, and the usefulness of variable scale decomposition and of Fourier-Weierstrass-series. Quite recently this was extended to include the fractal spottiness of the active regions of turbulence, i.e., to the spatial intermittency [12]. In the frame of the Fourier-Weierstrass representation the dissipation fluctuations and the moment deviations $\delta\zeta(m)$ turn out to be more independent than generally be- lieved. One consequence is a new relation between the $\zeta(m)$ and the dissipation decorrelation ex- ponent μ, namely (cf.[12]), $\mu = 2\zeta(2) - \zeta(4)$.

6.   References

[1] S.Grossmann, Phys.Bl.45,172(1990)

[2] B.B.Mandelbrot, The Fractal Geometry of Nature, Freeman, San Francisco 1982

[3] S.Lovejoy, Science 216,185(1982)

[4] M.Sernetz, B.Gelléri, J.Hofman, J.Theor.Biol.117,209(1985)

[5] H.-O.Peitgen, P.H.Richter, The Beauty of Fractals, Springer, Berlin 1986

[6] H.Effinger, S.Grossmann, Z.Phys.B66,289(1987)

[7] H.Effinger, S.Grossmann, Phys.Fluids A1,1021(1989)

[8] A.Grossmann, J.Morlet, T.Paul, J.Math.Phys.26,2473(1985)

[9] F.Argoul, A.Arnéodo, G.Grasseau, Y.Gagne, E.J.Hopfinger, U.Frisch, Nature 338,51(1989)

[10] J.Eggers, S.Grossmann, Does chaos imply intermittency in fully developed turbulence, preprint, Marburg 1990

[11] A.Erzan, S.Grossmann, A.Hernández-Machado, J.Phys. A: Math. Gen. 20,3913(1987)

[12] J.Eggers, S.Grossmann, Is anomalous velocity scaling in turbulence due to dissipation fluctuations, preprint, Marburg 1990

TRANSITION TO TURBULENCE IN THERMAL CONVECTION

F.H. Busse, Institute of Physics, University of Bayreuth
D-8580 Bayreuth, FRG

Abstract: Thermal convection in a horizontal fluid layer heated
from below represents the simplest hydrodynamic system exhibiting
the phenomenon of turbulence. Because of the horizontal isotropy
of the physical conditions regular patterns can be observed over
a wide range of the parameter space, even in the limit of
asymptotically high Rayleigh numbers. On the other hand, spatio-
temporal chaos in the form of phase turbulence is possible in the
limit of small amplitudes of motion.

1.   Introduction

During the past three decades Rayleigh-Bénard convection in
a fluid layer heated from below has assumed a central role in the
understanding of the origin of turbulence. Because of the
horizontal isotropy of the energy source driving the motions, the
evolution from simple to complex forms of flows occurs in a more
regular fashion than in other fluid systems such as channel flow
or pipe flow. Coherent structures now seen in many types of fully
developed turbulence have long been known to meteorologists and
solar physicists from observations of convection in the
atmospheres of the Earth and of the sun. Through the use of
temperature dependent properties such as the index of refraction
instantaneous two-dimensional pictures of the convection layer
can be obtained which allow the visualisation of structures even
in the case of fully developed turbulent flow. It is thus not
surprising that more regular features have been recognized in
thermal convection than in other kinds of fluid turbulence.

The advantages that the Rayleigh-Bénard system offers from
the experimental and observational point of view are matched by

its theoretical attractions. Sequences of subsequent bifurcations can be isolated through their symmetry breaking properties in numerical simulations, and because of their supercritical or only weakly subcritical character these bifurcations can be compared quantitatively with experimental measurements in many cases. In this respect the Rayleigh-Bénard system resembles the Taylor-Couette system of flow between differentially rotating co-axial cylinders. In fact, both systems are mathematically identical with respect to the two-dimensional (or axisymmetric) solutions if the small gap limit with nearly co-rotating cylinders of the Taylor-Couette system is assumed. The temperature field of convection rolls corresponds to the azimuthal component of the Taylor vortex motion in this case.

In following it is attempted to give a brief outline of the theory of Rayleigh-Bénard convection in terms of some general properties. For details and for the comparison with experiments the reader is referred to the reviews [1], [2].

2.   Weakly Nonlinear Rayleigh-Bénard Convection

For convection layers realized in the laboratory, the Boussinesq approximation, in which the temperature dependence of the fluid density

$$\rho = \rho_0(1 - \gamma(T - T_0)) \qquad (1)$$

is taken into account in the gravity term only of the basic Navier-Stokes equations, is satisfied extremely well. In this case two dimensionless parameters suffice to describe the external conditions of the horizontally extended fluid layer, the Rayleigh number R and the Prandtl number P which are defined by

$$R \equiv \frac{\gamma g(T_2 - T_1)d^3}{\nu\kappa} , \qquad P = \frac{\nu}{\kappa} \qquad (2)$$

where d is the thickness of the layer, g is the acceleration of gravity, T_2 and T_1 are the temperatures of the lower and upper boundaries, respectively, and ν and κ are kinematic viscosity and thermal diffusivities of the fluid. The two parameters (2) have been chosen such that the onset of convection is described by the
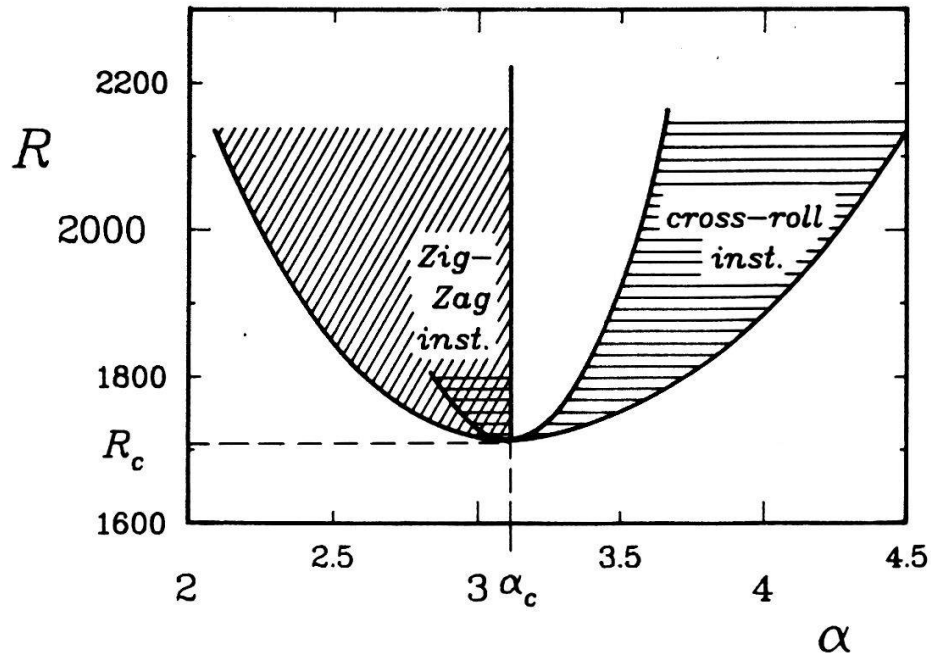
Figure 1: The Rayleigh number R for onset of convection in a layer with rigid boundaries as a function of the wavenumber α (outer parabola). Convection rolls are subject to instabilities in the shaded regions which have been determined for infinite Prandtl number P.

Rayleigh number only. The outer curve in figure 1 is thus independent of P. Most finite amplitude properties of convection depend rather strongly on the Prandtl number.

The linear theory from which the parabolic curve of figure 1 is obtained leads to the following general expression for the vertical velocity of convection which we use here as a representative for the dependent variables,

$$u_z = f(z,\alpha) \sum_{n=-N}^{N} c_n \exp\{i\underset{\sim}{k}_n \cdot \underset{\sim}{r}\}$$

with

$$\underset{\sim}{k}_{-n} = -\underset{\sim}{k}_n, \quad |\underset{\sim}{k}_n| = \alpha, \quad c_{-n} = c_n{}^*, \quad \sum_{n=1}^{N} |c_n|^2 = \varepsilon^2 \qquad (3)$$

where the asterisk indicates the complex conjugate and the summation limit N may tend to infinity. Because of the horizontal isotropy of the problem the solution is highly degenerate. The length of the horizontal wave vectors $\underset{\sim}{k}_n$ is fixed by the

N=1: Rolls   N=2: Square Patterns

N=3: Hexagonal Patterns

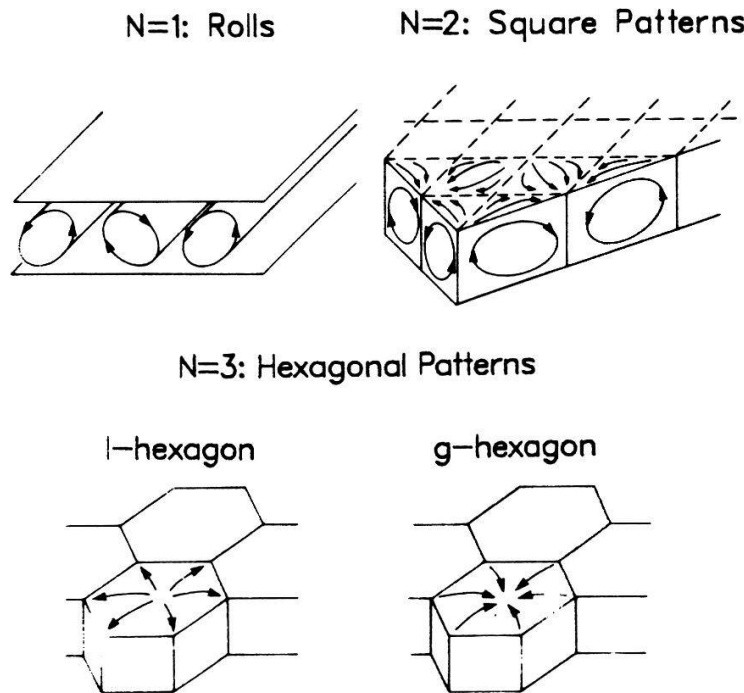I—hexagon   g—hexagon

Figure 2: Patterns of convection in horizontal layers heated from below.

wavenumber α, but they may have arbitrary orientation and the coefficients c_n may also be arbitrary. Not all solutions of the linear problem correspond to steady solutions of the nonlinear problem in the limit when the amplitudes of the latter approach zero. An expansion of the nonlinear solution in powers of the amplitude ε yields a hierarchy of systems of linear inhomogeneous equations which can be solved when solvability conditions are satisfied. These solvability conditions provide nonlinear equations for the coefficients c_n in dependence on the vectors k_n. For reasons of symmetry all solvability conditions can be satisfied by solutions of the form

$$|c_n|^2 = \varepsilon^2/N \qquad \text{für} \quad n = 1,\ldots, N \qquad (4)$$

if a regular distribution of vectors $\underset{\sim}{k}_n$ is prescribed with equal angles between neighboring $\underset{\sim}{k}$-vectors. Some examples are shown in figure 2. Since the solutions with N=1,2,3 are the only ones that correspond to periodic patterns in the plane, they also appear to preferred in physical realisations. Depending on the boundary conditions, the four cellular forms of convection seen in figure 2 can be observed in experiments.

To answer the question of the stability of various forms of convection the evolution in time of the coefficients c_n must be considered. When we allow for a variation in time on the scale $\varepsilon^{-2}d^2/\kappa$, we obtain the above mentioned solvability conditions with added time derivatives,

$$V\frac{d}{dt} c_i = -(R-R_c)c_i + \beta \sum_{n,m=-N}^{N} c_n c_m \, \delta(\underset{\sim}{k}_m + \underset{\sim}{k}_n - \underset{\sim}{k}_i) +$$

$$\sum_{n=1}^{N} |c_n|^2 \Big[A(\underset{\sim}{k}_i \cdot \underset{\sim}{k}_n) + E(\underset{\sim}{k}_i \cdot \underset{\sim}{k}_n) \, \underset{\sim}{\Omega} \cdot \underset{\sim}{k}_i \times \underset{\sim}{k}_n \Big] c_i \qquad (5)$$

In writing this system of equations we have allowed for the fact that most qualitative properties of the problem remain unchanged when the layer is rotating about a vertical axis with the dimensionless angular velocity $\underset{\sim}{\Omega}$. By assuming that the centrifugal force is small in comparison with gravity we preserve the isotropy of the layer. Only the Coriolis force enters the dynamics of convection. There is an important difference from the non-rotating case, however, in that the cross-product of two $\underset{\sim}{k}$-vectors enters the equations (5) for finite $\underset{\sim}{\Omega}$. For $\underset{\sim}{\Omega} = 0$ equations (5) can be written in the form

$$V \frac{d}{dt} c_i = -\frac{\partial}{\partial c_{-i}} F(c_{-N}, \ldots, c_N) \qquad (6)$$

while for $\underset{\sim}{\Omega} \neq 0$ the gradient character of right hand side of equations (5) is lost. Since the function F has at least one minimum, the gradient character (6) ensures the existence of at least one stable steady solution. Any disturbance of a minimizing solution $\{c_{-N}, \ldots, c_N\}$ must decay according to equations (6). They may exist more than one minimizing solutions of the functional F in which case the history of an experiment determines the physically realized state. This situation does occur, for instance, in the competition of rolls and hexagonal patterns.

In a rotating convection layer the existence of stable steady pattern can no longer be guaranteed. Indeed, as Küppers and Lortz [3] have shown all steady solutions describing convection flows become unstable, when the rotation rate exceeds a certain critical value. In the laboratory realisation the

system exhibits the phenomenon of phase turbulence [4]. The
visualisation shows a random assembly of patches of convection
rolls with different orientations. These rolls are replaced in
time by other rolls such that temporal and spatial distributions
of rolls vary in a chaotic manner as can be demonstrated by an
experimental movie. Another case of phase turbulence occurs in a
non-rotating convection layer with stressfree boundaries. In this
case the gradient character (6) of the evolution equations (5)
also disappears and a chaotic behavior is found [5].

3.   References

[1]   F.H. Busse, in "Mantle Convection", W. Peltier ed., Gordon
      and Breach, 23-95 (1989).

[2]   F.H. Busse, Chapter 5 in "Hydrodynamic Instabilities and the
      Transition to Turbulence", H.L. Swinney and J.P. Gollub,
      eds., Springer-Verlag (1981).

[3]   G. Küppers and D. Lortz, J.Fluid Mech. 35, 609 (1969).

[4]   F.H. Busse and K.E. Heikes, SCIENCE 208, 173-175 (1980).

[5]   F.H. Busse, in Proc. 2nd European Conference in Turbulence,
      H.H. Fernholz and H.E. Fiedler, eds., Springer, 152-161
      (1989).

TWO PARTICLE MOMENTUM DISTRIBUTION IN METALS
AND SUPERCONDUCTING OXIDES

P. Genoud, L. Hoffmann, T. Jarlborg, A.A. Manuel, S. Massidda*, M. Peter, W. Sadowski and E. Walker, Département de Physique de la Matière Condensée, Université de Genève, 24 Quai Ernest Ansermet, CH-1211 GENEVE 4, and (*) IRRMA, EPFL-PH, Ecublens, CH-1015 LAUSANNE

Abstract: The Two Particle Momentum Distribution (TPMD) is determined by measuring the Angular Correlation of the Annihilation Radiation (ACAR) of electron-positron pairs. In alkalis and some transition metals, including superconducting compounds, results closely resemble band structure predictions. For ferromagnetic Fe and Cerium, empirical corrections restore agreement. Results in superconducting oxides are at present controversial. The Geneva group has measured with relatively very high signal/noise and has found no FERMI break even where band theory would have predicted one. More positron data are urgently needed, and present ACAR machines are far from giving the theoretically possible performance: we hope for a better machine at PSI.

1.   The experiment

Positrons are shot into samples from a source (in our case ^{22}Na), loose their kinetic energy within some ps (several microns) in metals, and annihilate after some hundred ps. In oxides, the thermalisation time is longer, the penetration deeper, full thermalisation not assured. Energy and momentum are carried away by two or more photons, the cross section is given by the classical electron radius, higher orders occur with decreasing probability (fine structure constant). The photons are nearly antiparallel, their angle is of order (electron momentum / m_e*c), which means milliradians. The distribution of these angles is detected with a pair of High Resolution Proportional Counters (HRPC) and represents a projection of the TPMD. The counters used in Geneva, originally proposed by JEAVONS and CHARPAK, are outstanding because of their high resolution and efficiency. When used with a long lived β emitter as a source, their response time is sufficient - with a strong positron beam source, they would saturate. From the projections,

the TPMD can be recovered by tomographic techniques, and in the
TPMD, the FERMI surface can be identified. HOFFMANN's thesis de-
scribes the apparatus used in Geneva [1].

2.   Independent Particle model (IPM)

The momentum distribution (MD) of a BLOCH particle with momen-
tum k contains higher momentum components (HMC) for vectors k + G,
where G are the reciprocal lattice vectors. Suppose a band which is
partially filled with nearly free electrons (NFE), and it's MD will
bring out a nearly filled FERMI surface in the first BRILLOUIN zone.
The HMC will show up in analogous surfaces in the higher BRILLOUIN
zones, with rapidly decreasing amplitudes. This is exactly the pic-
ture we found in the alkali metals, with amplitudes which agree well
with band calculations, as shown in a recent review article [2].
The positron momentum part of TPMD is weak, by neglecting it only
a minor error is committed. In the case of a transition metal like
Vanadium, the NFE approximation no longer holds, nevertheless IPM
calculations predict a FERMI surface in satisfactory agreement with
TPMD measurements by ACAR.

For more complicated (d- and f bands) and molecular complexes
such as treated by CHIBA [3] there will be more and more filled
subbands; the subbands crossing the FERMI energy will carry less
weight and consequently, the TPMD will be marked less by the
quasiperiodic FERMI surface and more by the FOURIER transform of
the atomic or molecular wave functions. As long as positron momentum
can be neglected, it is possible to superpose the amplitudes from
all BRILLOUIN zones and to obtain the approximate electron density
in the space of the crystal momentum k of the BLOCH electrons (this
procedure is called LOCK CRISP WEST (LCW) folding [4]).

3.   Interactions and correlations

The success of the IPM is remarkable in view of the well known
fact there exists no general justification for such a model. Elec-
tromagnetical and quantum mechanical interactions produce
correlation and lead to the superposition of many configurations,
but also to computational difficulties that cannot be handled in a
general way. The program is then to push IPM to the its limits [5]
and to describe correlation effects as efficiently and economically
as possible. One way to describe correlation is the use of _enhance-
ment_ factors. Correlations tend to "smooth out" the difference in
population above and below the FERMI energy (E_F), and the calcula-

tion of this effect has received a large deal of attention. JARLBORG and SINGH [6], DANIUK et al. [7] and SORMANN [8] have in recent articles approached the enhancement problems with methods of different sophistication. The e-e interaction produces partial mixing of electron and hole states. The e-positron interaction produces enhancement which, below E_F, partially compensates the effect of e-e. SINGH et al. [9] have proposed a parametrisation of the enhancement (and de-enhancement) effects, which is based on energy and angular momentum.

Interactions of a different kind are the ordering phenomena like superconductivity, ferromagnetism, antiferromagnetism etc. There does not seem to be clear evidence of positron spectra changing due to superconductivity. Antiferromagnetism has been observed to alter the TPMD for instance in Chromium [10]. Ferromagnetic polarisation can be observed because positrons are polarised in the direction of flight, and retain their polarisation in the solid, as SEEGER has shown [11]; this polarisation was observed clearly in Fe for example [12]. In this case a spin polarised IPM calculation did not lead to an acceptable description of observed polarisation, but agreement was obtained through subsequent "parametrisation". Parameters were introduced essentially to displace subbands relatively to each other. A similar treatment was successful for getting the TPMD measured in Cerium to agree with calculation: the f-band had to displaced by 0.5 eV to higher energies [13]. From the ACAR studies of metals and intermetallic compounds, we gained the impression that, starting from IPM, and applying judiciously certain semi-empirical corrections, TPMD was understood.

4.   High-T_c Superconductors

The discovery of High-T_c Superconductivity has brought excitement and surprises, new interest and new challenges to ACAR. In Geneva we were early to measure $YBa_2Cu_3O_7$ and to interpret our measurements as confirmation for the presence of a FERMI surface in this compound. We then proceeded to analyse carefully $YBa_2Cu_3O_6$ and found a similar structure in the LCW folded results of that compound too which forced us to admit that the structures we had observed where not necessarily indicative of a band-structure, and even less of a FERMI surface. In particular it became clear that the contribution of positron momentum to the LCW picture was important in the oxides, and that interpretation could only be done after quantitative analysis of data with sufficiently intense signals. At present there is

qualitative agreement between calculation and observation for the 1237 compound in p-space, as MASSIDDA [14] has shown agreement with his careful LAPW calculations, and as was confirmed in Geneva after elimination of some errors in our way of calculating TPMD. No break in p-space is seen which could be attributed to a manifestation of the FERMI surface. This is compatible with the level of statistical fluctuations in our experiment [15]. We do not agree with claims to the contrary by other authors, since our measurements are based on the biggest number of counts so far. By superposition of all HMC components (LCW and symmetry folding) we should however enhance a putative FERMI break to visibility well above noise, yet a recent effort in this direction failed to produce this break [16]. We are presently investigating if this discrepancy is a consequence of 1) an insufficient experimental setup, 2) an underestimation of the calculated band dispersion, 3) a defective sample, or 4) if it should be interpreted as coming from an additional FS smearing.

The story of positrons in High-T_c Superconductors so far should have thought us great caution in drawing conclusions from this new result which is in contradiction not only with claims by other positron groups, but also with photoemission studies, and perhaps also very recent tentative deHvA results reported by F. MUELLER [17]. But it is to be remarked that transport results might confirm the presence of some singularity but might not permit to judge the amount of smearing around the FERMI break. Spectroscopic results, on the other hand, involve transition to excited states which pose their problems. Clear-cut positron results concerning the momentum distribution around the FERMI surface in oxides would therefore be an essential contribution.

5.   Conclusion and outlook

The ACAR technique gives the TPMD of metals and oxides and hence furnishes valuable calibration for the so-called "ab-initio" calculation. In the case of High-T_c superconductors, the ACAR data are still controversial: faster measurements on more substances would be necessary. Fortunately, the ACAR technique is far from having been developed to optimum performance; large factors could be obtained from better detectors and more intense sources. We are therefore happy that the PAUL SCHERRER Institute (PSI) is seriously considering the installation of a high-performance positron source. The result of a recent meeting on this subject will appear soon in H.P.A. [18].

6.   <u>References</u>

[1] L. Hoffmann, Ph.D. thesis n°2342, Univ. of Geneva, 1989.

[2] M.Peter, IBM Journal of Res. and Dev. <u>33</u>, 333 (1989).

[3] T. Chiba, The Journal of chemical Physics <u>64</u>, 1182 (1976).

[4] D.G. Lock, V.H.C. Crisp and R.N. West, J. Phys. F: Metal Phys.
     <u>3</u>, 561 (1973).

[5] W. Kohn, in "Highlights of Cond. Mat. Theory", Proc. Interna-
     tional School of Physics, course LXXXIX, F. Bassani, F. Fumi
     and M.P. Tosi eds., North Holland Publ. Co., Amsterdam, 1985.

[6] T.Jarlborg and A.K. Singh, Phys. Rev. B <u>36</u>, 4660 (1987).

[7] S. Daniuk, G. Kontrym-Sznajd, J. Majsnerowski, M. Sob and H.
     Stachowiak, J. Phys.: Condens. Matter <u>1</u>, 6321 (1989).

[8] H. Sormann, in "Positron Annihilation", L. Dorikens-Vanpraet,
     M. Dorikens and D. Segers eds, World Scient. Publ. Co., Sin-
     gapore, p. 272, 1988.

[9] A.K. Singh, A.A. Manuel, T. Jarlborg, Y. Mathys, E. Walker and
     M. Peter, Helv. Phys. Acta <u>59</u>, 410 (1986).

[10] AK. Singh, A.A. Manuel and E Walker, Europhys Lett <u>6</u>, 67 (1988)

[11] A. Seeger, Helv. Phys. Acta <u>63</u> (1990), to appear.

[12] P. Genoud, A.K. Singh, A.A. Manuel, T. Jarlborg, E. Walker, M.
     Peter and M. Weller, J. Phys. F <u>18</u>, 1933 (1988).

[13] T. Jarlborg, A.A. Manuel, M. Peter, D. Sanchez, A.K. Singh,
     J.L. Stephan, E. Walker, W. Assmuss and M. Hermann, in "Posi-
     tron Annihilation", L. Dorikens-Vanpraet, M. Dorikens and D.
     Segers eds, World Scient. Publ. Co., Singapore, p. 266, 1988.

[14] S. Massidda, to be published.

[15] L. Hoffmann, A.A. Manuel, P. Genoud, M. Peter, W. Sadowski, H.
     Scheel, E. Walker and J.Y. Henry, Phys. Rev. B (1990),to appear

[16] L. Hoffmann, S. Massidda, W. Sadowski, E. Walker, A.A. Manuel,
     M. Peter and A.J. Freeman, 10th General Conf. of the Condensed
     Matter Div. of the European Phys. Soc., Lisbon, Portugal, Apr
     9-12, 1990, poster I-B80 (unpublished).

[17] F.M. Mueller, A.P.S. Meeting, spring 1990.

[18] W. Waeber and U. Zimmermann eds, Helv. Phys. Acta <u>63</u>, pp377-
     470 (1990).

MEASUREMENT OF THE LOCAL ELECTRON SPIN POLARIZATION

BY THE SCANNING TUNNELING MICROSCOPE

R. Wiesendanger, H.-J. Güntherodt, G. Güntherodt[*],
R.J. Gambino[**], and R. Ruf[**]

Institute of Physics, University of Basel,
Klingelbergstrasse 82, CH-4056 Basel, Switzerland
[*] II. Institute of Physics RWTH Aachen, D-5100 Aachen,
Federal Republic Germany
[**] IBM T.J. Watson Research Center, Yorktown Heights,
New York 10598, USA

Abstract: We show that the scanning tunneling microscope (STM) can
be made sensitive to the electron spin and therefore to magnetic
structures on the atomic scale. This is demonstrated by the
observation of vacuum tunneling of spin-polarized electrons with a
STM operated in ultrahigh vacuum. A ferromagnetic CrO_2 tip
providing electrons of high spin polarization and a Cr(001) single
crystal surface which offers an ideal magnetic test structure are
used. We have derived an expression relating the product of the
electron spin polarizations of the two electrodes with quantities
directly measurable with the STM.

1.   Introduction

Since the invention of scanning tunneling microscopy (STM) by
G. Binnig, H. Rohrer and coworkers [1], the question arose, whether
this technique can also be made sensitive to the electron spin
offering the opportunity to study magnetic structures, for instance
antiferromagnetic spin configurations, down to the atomic scale.
However, the special requirements for the STM tip, the sample and
the environment have prevented the observation of spin-dependent
vacuum tunneling by STM so far. Here, we report the first
observation of vacuum tunneling of spin-polarized electrons with a
STM operated in ultrahigh vacuum. Moreover, we give an expression,
relating the product of the electron spin polarizations of tip and
sample surface with quantities directly measurable with the STM.
As a consequence, the local spin polarization of the free surface
can be determined in contrast to experiments using planar tunneling
junctions (either superconductor-oxide-ferromagnet- [2] or
ferromagnet-oxide-ferromagnet junctions [3]) which yield the spin
polarization averaged over the entire oxide covered surface.

2.   Experiment

The experiments were performed in a multichamber UHV system (NANOLAB) with several surface preparation and analysis facilities and a background pressure in the low 10^{-11} mbar range [4]. The calibration of the STM scanning unit was performed by imaging the Si(111)7x7 [5] and the Si(001)2x1 [6] surface structures. The noise level of the instrument is well below 0.01 nm, demonstrated by imaging the atomic structure of the Au(111) surface with a measured corrugation of the order of 0.02 nm [4].

The central point for the demonstration of spin-dependent vacuum tunneling with the STM is the choice of the magnetic probing tip and the magnetic test structure. We used a ferromagnetic CrO_2 tip consisting of a flat CrO_2 film with in-plane magnetization hanging over a Si(111) substrate having the shape of a tip [7]. Recent spin-resolved photoemission experiments on similar CrO_2 films showed a spin polarization of nearly 100% for binding energies near 2 eV below the Fermi level E_F [8]. A positive sample bias voltage of about 2 - 3 V was applied in the present STM experiment to allow tunneling of these electrons with high spin polarization. For comparison, we have used electrochemically etched tungsten tips as nonmagnetic probes.

An ideal magnetic test structure was given by the Cr(001) single crystal surface. S. Blügel et al. [9] showed on the basis of self-consistent total-energy calculations that topological antiferromagnetism between ferromagnetic terraces separated by monoatomic steps (fig. 1) is the energetically most favourable structure of this surface. Our topographic STM studies of the clean Cr(001)1x1 surface performed with a tungsten tip [10] strongly support this microscopic model with terraces separated mainly by monoatomic steps of 0.144 nm height, which corresponds to the separation between the top surface layer and the second layer of opposite magnetization built up by the atoms in the body-centered cubic positions of antiferromagnetic bcc Cr (fig. 2). The topological antiferromagnetism of the Cr(001) surface with terraces alternately magnetized in opposite directions provides a well-defined magnetic test structure. The demonstration of spin-dependent vacuum tunneling with the STM can now be performed by a comparison of the STM traces obtained when a nonmagnetic tungsten tip or a ferromagnetic CrO_2 tip is scanned over the alternately magnetized terraces separated by monoatomic steps on the Cr(001) surface.

3.   Results and Discussion

The nonmagnetic tungsten tip only responds to the surface topography and is scanned at a constant distance s_0 over the different terraces, independent of their magnetization. Therefore, the value for the monoatomic step-height, measured with a tungsten tip, is always the same (within less than 5% experimental error) and corresponds to the topographic single step-height value of

h = 0.144 nm. With a CrO_2 tip, however, a periodic alternation of the values for the monoatomic step-height around the mean value of 0.144 nm is observed when the CrO_2 tip is scanning over the alternately magnetized terraces (fig. 3b). The deviations from the topographic monoatomic step-height value measured with a CrO_2 tip can be as large as ±15% which is outside the range of scatter of the monoatomic step-height values measured with a tungsten tip. Furthermore, a periodic alternation of the step-height values, as reproducibly observed in successive line scans with the CrO_2 tip, has never been found in topographic STM traces measured with a tungsten tip.

We attribute this periodic alternation of the monoatomic step-height values, as observed with a CrO_2 tip, to an additional contribution from spin-dependent tunneling (fig. 3a). If the CrO_2 tip is scanning over a terrace with the same magnetization direction as present for the front part of the tip, the tunneling current $I_{\uparrow\uparrow}$ will be increased compared to the current I_0, which would be measured without a spin-dependent contribution [3]. Since the STM is operated at constant current, an additional contribution to the tunneling current leads to a corresponding increase Δs_1 of the mean distance s_0 between the tip and the sample surface. If the CrO_2 tip is scanning over a terrace having the opposite direction of magnetization, the tunneling current $I_{\uparrow\downarrow}$ will be decreased, leading to a corresponding decrease Δs_2 of the distance between tip and sample surface. The measured monoatomic step-height values therefore alternate between $h_1 = h + \Delta s_1 + \Delta s_2$ and $h_2 = h - \Delta s_1 - \Delta s_2$, where h is the topographic monoatomic step-height. It can be shown [11] that the relationship between the electron spin polarizations P_A, P_B of the two electrodes A, B (A: tip, B: sample) and Δs_1, Δs_2 is given by:

$$P_A \cdot P_B = \frac{\exp\left(A\sqrt{\phi}\,\Delta s\right) - 1}{\exp\left(A\sqrt{\phi}\,\Delta s\right) + 1},$$

where ϕ is the mean local tunneling barrier height, $\Delta s = \Delta s_1 + \Delta s_2$ and $A \approx 1$ eV$^{-1/2}$ Å^{-1}. Therefore, by measuring Δs and ϕ with the STM, the product $P_A P_B$ can directly be derived. With the CrO_2 tip and the Cr(001) single crystal surface, we have obtained values for $P_A P_B$ of up to 20%. Assuming an electron spin polarization of about 90% for the CrO_2 tip at a bias voltage of +(2 − 3) V [8], we derive a maximum spin polarization of 22% for the Cr(001) surface, consistent with absolute values of published data [12,13].

4. Summary

In summary, we have demonstrated that the STM can be made sensitive to the electron spin by the observation of vacuum tunneling of spin-polarized electrons. We expect that by improving the sharpness of the ferromagnetic probing tips, in-plane antiferromagnetic structures will also be accessible for magnetic STM studies. The application to the novel high-T_c superconductors seems particularly promising.
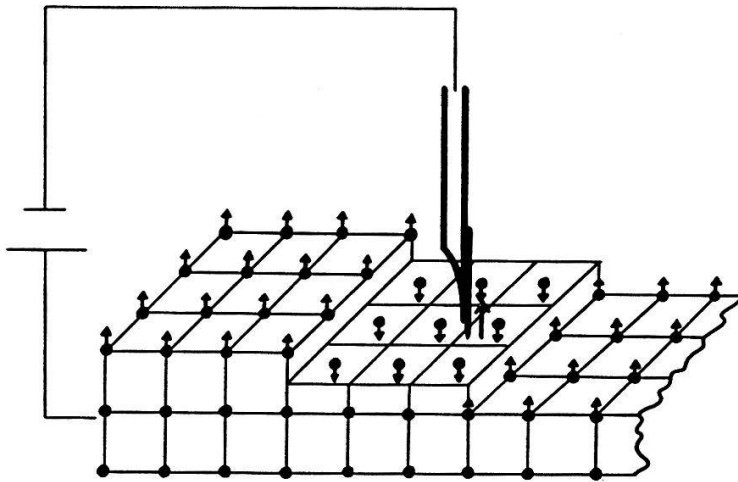
Fig. 1:
A ferromagnetic CrO_2 tip is scanned over the alternately magnetized terraces of a Cr(001) surface. These terraces are separated by monoatomic steps of 0.144 nm height.
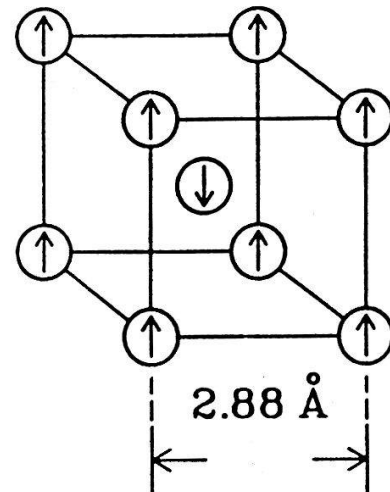

Fig. 2:
Spin-lattice of antiferromagnetic Cr. The topmost atoms define the (001) crystal plane.
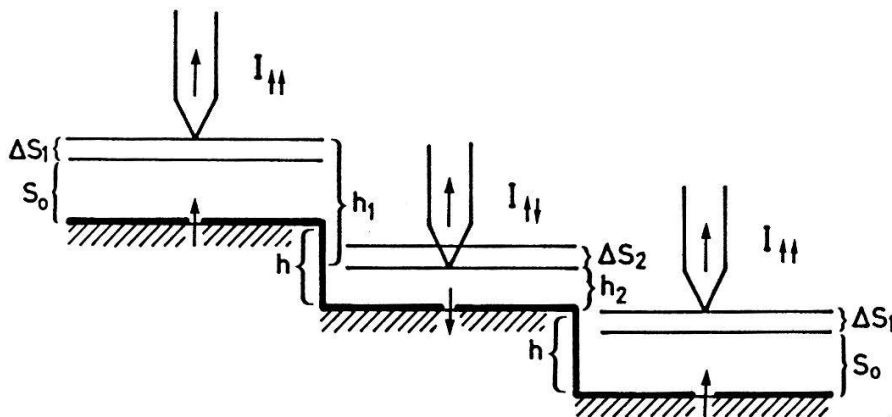

Fig. 3a:
With a ferromagnetic tip scanned over alternately magnetized terraces, the measured step-height value is not identical with the topographic step-height h but alternates between $h_1 = h + \Delta s_1 + \Delta s_2$ and $h_2 = h - \Delta s_1 - \Delta s_2$ due to an additional contribution from spin-dependent tunneling.
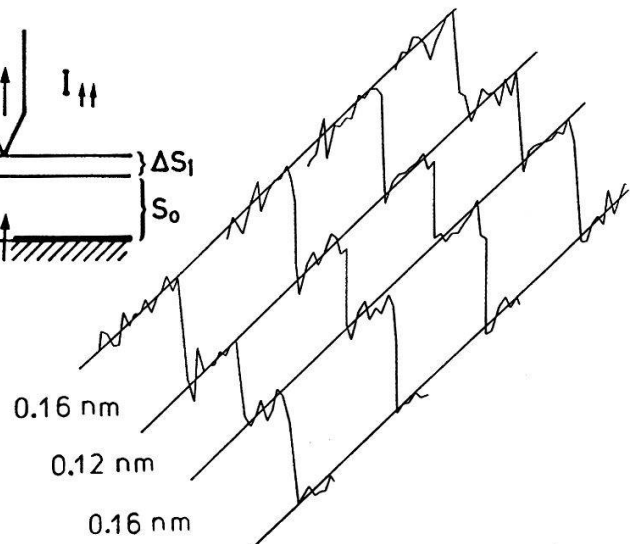
Fig. 3b:
Successive STM line scans at constant current over the same three monoatomic steps on a Cr(001) surface obtained with a ferromagnetic CrO_2 tip. The same alternation of the measured step-height value in all single line scans is evident.

5.   Acknowledgements

6.   References

[1] G. Binnig, H. Rohrer, Ch. Gerber, and E. Weibel,
    Phys.Rev.Lett. 49, 57 (1982).
[2] P.M. Tedrow and R. Meservey, Phys.Rev.Lett. 26,
    192 (1971).
[3] M. Julliere, Phys.Lett. 54A, 225 (1975).
    S. Maekawa and U. Gäfvert, IEEE Trans.Magn. MAG-18,
    707 (1982).
    J.C. Slonczewski, J. de Phys. C8, 1629 (1988).
[4] R. Wiesendanger, G. Tarrach, D. Bürgler, T. Jung,
    L. Eng, and H.-J. Güntherodt, Proc. IVC-11/ICSS-7,
    Cologne, W-Germany, Vacuum (in press).
    R. Wiesendanger, D. Bürgler, G. Tarrach, D. Anselmetti,
    H.R. Hidber, and H.-J. Güntherodt, Proc. STM'89,
    J.Vac.Sci.Technol. A8, 339 (1990).
[5] R. Wiesendanger, G. Tarrach, D. Bürgler, and
    H.-J. Güntherodt, Europhys.Lett. (in press).
[6] R. Wiesendanger, D. Bürgler, G. Tarrach, and
    H.-J. Güntherodt, Surf.Sci. (in press).
[7] The preparation of these CrO_2 tips will be described
    in a forthcoming publication.
[8] K.P. Kämper, W. Schmitt, G. Güntherodt, R.J. Gambino,
    and R. Ruf, Phys.Rev.Lett. 59, 2788 (1987).
[9] S. Blügel, D. Pescia, and P.H. Dederichs, Phys.Rev. B39,
    1392 (1989).
[10] R. Wiesendanger and H.-J. Güntherodt, submitted for
    publication.
[11] R. Wiesendanger, H.-J. Güntherodt, G. Güntherodt,
    R.J. Gambino, and R. Ruf, submitted for publication.
[12] F. Meier, D. Pescia, and T. Schriber,
    Phys.Rev.Lett. 48, 645 (1982).
[13] C. Rau and S. Eichner, Phys.Rev.Lett. 47, 939 (1981).

STM AND LUMINESCENCE

D.L. Abraham, S.F. Alvarado, C. Schönenberger, D.J. Arent, and H.P. Meier

IBM Research Division, Zurich Research Laboratory, Säumerstrasse 4,
CH-8803 Rüschlikon, Switzerland

Abstract: We report the observation of luminescence in scanning electron microscopy on GaAs/AlGaAs heterostructures.

Recently, the STM was used to induce light emission associated with inverse photoemission and fluorescence processes due to decay of plasmons in metals [1]. Here, spatial resolution in the nanometer range was demonstrated. For the case of semiconductors, tunneling into the conduction band electron-hole recombination across the direct band gap can give rise to luminescence. STM measurements of III-V heterostructures show that luminescence can be induced within single quantum wells of dimensions down to a few nm in width and can also be used to image them [2]. The measurements are performed in UHV conditions, with $p = 10^{-10}$ to 4×10^{-11} Torr, using a "pocket size" type STM [3] . An airlock is attached to the main chamber and allows the introduction of samples and tips. Tips were made of 0.25 mm tungsten wire by electrochemical etching. We used a multiquantum well test structure consisting of $Al_{0.38}Ga_{0.62}As/GaAs(100)$ pairs of various widths (2 nm, 5 nm, 10 nm, 20 nm, 50 nm, and 100 nm) all heavily doped, $p \simeq 10^{-19}cm^{-3}$, i.e. $E_F \simeq$ top of valence band energy. The substrate is (001) GaAs. Clean (110) surfaces were produced by cleaving the wafers (thinned to about 150 μm) in situ. For the luminescence intensity measurement at room temperature, a collector lens, subtending a solid angle of about 0.2 sr, was mounted a few centimeters from the tunneling junction. The maximum optical responsivity of the detection system is centered at $hv = 1.56 \pm 0.14$ eV, i.e. the images and spectra shown here are made by measuring the luminescence caused by recombination within the quantum wells. Electroluminescence is observed upon electron injection into the bulk conduction band of the semiconductor. Luminescence intensity vs. tunneling voltage measurements at constant tunneling current allow the position of the bulk conduction bands to be determined: Fig. 1 shows typical results obtained for GaAs and

$Al_{0.38}Ga_{0.62}As$. The threshold of luminescence occurs at a potential closely corresponding to the band gap of the III-V compound: $E_g = 1.42\,eV$ for GaAs and $E_g = 1.9\,eV$ for $Al_{0.38}Ga_{0.62}As$, as would be expected when injecting electrons into heavily doped III-V compounds. The GaAs spectrum shown exhibits a weak step at $V_T \simeq -2.8\,eV$ and a clear rise in intensity with threshold at $V_T \simeq -4.5\,eV$. These features are most probably associated with impact ionization of electron-hole pairs. This process increases the number of conduction electrons available for luminescence. The first step is usually very weak and does not clearly appear in most spectra. The feature at $V_T \simeq -4.5\,eV$, however, is clearly reproducible. We note that it is also possible to tunnel into $Al_{0.38}Ga_{0.62}As$ at potentials corresponding to injection of electrons at energies below the bulk conduction band. This suggests that there is band bending at this surface as reported by Albrektsen et al. [4] based on measurements taken on the same sample. Nevertheless, as shown in Fig. 1, the luminescence threshold occurs at a tip potential corresponding to the energy of the bulk conduction band. Thus a fraction of the electrons tunneling into the AlGaAs(110) surface can ballistically cross the band-bending region and reach the wells for recombination only when their energy is higher than the energy of the bottom of the conduction band in the bulk, see Fig. 2. Fig. 3 shows a luminescence image of the $Al_{0.38}Ga_{0.62}As/GaAs(100)$ heterostructure. For this measurement the STM was operated in the constant current mode. The typical measurement time is 10 to 20 min. The high resolution of the luminescence pictures as well as the dependence of the image contrast on the tunneling voltage can be qualitatively explained in the context of the band structure at the surface/interface region.
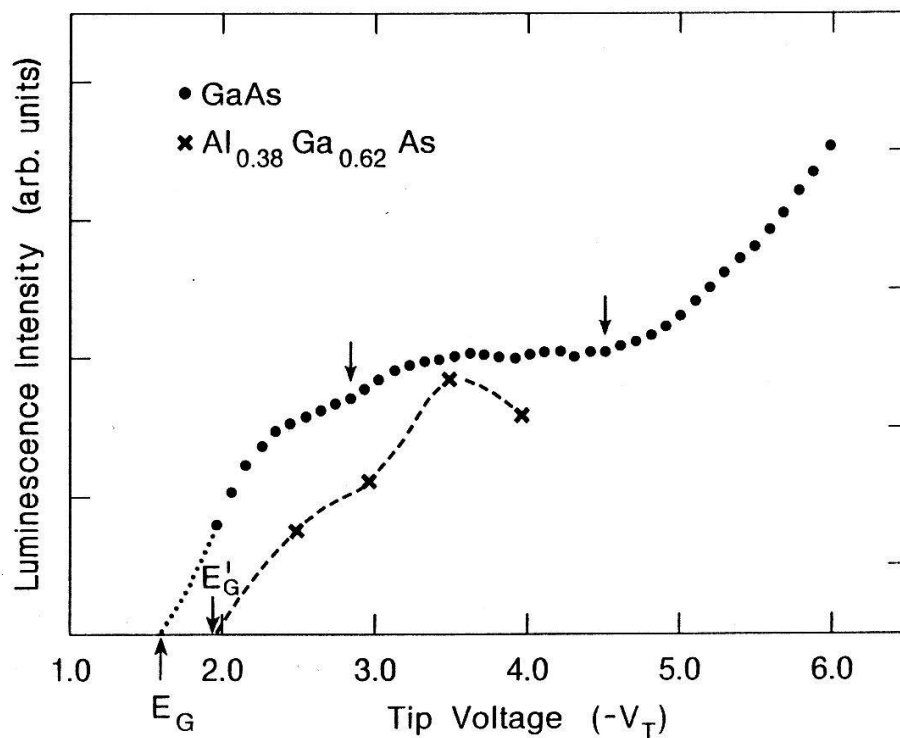

Fig. 1

Damaged or contaminated regions of the surface appear darker in the luminescence images, see the dark spots in the 10 nm well, indicating trapping at those surface perturbations. These results open up new possibilities for the study and characterization of semiconductors and devices by local luminescence efficiency and spectroscopy.
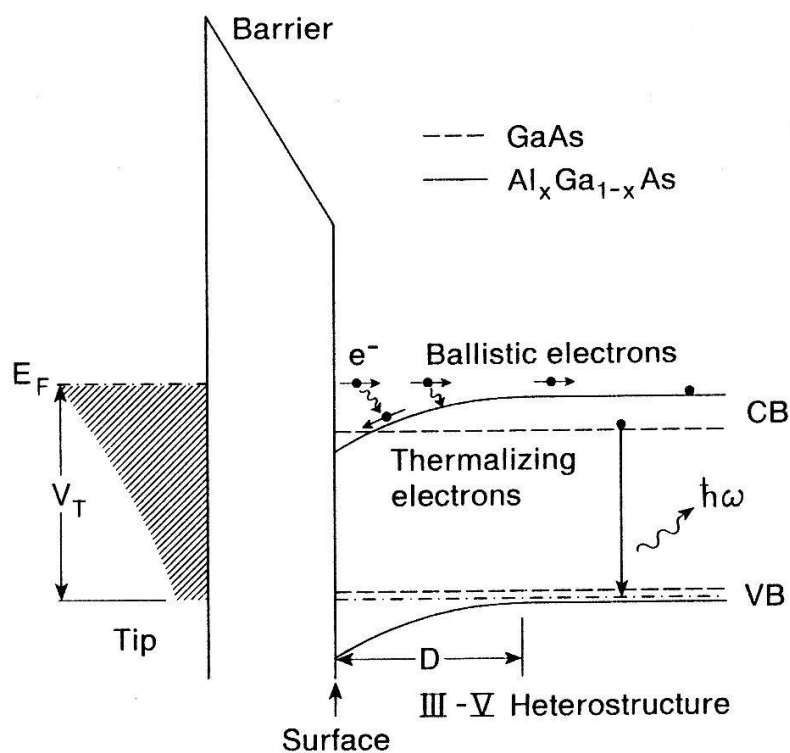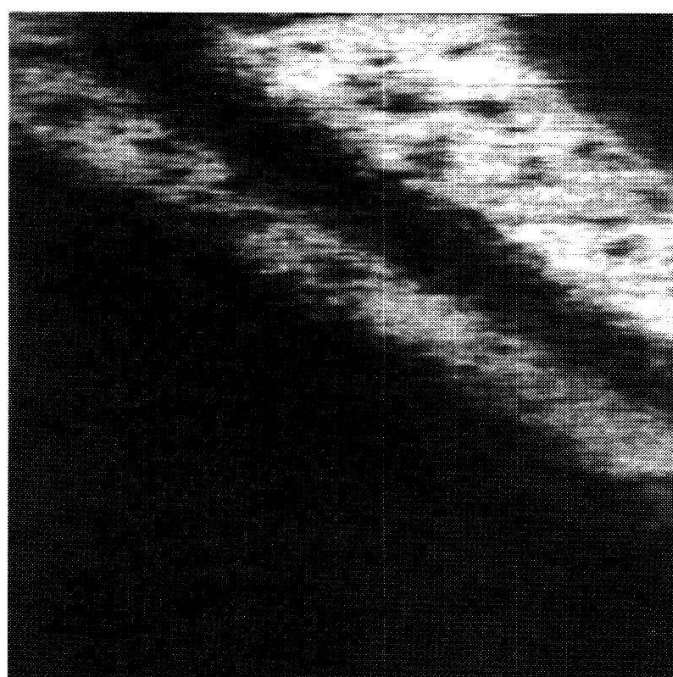

Fig. 2

Fig. 3

References

[1] J.K. Gimzewski, B. Reihl, J.H. Coombs, and R.R. Schlittler, Z. Phys. B — Condensed Matter **72**, 497 (1988); J.H. Coombs, J.K. Gimzewski, B. Reihl, J.K. Sass and R. Schlittler, J. Microscopy **152**, 325 (1988). Field emission from a tip to induce local photon emission was first proposed by R. Young, Physics Today, November 1971, p. 42.

[2] D.L. Abraham, A. Veider, Ch. Schönenberger, H.P. Meier, D.J. Arent and S.F. Alvarado, Appl. Phys. Lett., in print.

[3] Ch. Gerber, G. Binnig, H. Fuchs, O. Marti, and H. Rohrer, Rev. Sci. Instrum. **57**, 221 (1986).

[4] O. Albrektsen and H. Salemink, Appl. Phys. Lett., in print.

CARACTERE NON METALLIQUE DES CLUSTERS
DE PLATINE Pt$_n$ (n = 1 à 6)

P. Fayet[a], W. Eberhardt, D.Cox, Z. Fu, D. Sondericker, R. Sherwood,
A. Kaldor. Exxon Research and Engineering Co., Annandale, N.J.,
08801, USA. a) Université de Lausanne, Institut de Physique
Expérimentale, 1015 Lausanne-Dorigny.

Résumé: L'émission photoélectrique produite par radiation
synchrotron nous a permis de déterminer l'énergie de liaison des
électrons 4f ainsi que l'énergie des niveaux de valence du platine
en fonction de la taille des amas. De ces mesures nous concluont que
les petits amas de platine Pt$_n$ (n = 1 à 6) ne présentent pas encore
de caractère métallique.

Dans cet article nous décrivons un moyen d'étudier à partir de
quelle taille le caractère métallique apparaît dans les petits
clusters d'élément de transition. Nous avons mesuré l'émission
photoélectrique des niveaux de coeur 4f et le sommet des bandes de
valence des clusters de platine Pt$_n$ déposés sur des supports de
Si(100) naturellement oxydé [1]. Chaque échantillon est le produit
de l'exposition d'une pièce de Si(100) à un faisceau moléculaire de
clusters Pt$_n^+$ sélectionnés en taille (n = 1 à 6). Ils ont été
déposés à une énergie de 10±5 eV sur la surface de SiO$_2$ et à un
recouvrement équivalent à 10% d'une monocouche atomique de platine.
Toutes les dépositions et les mesures de photoémission ont été
réalisées à température ambiante.

Les positions en énergie des raies spectrales des niveaux de
coeur 4f$_{7/2}$ du platine pour les clusters Pt$_1$ à Pt$_6$ sont présentées à
la fig. 1a). Cette figure montre de plus que la largeur de la raie
4f$_{7/2}$ diminue de manière linéaire lorsque la taille des amas
augmente. Les valeurs discrètes des énergies obtenues et la
variation linéaire de la largeur des raies spectrales prouvent que
la plupart des clusters survivent sans fragmentation à la déposition
et que les clusters ne frittent pas après la déposition: l'indivi-
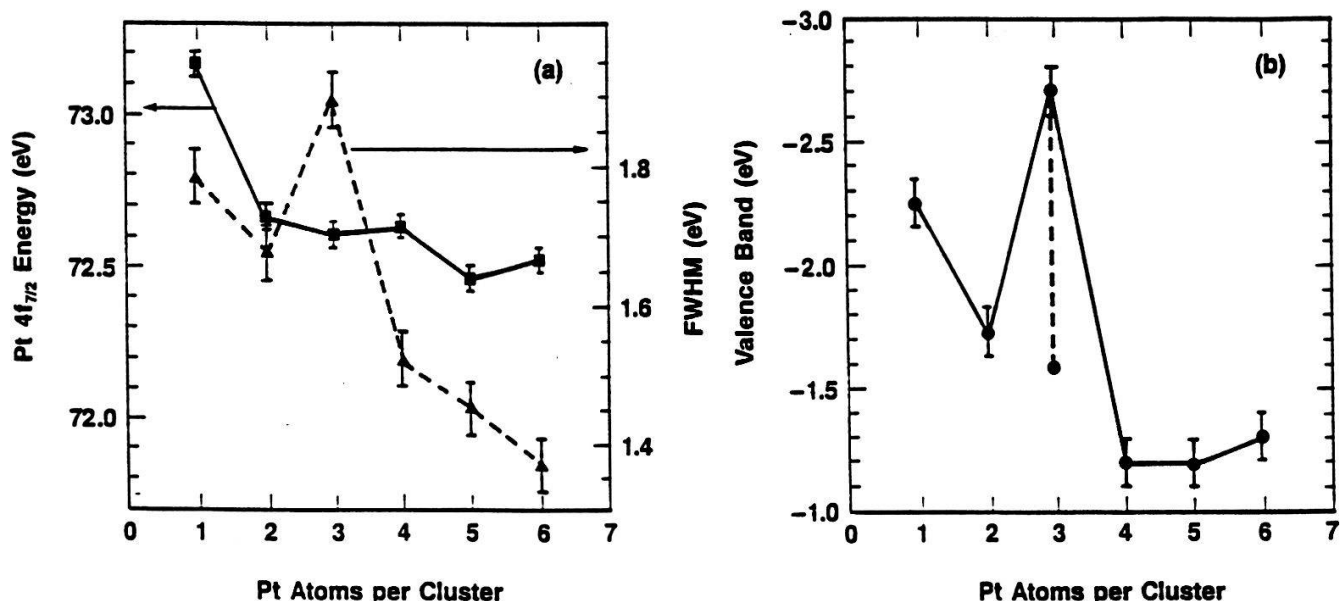dualité des amas est conservée dans ce processus.

Fig. 1.a) Position en énergie et largeur (FWHM) des raies spec-
trales des niveaux $4f_{7/2}$ pour les clusters déposés sur le
SiO_2 en fonction de la taille des clusters. Ces mesures ont été
effectuées à 280 eV d'énergie des photons incidents. La position
du solide métallique est à 71.2 eV et la largeur de raie vaut
moins que 0.5 eV.   (b) Seuils de la densité d'états des
électrons de valence en fonction de la taille des clusters
mesurés à 40 eV. L'énergie de liaison de l'électron aux clusters
est donnée par la valeur ci-dessus augmentée de 5,1 eV (niveau
de Fermi du substrat).   Cette figure provient de la réf. (1).

La position du sommet des bandes de valence est présentée à la
fig. 1b). Ces valeurs sont éloignées de la position du niveau de
Fermi du métal massif. De plus sur les spectres de photoémission, le
sommet de la densité d'états ne montrent pas la particularité de la
fonction escalier du niveau de Fermi du métal. Ces faits sont une
conséquence directe du caractère non métallique de ces petits amas.

Les expériences de photoémission ont été effectuées sur la
ligne U1 du NSLS à Brookhaven National Laboratory, USA.

Références

[1] W. Eberhardt, P. Fayet, D.M. Cox, A. Kaldor, R. Sherwood and D.
Sondericker, Phys. Rev. Lett. 64, 780 (1990); Physica Scripta à
paraître.

TIME OF FLIGHT (TOF) SPECTROMETER FOR MOLECULAR ADSORPTION KINETICS MEASUREMENT

B. Calpini, M. Croci, R. David*, R. Monot

*Institut de Physique Expérimentale, Ecole Polytechnique Fédérale de Lausanne, 1015 Lausanne; *Permanent address : Forschungszentrum Jülich, D-5170 Jülich*

Abstract : Molecular Beam Relaxation Spectroscopy (MBRS [1]) implies the precise knowledge of the beam characteristics. By using a 50 % duty cycle chopper with the molecular source on line with a quadrupole mass spectrometer, the direct beam can be fully characterized. This is illustrated by a helium supersonic beam (v = 1750 m/s and S ≅ 15).

Experimental setup

A schematic view of the apparatus used in this study is shown in fig. 1. It consists of a 4 pumping stages experiment : chamber 1 (CH 1) contains a nozzle beam ① (stagnation pressure up to 10 bars, 50 μm diam. nozzle) and the skimmer ② (500 μm diam.); a chopper ③ is enclosed in CH 2 and is defined as the "zero flight path" of our experiment; CH 1 and 2 are rotatable around the center of CH 3, the reaction chamber; CH 4 contains an Extranuclear Quadrupole Mass Spectrometer (QMS) (④ = ionizer, ⑤ = quad. filter, ⑥ = electronmultiplier), which can be moved from L_m = 180 mm to L_M = 480 mm with L defined as the flight path between chopper and ionizing region.
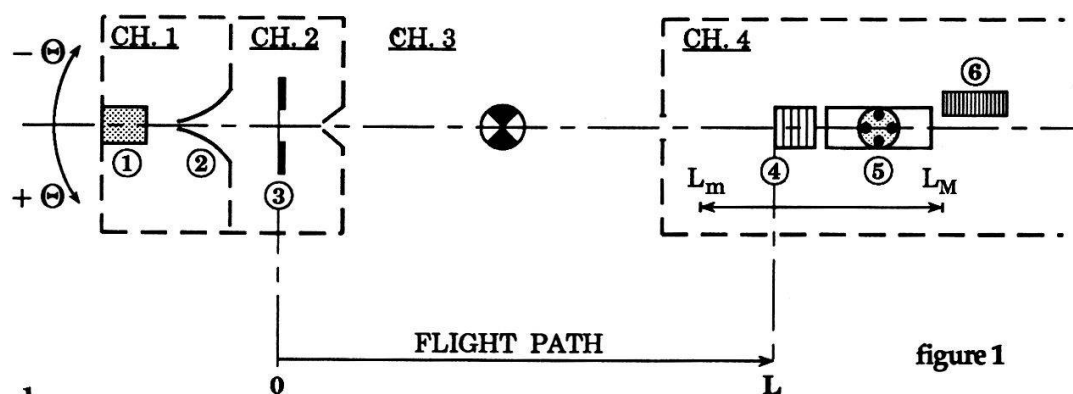

figure 1

Method

Measuring the direct molecular beam with an axial ionizer (density detector) the speed distribution of the particles in the beam is :

$$\frac{dn}{dv} \div v^2 \exp\left[-\left(\frac{v}{v_T} - S\right)^2\right] \tag{1}$$

where v_T is the thermal speed in the beam and the speed ratio S is a direct measure of the "quality" of the beam. From eq. (1) the distribution of the time of flight correlated to this speed distribution is given by

$$\frac{dn(t)}{dt} \div t^{-4} \exp\left[-\left(\frac{L}{v_T t} - S\right)^2\right] \tag{2}$$

Measuring at a distance L the experimental signal n_{exp} (t) and derivating this signal we get :

$$\frac{d\,n_{exp}}{dt} = \left(\frac{dg}{dt} * \frac{dn}{dt} \right) \left[\; t - t_{QMS}\,(m) \;\right] \qquad (3)$$

where g is the gate function and t_{QMS} (m) the time spent in the QMS for a given gas of mass m . To estimate t_{QMS} (m) we produce a seeded beam (He =

96 %; CO + Ar + Kr = 4 %) at $P_{stag.}$ = 8 bar. All species in the beam will arrive at the <u>same</u> time in the ionizer [3], but will be detected for higher mass, according to the relation t_{QMS} (m) = $\alpha \sqrt{m}$ [2]. For an ion energy of 10 eV we measured $\alpha = 8 \pm 0.3$ for L = 200, 300 and 400 mm (fig. 2).
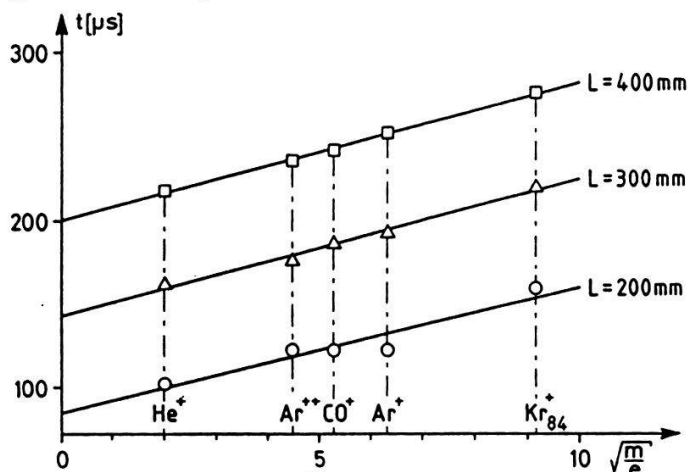
figure 2

As a result of this "calibration" experiment we present in fig. 3 the experimental time of flight distribution (o) for a He beam ($P_{stag.}$ = 8 bar) with a flight path of L = 300 mm. The convolution function (CONV.) is obtained by eq. (3). We measure $S \cong 15$ with L/t_{mp} = 1750 m/s (m.p. = most probable). For high S , this speed is converging to the value $a = \sqrt{\dfrac{5\,kT_0}{m}}$ (monoatomic gas with T_0 = nozzle temperature and k = Boltzmann constant). Fig. 4 shows the $\dfrac{L}{a}$ line and the experimental points of measurement (□) for different L.
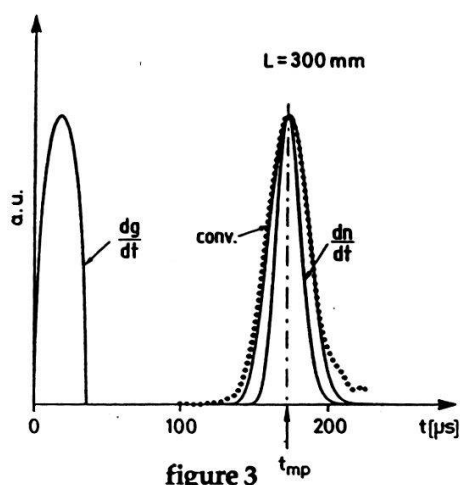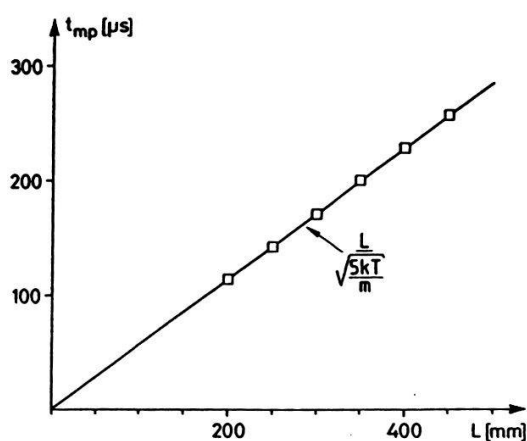

figure 3

figure 4

References

[1]   L.K. Verheij, J. Lux, A.B. Anton, B. Poelsema, G. Comsa, Surf. Science **182** (1987) p. 411.

[2]   F. Huisken, T. Pertsch, Rev. Sci. Instr. **58** (1987) p. 1038.

[3]   F. Huisken, T. Pertsch, J. Chem. Phys. **86** (1987) p. 106.

SCANNING TUNNELING MICROSCOPY/SPECTROSCOPY OF TITANIUM IN AIR

M. Jobin, R. Emch, F. Zenhausern, S. Steinemann* and P. Descouts

GAP Biomédical, Université de Genève, 20 rue de l' Ecole-de-Médecine, CH 1211 Genève 4.

* Institut de Physique expérimentale, Université de Lausanne, CH 1015 Lausanne.

Abstract: We present STM images and STS measurements on electropolished Ti which indicate that the native Ti-oxide behaves as a n-type semi-conductor with a surface band gap of about 0.8 eV.

1.   Introduction

Ti and Ti-alloys are particulary suitable metallic biomaterials because of good corrosion resistance in tissue, absence of tissue toxicity, good strength and low elastic modulus [1]. The biocompatibility of Ti is directly related to the thin amorphous film of native oxide TiO_2 wich forms spontaneously in air and has a specific resistivity of 1E15 [ohm cm] for a film thickness of 5-10 nm [2]. At Geneva University we have developed a STM coupled with a high resolution reflective optical microscope to investigate some aspects of the interface between biomaterials and living tissue [3]. With this STM we have reached atomic resolution in air on HOPG and we have also succeeded in imaging a protein (Fibronectin) deposited on mica and coated with a conductive layer [3]. We present in this paper STM images of Titanium in air and some preliminary spectroscopic measurements of the native Ti-oxide layer.

2.   Results

Fig. 1 shows a high resolution STM image of an electropolished Ti sample. We can observe on this sample relatively flat surfaces with a corrugation of about one nanometer which opens the possibility of imaging adsorbed proteins. To understand the mechanism of the STM image formation on Ti oxide we made STS measurements by performing I(V) curves with our STM taken for various tip-sample separations. These I(V) curves show a typical n-type semi-conductor behaviour. From these curves we can calculate a normalized conductivity $(dI/dV)/(I/V)$ wich gives in our case a surface band gap of 0,8 eV, quite smaller than the bulk band gap of TiO_2 (3,05 eV).
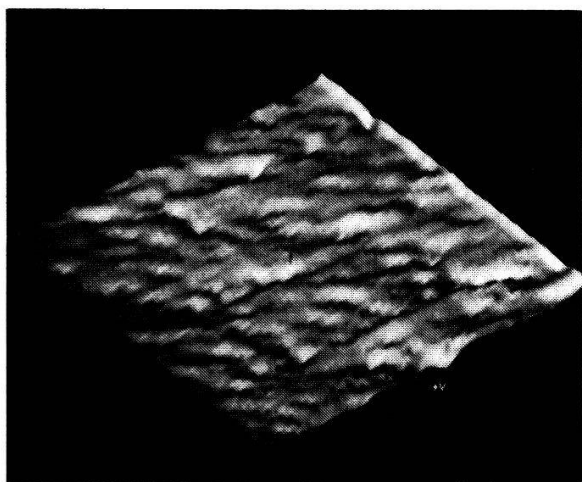
Fig 1 : High resolution STM image of
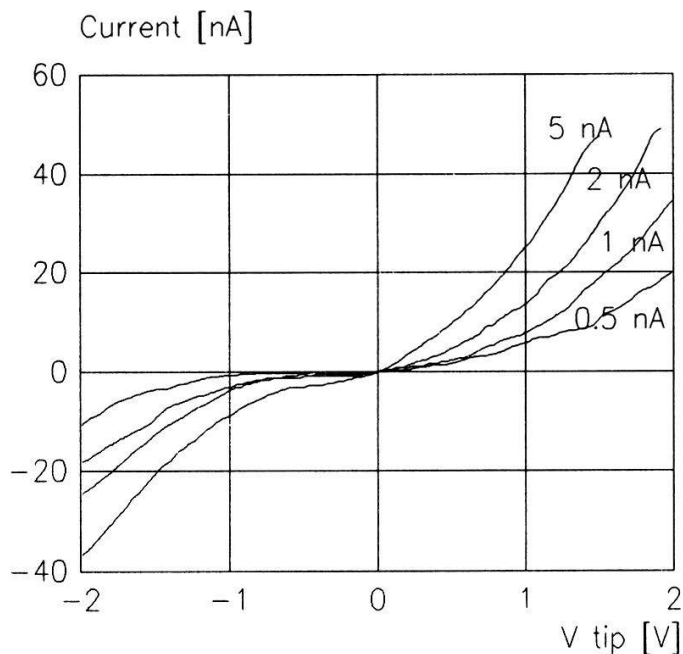electropolished Ti in air (20 nm x 30 nm)

Fig 2 : I(V) curves for various tip-sample
separations. (5 nA-shortest separation)

For the spectroscopic measurements, the tip voltage was 500 mV with different values of
the tunneling currents as indicated in Fig 2 which determine the tip-sample separation.
The feedback loop is interrupted while the voltage ramp is applied on the tip.

3.   Discussion

    To analyse the spectroscopic results obtained with the STM in air we have to take
into account the fact that in air the Ti oxide is always hydroxylated and that ions are very
mobile at the surface of the oxide. Surface defects could be created by the high electric
field between the tip and the sample and the induced surface states be responsible for the
semi-conductor behaviour. For a better control of this oxide, STM/STS experiments
under UHV are now in progress.

5.   References

[1]   S.G. Steinemann, Titanium Science and Technology, vol. 1-4, 1373 (1985).
[2]   S.G. Steinemann, P.A. Mausli, Proc. 6th. World Conf. on Titanium, Ed. de
        Physique, 535 (1988).
[3]   R. Emch et al., J. Vac. Sci. Technol. A8(1), 655 (1990).

ATOMIC FORCE MICROSCOPY:
HIGH RESOLUTION AND CONTRAST MECHANISM

E. Meyer, H. Heinzelmann, D. Brodbeck, G. Overney, L. Howald and H.-J. Güntherodt
Institut für Physik, Universität Basel, Klingelbergstrasse 82, CH-4056 Basel, Switzerland

Abstract: Atomic force microscopy (AFM) is a new technique which allows the examination of insulators as well as conductors in real space. In comparison to the scanning tunneling microscope (STM) the instrument probes the force while the STM probes the tunneling current, both on a local scale. Until recently atomic resolution has been restricted to layered materials such as graphite, boron nitride, $MnPS_3$ or transition metal dichalcogenides. Now we succeeded in resolving the surface of a nonlayered structure on an atomic scale. The AFM measurements of LiF(100) will be described and compared with different surface sensitive methods such as helium scattering. The experimental results allow conclusions about the contrast mechanism of the AFM and give some indications for the theory.

The atomic resolution on layered materials such as graphite and boron nitride [1] has shown the great potential of AFM in surface science. The fundamental contrast mechanism of this technique is still under investigation. Originally it has been proposed that the AFM probes the total charge density. Recent experiments on graphite [2] and the transition metal dichalcogenides [3] have shown that there exist some deviations from this model. On the other hand theoretical investigations [4] have shown that the disturbance of the electronic and atomic structure by the tip is significant. Using a continuum elasticity theory in combination with *ab initio* calculations Tománek *et al.* [5] have shown that in AFM typical forces of $10^{-8}N$ will yield long ranged elastic deformations on layered materials. Abraham *et al.* [6] could indicate an upper limit of $\approx 2 \cdot 10^{-8}N$ for a monoatomic tip. For higher loadings the layer will be punctured. Experimentally the force could be varied from $5 \cdot 10^{-9}$ to $10^{-7}N$ without observing a destruction of the tip or sample. It has been proposed that the tip punctures the layer and shears layer against layer [7]. As an alternative it has been suggested that the AFM has a blunt tip, probably a flake of the sample, which allows the high loadings [6]. A nonlayered structure such as LiF is an ideal candidate to disentangle the different explanations. These structures will not have long ranged elastic deformations and exclude the presence of flakes which are natural for the layered materials.

The experimental technique has been described previously [8]. As force sensor we have used microfabricated SiO_2 lever with a spring constant of about $1N/m$. The applied force between probing tip and sample was approximately $10^{-8}N$. Fig. 1 shows a $15 \times 21 Å^2$ area of LiF(100). The distance between the protrusions is $2.8 \pm 0.1 Å$, which corresponds well to the distance between equally charged ions of $2.84 Å$. The size of the ions can be estimated by the common hard sphere model. The ionic radius of F^- is $1.33 Å$ while Li^+ has a radius of $0.68 Å$. Therefore the protrusions can be attributed to the fluorine ions. The smaller Li^+ is hidden between the large fluorine ions and could not be imaged in our experiment. The AFM measurements are in agreement with heliumscattering and low energy electron diffraction

experiments, exhibiting an unreconstructed (1x1) surface structure. The corrugation height of 0.5 ± 0.1Å is in agreement with the helium scattering measurements. Thus for loadings of the order of 10^{-8}N the assumption that the AFM probes the total charge density seems to be reasonable. The long ranged elastic deformations which are not present in the case of LiF do not play an essential role for the contrast mechanism. Similarly the shearing of layers can be excluded. The role of the frictional forces is still unclear and has to be investigated in future.
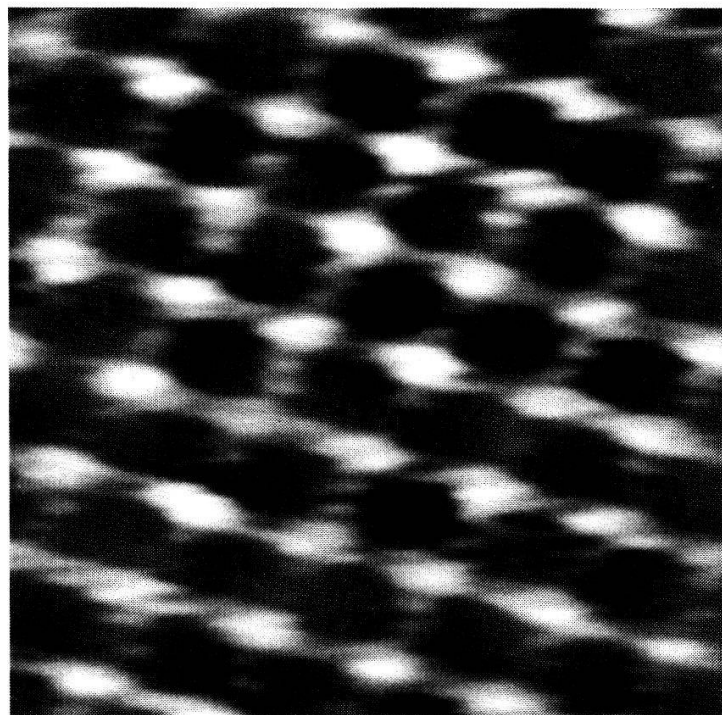
Fig. 1: AFM image on LiF(001). The corrugation height is 0.5 ± 0.1Å. The distance between the protrusions corresponds to the distance between the fluorine ions.

[1] G. Binnig, Ch. Gerber, E. Stoll, T.R. Albrecht and C.F. Quate. *Surf. Sci.* **189/190**, 1 (1987).

[2] C.M. Mate, G.M. McClelland, R. Erlandsson and S. Chiang. *Phys. Rev. Lett.* **59**, 1942 (1987).

[3] E. Meyer, D. Anselmetti, R. Wiesendanger, H.-J. Güntherodt, F. Lévy and H. Berger. *Europhys. Lett.* **9**, 695 (1989).

[4] S. Ciraci and Inder P. Batra. *Phys. Rev. B* **36**, 6194 (1987).

[5] D. Tománek, G. Overney, H. Miyazaki, S.D. Mahanti and H.J. Güntherodt. *Phys. Rev. Lett.* **63**, 876 (1989).

[6] F.F. Abraham and I.P. Batra. *Surf. Sci.* **209**, L125 (1989).

[7] J. B. Pethica and W. C. Oliver. *Phys. Scryp.* **T19**, 61 (1987).

[8] E. Meyer, H. Heinzelmann, P. Grütter, Th. Jung, Th. Weisskopf, H.-R. Hidber, R. Lapka, H. Rudin, and H.-J. Güntherodt. *J. Microsc.* **151**, 269 (1988).

THE CRITICAL FIELD OF PbMo$_6$S$_8$ MEASURED BY SPECIFIC HEAT[+]

J. CORS, D. CATTANI, M. DECROUX, B. SEEBER AND Ø. FISCHER
University of Geneva, DPMC, 1211 Genève 4
University of Geneva, GAP, 1211 Genève 4

A measurement of the initial slope dH_{c2}/dT was carried out on an homogeneous PbMo$_6$S$_8$ sample by means of a specific heat experiment. The jump in C/T at T_c was measured in magnetic fields up to 14 tesla. The results unambigously confirm PbMo$_6$S$_8$ as a high field bulk superconductor. Further, typical features of extreme type-II superconductivity are observed.
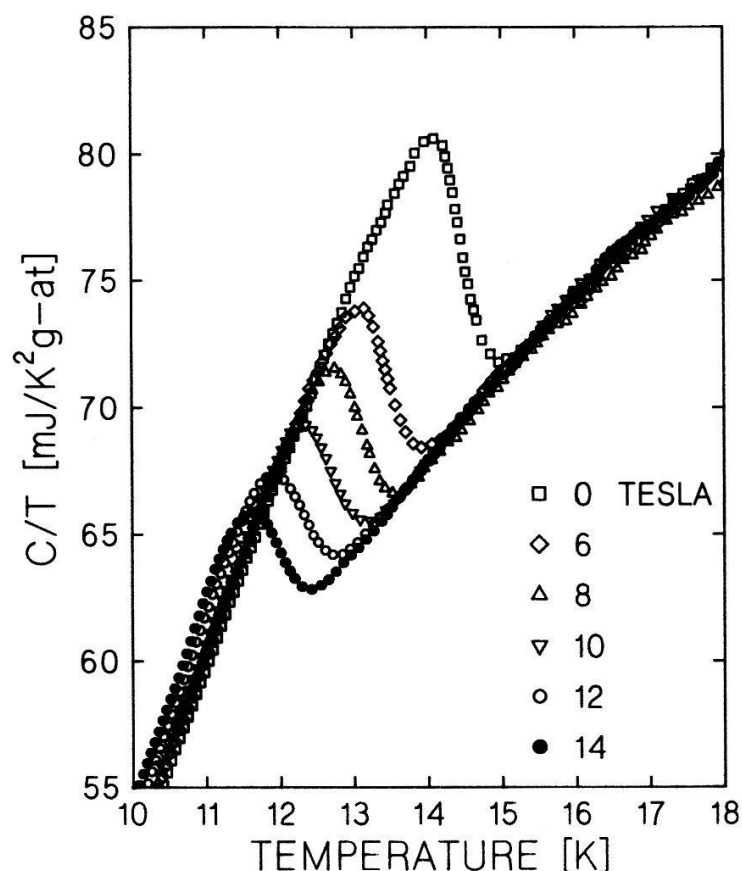
1. Experimental

PMS was synthetized at high temperatures (1600C) in powdered form. A dense bulk sample was obtained by hot-pressing at 1200C. For the measurements, a small disk weighing 30 mg was cut from the sintered pellet. A silicon chip with integrated thermometers and heater [1] was used to obtain absolute values of the heat capacity by means of the relaxation technique. The C/T versus T curves in different applied fields up to 14 tesla are shown in fig.1.

Fig.1.- C/T vs T for PbMo$_6$S$_8$ (T_c=14.5K) in magnetic fields up to 14 tesla.

2. Discussion

The peaks in C/T give evidence for the occurrence of bulk superconductivity under magnetic field. The transition width remains constant. For each field, T_c is determined by extrapolating to the idealized transition under isoentropic conditions. By using the dirty limit formula $H_{c2}(0) = 0.693\ T_c\ dH_{c2}/dT$ we obtain $H_{c2}(0)= 55$ tesla. We point out that the C/T curves of fig.1 are typical of an extreme type-II superconductor. The magnetic field does not affect significantly the specific heat below T_c. The normal cores scarcely contribute to the heat capacity of the mixed state because of the small superconducting coherence lenght $\xi_0=[\Phi_0/2\pi H_{c2}(0)]^{1/2} \cong 25$Å. Another interesting peculiarity is given by the evolution of the height of $\Delta C/T$ as a function of the applied field. The heights of $\Delta C/T$ in the mixed and in the normal state are related to each other by

$$\lim \Delta C_m/T = \Delta C_S[\ 1.16\ T\ (1-1/2\kappa^2)]^{-1}\ \text{for}\ \mu_0 H\rightarrow o\quad [2].$$

κ is of the order of 100 in $PbMo_6S_8$. As the field is reduced, the $\Delta C_m/T$ values tend to 87% of $\Delta C_s/T$, in good agreement with this equation.

3. Conclusion

The high critical field of $PbMo_6S_8$ is definitively confirmed as an intrinsic property of this compound. Our measurements of its specific heat in the mixed state reveal typical features of an extreme type-II superconductor. In this sense PMS looks similar to other superconductors like Nb_3Sn [3]. Only its upper critical field is larger by more than a factor of two.

4. References

[1] M. Decroux, this volume.
[2] K. Maki, Phys. Rev. 139 A (1965) 702
[3] M. N. Khlopkin, Sov. Phys. JETP 63 (1986) 164

CRITICAL CURRENT DENSITIES AND GRANULAR NATURE OF PbMo$_6$S$_8$+

D. CATTANI, J. CORS, M. DECROUX, B. SEEBER AND Ø. FISCHER
University of Geneva, DPMC, 1211 Genève 4
University of Geneva, GAP, 1211 Genève 4

The high upper critical field B_{c2} is now demonstrated to be an intrinsic property of the PbMo$_6$S$_8$ (PMS) Chevrel phase compound [1]. However lower values of B_{c2} determined using measurements based on macroscopic screening currents (like ac-susceptibility and critical current densities), suggest that the granular nature of this superconductor may limit transport current by possible weak links between grains. Ac-susceptibility and critical current densities measurements allow us to confirm this assumption for PMS bulk samples.
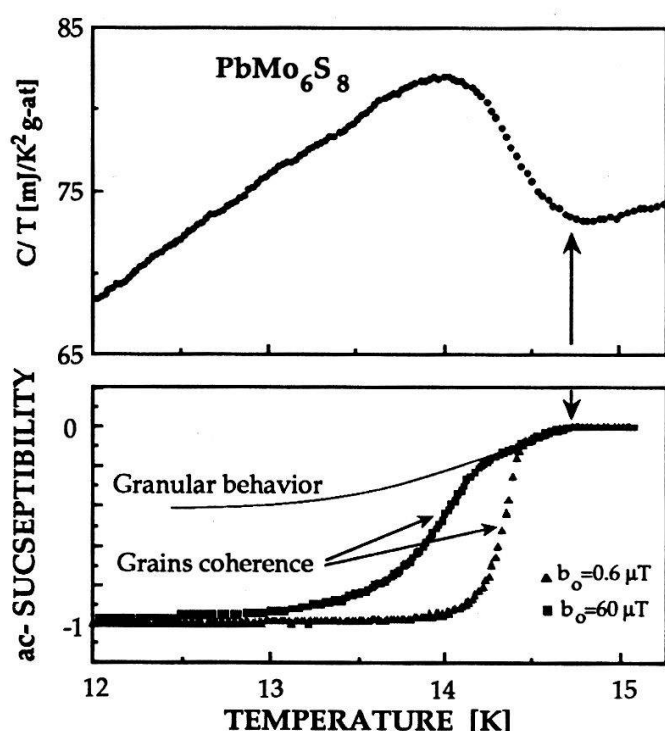

Fig. 1 Specific heat and ac-susceptibility charac-terization of an homogeneous PMS bulk sample.

1.   Experimental

The ac-susceptibility measurements reveal two steps in the superconducting transition of an homogeneous bulk sample (*fig.1*). The first part of the transition starts at the same temperature of the specific heat jump, and is independent of the ac-field amplitude. This linear response towards the field amplitudes is attributed to the screening of disconnected grains.

The following part of the transition is related to the establishment of macroscopic shielding currents through the grains boundaries. The resulting transition shift, which is not related to any structure in the specific heat curve, characterizes the coherence between the grains and is dependent of the intergrain critical current densities.

Inductive measurements of the critical current densities were carried out using the flux penetration method described by Rollins and al.[2]. In the original Bean model where only one type of macroscopic current is present in the sample, the flux penetration profile leads to a straight line, whose slope is related to j_c. In the particular case of a polycrystalline material with weak links at the grain boundaries, one gets flux profiles with two distinct linear parts, reflecting the currents across the grain boundaries and inside the grains [3].

Measurements on PMS bulk samples never show unambigously these two contributions, indicating that the ratio between them does not exceed 2 or 3 orders of magnitude. To make such a distinction possible we have measured a cold pressed homogeneous PMS powder, characterized by weakly connected grains, which allows us to estimate the intragrain j_c behavior under magnetic field. We found out that under 9 tesla, the estimated intragrain j_c was at least one order of magnitude higher than the measured value on a sintered bulk sample prepared with the same PMS powder.

2.   Discussion

The estimated high intragrain j_c values are not so peculiar if one consider the important reduction of screening currents caused by the presence of grain boundaries in the specimen, as we observe by ac-susceptibility measurements. Our results indicate that like in the high-T_c superconductors improvement of j_c is expected with better connections of the grains.

3.   References

[1]   J. Cors et al, this volume.

[2]   R.W. Rollins, H.Küpfer, W.Gey, J.Appl.Phys. 45, 5393 (1974).

[3]   H. Küpfer et al, Cryogenics 28, 650 (1988).

SINGLE CRYSTAL GROWTH AND CHARACTERIZATION OF HIGH-T$_C$ Bi SYSTEM

M. Suzuki[t], H. Nakano[tt], S. Curt, G. Burri and L. Rinderer

Institut de Physique Expérimentale, Université de Lausanne
CH-1015 Lausanne, Suisse
On leave from Saga University[t], Saga 840, and Nagoya University[tt], Nagoya 464-01, Japan.

Abstract :   The two kinds of Bi-Pb-Sr-Ca-Cu-O single crystals were grown by the flux method. The platinum crucible stuffed with potassium chloride of 30 gram and Bi-Pb-Sr-Ca-Cu-O of 5 gram was heated to 950 °C, and then was slowly cooled to a room temperature. A temperature gradient was found to play an important role in a single crystal growth process. The electrical resistance of the single crystal grown from $Bi_{1.7}Pb_{0.3}Sr_2Ca_2Cu_3O_y$ powder was strongly anisotropic and became zero ohm near 77 K. On the other hand, the one from $Bi_{1.7}Pb_{0.3}Sr_2CaCu_2O_y$ powder increased with decreasing temperature and did not show any superconductivity.

Since the high-T$_C$ (110 K) superconductivity in Bi-Sr-Ca-Cu-O system was found by Maeda et al. [1], many investigations have been carried out in both basic and applied sides using a sintered ceramic Bi-system. The experimental data from a Bi-system single crystal can give us informations more than those of Bi-system ceramic. In spite of this, only several experiments [2] have been carried out by using a high-T$_C$ Bi-system single crystal. This comes from the fact that the single crystal growth method for Bi-system has not been established yet. In this paper, in order to improve the single crystal growth method for the high-T$_C$ Bi-system, a relation between a quality of single crystal and a condition of the single crystal growth was investigated.

Two kind of powder, $Bi_{1.7}Pb_{0.3}Sr_2Ca_2Cu_3O_y$ (hereafter referred to as 2223) and $Bi_{1.7}Pb_{0.3}Sr_2CaCu_2O_y$ (hereafter, referred to as 2212) were prepared by the usual solid reaction method. The 2223 or 2212 powder of 5 gram was put into a platinum crucible together with potassium of 30 gram. Single crystals were grown in the following procedure of thermal treatment in air of 1 atmosphere. The crucible was heated to 950 °C and cooled at a rate of 5 °C/h from 950 °C to 880 °C, at a rate of 2 °C/h from 880 °C to 800 °C, at a rate of 30 °C/h from 800 °C to 500 °C, and at a rate of 100 °C/h from 500 °C to room temperature. The temperature gradient of the crucible at 900 °C was nearly equal to 2 °C/cm. Under no temperature gradient, a single crystal could not be obtained. The single crystal A grown from 2223 powder is an opaque and black layered structure. As shown in the electron microscope photograph of Fig. 1(a), the area of the single crystal A ranges between several square millimeters and several ten square millimeters. As seen in Fig. 1(b), the single crystal is composed of many plates. Another single crystal B grown from the 2212 powder is an opaque and black needle-like structure.

Figure 2 shows the temperature dependence of electrical resistance in the a-b plane of two single crystals measured by the four terminal method. The resistance in each characteristics normalized with the one at 295 K. The resistance of the single crystal A strongly depends on the direction of crystal axis along which a current flows, that is, the temperature dependence of resistance is semiconductor-like in the easy-crack direction and is metal-like in the direction perpendicular to the easy crack direction. In either case, the resistance becomes zero ohm near 77 K.

From the x-ray precession photograph, the lattice constant along c-axis is estimated as 3.08 nm, which is equal to the lattice constant of high-T_C Bi-system with $T_C \approx 80$ K [3]. On the other hand, the one of single crystal B increases with increasing temperature and does not show any superconductivity. In order to improve superconductivity, the thermal treatment of 857 °C for 4 hour in air of 1 atmosphere was applied to the single crystals, A and B. However, the critical temperature of the single crystal A was reduced from 77 K to 65 K and the single crystal B still did not show any superconductivity.
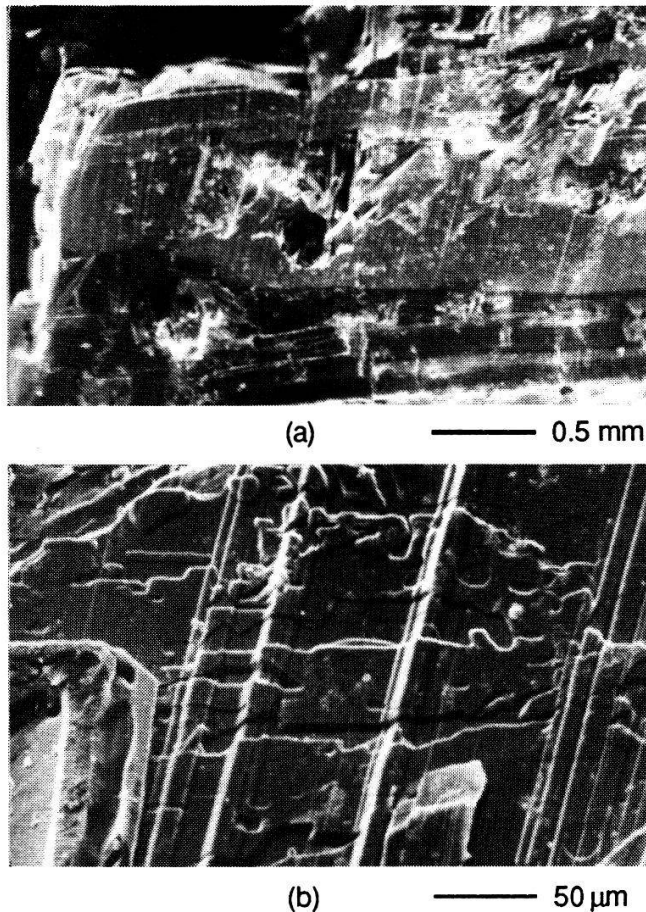

(a) ———— 0.5 mm

(b) ———— 50 μm

Fig.1 Electron microscope photographs of the single crystal A.
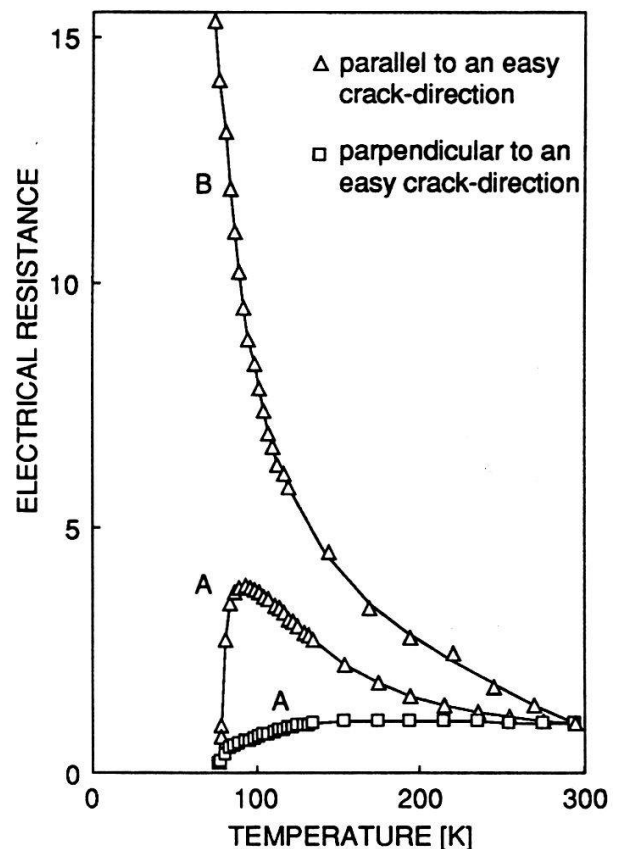
Fig.2 Temperature and direction dependences of electrical resistance for the single crystals, A and B.

References
[1] H. Maeda, Y. Tanaka, M. Fukutomi and T. Asano: Jpn. J. Appl. Phys. 27, L209 (1988).
[2] T. Shishido, D. Sindo, K. Ukei, T. Sasaki, N. Toyota and T. Fukuda: Jpn. J. Appl. Phys. 28, L 791 (1989), L.Pierre, J. Schneck, J. C. Toledano and C. Daguet: Phys. Rev. B41, 766 (1990).
[3] M. Onoda, S. Takekawa, H. Nozaki, A. Umezono and E. Takayama-Muromach: Jpn. J. Appl. Phys. 27, L1665 (1988).

PROPERTIES OF ULTRATHIN YBa$_2$Cu$_3$O$_7$ LAYERS IN YBa$_2$Cu$_3$O$_7$/PrBa$_2$Cu$_3$O$_7$ SUPERLATTICES.

L. Antognazza, J.-M. Triscone, O. Brunner, M.G. Karkut[*], and Ø. Fischer, University of Geneva, DPMC, 24 Quai E.-Ansermet, 1211 Geneva 4, Switzerland.

Abstract: We report on the T_c behavior of YBa$_2$Cu$_3$O$_7$/PrBa$_2$Cu$_3$O$_7$ (YBCO/PrBCO) superlattices with constant, either 12Å or 24Å YBCO layers, and increasing thickness of the PrBCO layers (d-PrBCO). For both series T_c first decreases with increasing d-PrBCO, and for d-PrBCO>60-70Å a plateau at about 50K for the 24Å YBCO series and 10K for the 12Å series is observed.

1. Introduction

The interest of growing YBCO/PrBCO superlattices resides in the fact that PrBCO, while isostructural to YBCO, is not superconducting but insulating. By increasing the insulating separation layer thickness between YBCO layers, the properties of ultrathin YBCO layers become accessible. We recently reported[1] a study of a series of samples with a constant 12Å YBCO layer thickness and various PrBCO thicknesses. Here we briefly present the T_c behavior of a new series with YBCO layer thickness of 24Å (2 unit cells). A more detailed discussion can be found in Ref.2

2. Results and discussion

The samples were prepared on polished MgO substrates by the alternative deposition of YBCO and PrBCO using dc single target planar magnetron sputtering. The preparation details can be found in Ref.3. Fig.1 shows the T_c behavior (measured resistively and defined by the 10% point of the normal state resistance) for the two series of samples: one with constant 24Å YBCO layer thickness and increasingly larger PrBCO thickness (top) and second with

[*]Present Address: Laboratoire de Chimie Minérale B, URA 254 CNRS, Université de Rennes I, 35042, Rennes CEDEX, France.

constant 12Å YBCO layer thickness (bottom). For both series T_c first decreases approximately linearly with increasing d-PrBCO, and then remains about constant. A plateau at ≈50K is clearly observed for the 24Å constant YBCO layers for d-PrBCO>60Å. For the 12Å constant YBCO layers a similar plateau seems to occur for d-PrBCO>70Å with a T_c value around 10K. In Ref.2 we have shown that it is unlikely that these results can be explained by either interdiffusion or proximity effect. Instead, we believe that we are seeing the result of the decoupling of the ultrathin YBCO layers by increasingly larger insulating layers.
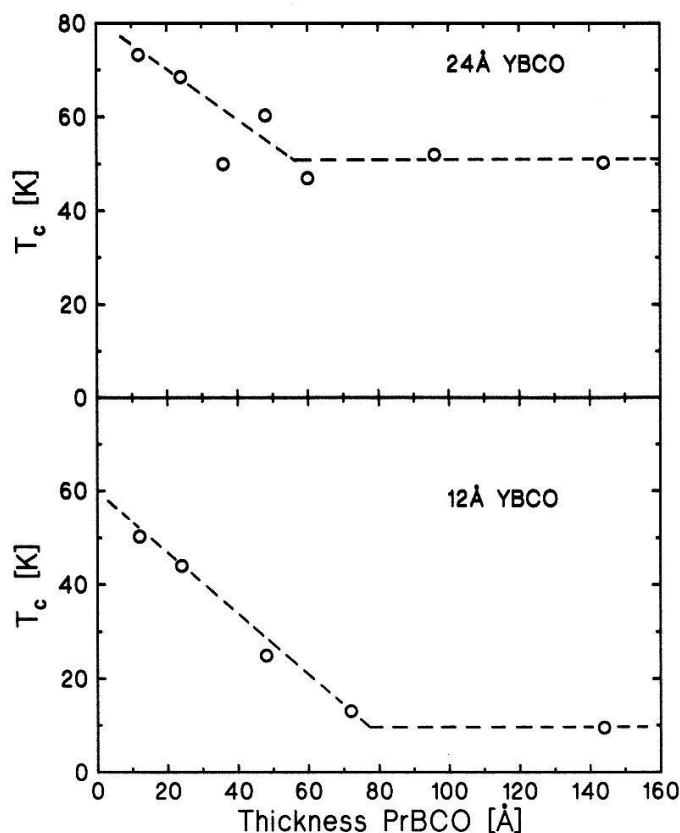

FIGURE 1

T_c as a function of d-PrBCO for, (top) the 24Å YBCO series, and (bottom) the 12Å YBCO series.

3. References

[1] J.-M. Triscone, Ø. Fischer, O. Brunner, L. Antognazza, A.D. Kent, and M.G. Karkut, Phys. Rev. Lett. 64, 804 (1990).

[2] L. Antognazza, J.-M. Triscone, O. Brunner, M.G. Karkut, and Ø. Fischer, submitted to the LT19 conference, Brighton 1990.

[3] J.-M. Triscone, M.G. Karkut, L. Antognazza, O. Brunner, and Ø. Fischer, Phys. Rev. Lett. 63, 1016 (1989), and references therein.

CRITICAL FIELD OF ARTIFICIAL $YBa_2Cu_3O_7$/$PrBa_2Cu_3O_7$ SUPERLATTICES.

O. Brunner, J.-M. Triscone, L. Antognazza, M.G. Karkut[*], and Ø. Fischer, University of Geneva, DPMC, 24 Quai E.-Ansermet, 1211 Geneva 4, Switzerland.

Abstract: We have measured the resistive transitions of $YBa_2Cu_3O_7$/$PrBa_2Cu_3O_7$ (YBCO/PrBCO) superlattices in magnetic fields parallel and perpendicular to the CuO planes. We find in multilayers with constant 24Å YBCO layer thickness that the anisotropy increases dramatically when the insulating separation layer of PrBCO increases from 12Å to 24Å. For larger PrBCO thicknesses the resistive transitions are insensitive to the application of a 90kG parallel field.

1. Introduction

We have recently reported the growth of YBCO/PrBCO superlattices [1] with modulation wavelength as short as 24Å (i.e. a unit cell of YBCO alternates with a unit cell of PrBCO). This multilayer structure is particularly interesting since PrBCO, while isostructural to YBCO, is an insulator. With this system the epitaxial growth of ultrathin (12Å or 24Å, i.e. one or two unit cells) YBCO layers separated by increasingly thicker PrBCO layers, allows us to study the behavior of isolated YBCO ultrathin layers. Here we present briefly upper critical field measurements which reveal the highly two-dimensional behavior of these artificial structures.

2. Results

The samples were prepared on polished MgO substrates by the alternative deposition of YBCO and PrBCO using dc single target planar magnetron sputtering. The preparation details can be found in Ref.2. Fig.1 shows the resistive transitions in parallel and perpendicular fields for a YBCO sample and

[*]Present Address: Laboratoire de Chimie Minérale B, URA 254 CNRS, Université de Rennes I, 35042, Rennes CEDEX, France.

24Å-YBCO/d-PrBCO multilayers. With the field perpendicular to the CuO planes we observe for the multilayers the characteristic broadening of the transition instead of the shift observed in "classical" superconductors. No reduction of the broadening is observed in spite of the decrease of T_C from 90 K to 50 K. In parallel field we observe that when the PrBCO thickness increases from 12Å to 24Å the effect of the field becomes insignificant, a small broadening of the foot of the transition for 24Å/24Å multilayers and no detectable effect on the 24Å/144Å multilayer. These measurements show that our modulated structures are very different from single thin films of YBCO and reveal their highly two-dimensional behavior. A detailed discussion can be found in Ref.3.
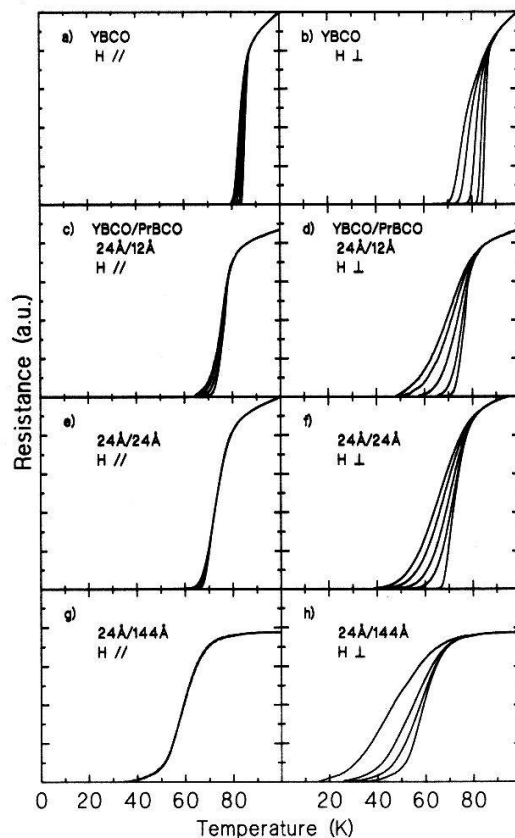

FIGURE 1

Resistive transitions in parallel and perpendicular fields of 0, 10, 30, 60, and 90kG. (The 60kG perpendicular field curve for the 24Å/144Å sample is missing).

3.   References

[1]   J.-M. Triscone, Ø. Fischer, O. Brunner, L. Antognazza, A.D. Kent, and M.G. Karkut, Phys. Rev. Lett. 64, 804 (1990).

[2]   J.-M. Triscone, M.G. Karkut, L. Antognazza, O. Brunner, and Ø. Fischer, Phys. Rev. Lett. 63, 1016 (1989).

[3]   O. Brunner, J.-M. Triscone, L. Antognazza, M.G. Karkut, and Ø. Fischer, submitted to the LT19 Conference, Brighton 1990.

Thermal induced rotation of a levitated permanent magnet above a superconducting disk

by Claudio Palmy, Neu-Technikum Buchs, 9470 Buchs, Switzerland
and Ferdinand Füllemann, Neufeld College, 3000 Bern, Switzerland

Stable levitation of a permanent magnet above a superconducting plate is a well-known effect. If a vertical directed thermal gradient field is present, a cylindrical magnet starts to oscillate along the horizontal axis with increasing amplitude and will finally rotate continuously.

We have placed different, axial magnetised cylindrical rare earth compound permanent magnets (RECOMA), from 5 to 8 mm in diameter and 2 to 5 mm long, on a high T_c superconducting disk as $YBa_2Cu_3O_7$. The magnets are levitated due to the Meissner effect. Since the centre of gravity and the axis of supporting magnetic forces F_M generally do not coincide a mechanical torque is often obtained. Therefore the magnet shows small oscillations around the cylindrical axis to find its equi- librium position. Contrary to what would be expected, the oscillation is not damped, but, will continuously increase in amplitude and in many cases a permanent rotation with frequencies up to 2 s^{-1} is obtained. In order to explain the observed effect we have measured the temperature gradient above the superconducting disk with a thermocouple.
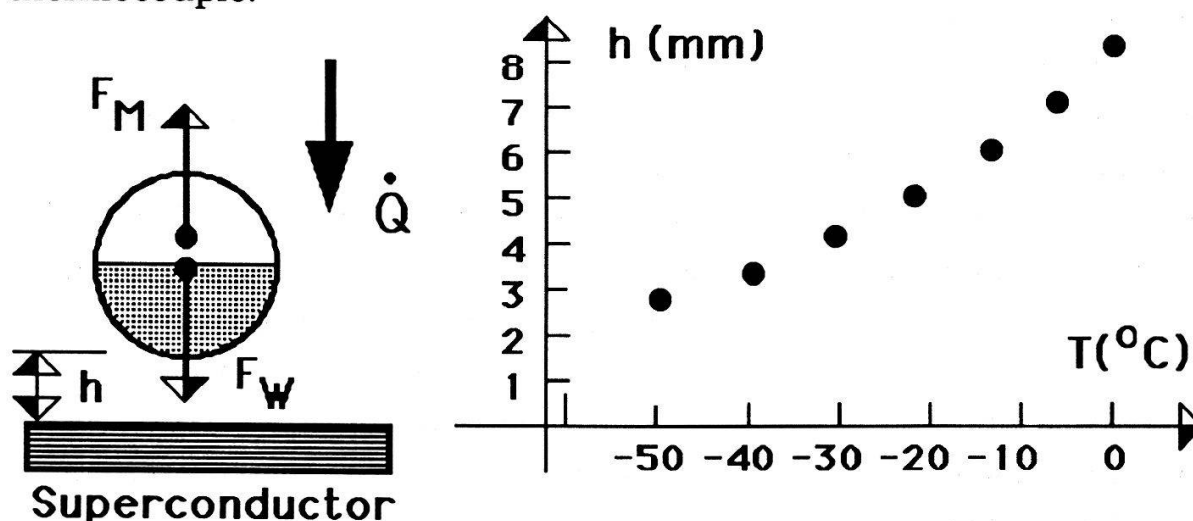

Fig. 1 Cross section of an oxide superconductor below a levitated cylindrical permanent magnet. The vertical temperature gradient causes an asymmetric magnetisation which increases towards the superconducting disk.

We see that the permanent magnet is located inside a temperature field of roughly 10 K/mm. As a consequence of the thermal flux dQ/dt the magnetisation in the upper part of the cylinder will be slightly smaller than in the lower part. Therefore the support point of the magnetic force is moving downward. In general a torque will be built up. According to measurements and Bloch's $T^{3/2}$ law the magnetisation is affected only by about one percent.
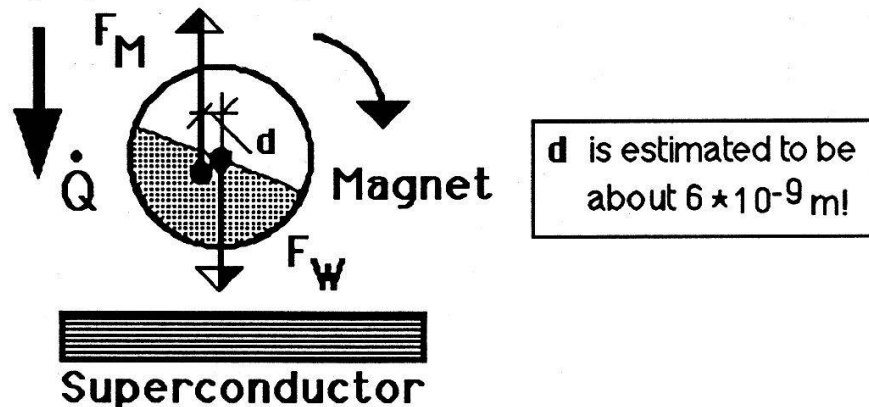

Fig. 2 If the permanent magnet oscillates there is always a "phase lag" between cylindrical motion and the motion of the centre of magnetisation.

By considering a general situation as illustrated in Fig. 2 we realise that the rearrangement of the magnetisation due to thermal flux displays the action point of magnetic levitation forces F_M in such a way that the present magnetic torque is enhanced. As permanent rotation starts the support point of magnetic forces F_M is stabilised on one side of the permanent magnets cylindrical axis and therefore a continuous torque is present. The rotating direction is arbitrary. The rotation effect has universal character in the sense that a thermal gradient always causes rotation of a magnetically levitated permanent magnet.

The described system is able to transform thermal energy to mechanical energy into a fraction of about $1 : 10^{-7}$.

We are grateful to R. Casparis and E. Röthenbacher for helpful discussions as well as F. Schnüriger for the preparation of the superconducting disks.

CHARACTERIZATION OF $Si_{1-x}Ge_x$ FILMS BY INELASTIC LIGHT (BRILLOUIN)SCATTERING FROM SURFACE ACOUSTIC MODES

M. MENDIK, M. OSPELT, H. VON KÄNEL and P. WACHTER

Lab. für Festkörperphysik, ETH–Zürich, 8093 Zürich

<u>Abstract</u>

Surface acoustic waves on cubic $Si_{1-x}Ge_x$ films grown on Si(100) have been measured by Brillouin scattering both as a function of k h and the direction of k. (k:wavevecto of phonon in the layer plane, h: thickness of the film). The velocity of the SAW on sufficiently thick films is not influenced by the substrate. Therefore the angular dispersion can be used to determine the elastic properties of the film using a single–crystal model.

<u>Introduction</u>

The existence of a surface causes interference of shear and compressional bulk waves at the crystal–air interface and is therefore the origin of surface acoustic waves. These thermally excited corrugations are the dominating mechanism for light scattering in opaque media. The presence of a film extends the boundary conditions apart from the usual σ_{3j} (j=1..3)=0 at a stress free crystal surface. These boundary conditions describe the continuity of the particle displacement at the substrate–layer interface. Depending on the layer thickness and the shear velocities of layer and substrate material, higher order modes may exist. It was first demonstrated by Elmiger [1] that it is possible to compute the complete elastic tensor of cubic single crystals using the angular dispersion of SAW. Calculations of the elastic properties of different layer compositions have been treated in [2,3]. Here an alternative approach is used to determine the elastic constants of a single $Si_{0.49}Ge_{0.51}$ film with h=5000Å.

<u>Experimental</u>

We used the λ=514 nm line (TM polarized) of an Ar^+ laser as the excitation source. The backscattered light was analysed by a 3+3 Tandem interferometer [4]. By varying the incident angle θ_i it is possible to change the length of the selected phonon momentum. Rotation of the sample around the sample normal allows to control the direction of the phonon in the sample plane. The measurements were carried out in air and at room temperature. The $Si_{0.49}Ge_{0.51}$ (thickness 80Å and 5000Å) alloys were prepared by co–deposition of Si and Ge on Si(100) while the substrate was held on 460° C. The $Si_{0.66}Ge_{0.34}$ (1170Å, 2400Å) were made by co–deposition of a thin layer at room temperature and annnealing to 500°. This step was repeated until h=1170Å or h=2400Å. Layers grown in this manner exhibit extremely smooth surfaces. The samples were characterized by Rutherford backscattering and channeling [5].
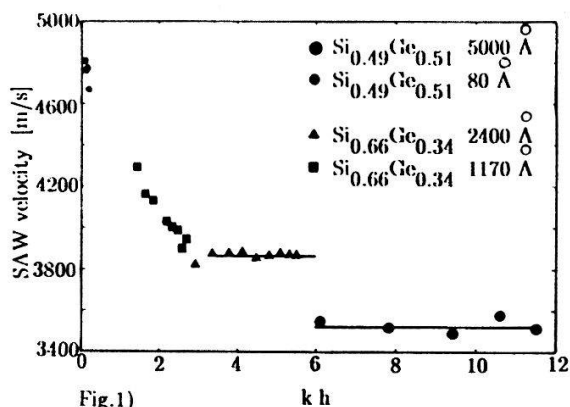

Fig.1)

<u>Measurements</u>

A film grown on a substrate loads or stiffens the surface. If the layer is thinner than the acoustic penetration depth of the SAW, the velocity depends on the elastic properties of the substrate as well as on those of the film. On the other hand if the film is sufficiently thick the SAW is completely determined by the layer material alone and is therefore dispersionless.

In order to determine the relation between the velocity and kh we varied θ_i from 25° to 75°. We observed (Fig.1)a dispersion of the SAW for h=80Å and h=1170Å indicating an influence by the substrate. In contrast, the
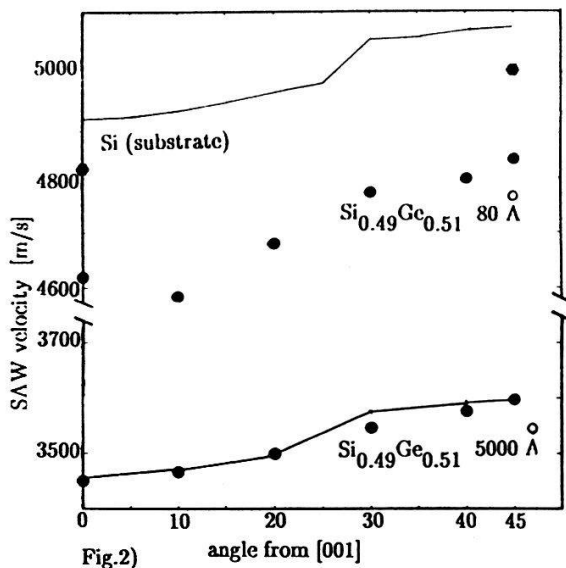
Fig.2)   angle from [001]

SAW velocity remains constant with increasing kh on the thickest films which demonstrates that the SAW are decoupled from the substrate and therefore determined by the elastic tensor of the film only. There were no higher order modes measurable for all samples.

Fig.2) shows the angular dispersion of the SAW on a h=80Å and h=5000Å $Si_{0.49} Ge_{0.51}$ film. The axes indicated on the plot refer to the crystallographic directions of the substrate. Measurements were carried out for various angles in the sample plane while θ_i was fixed at 70°. The angular dispersion of the SAW is strongly influenced by the substrate on the h=80Å film and reflects that symmetry too. In contrast, the angular dispersion on the h=5000Å film originated from the symmetry of the grown alloy alone. (which happens to be cubic as well in our case)

Computations

In order to get the elastic tensor we applied the Levenberg–Marquardt procedure to perform a least square fit of the measured phase velocities on the 5000Å thick film to the model function described in [6]. The elastic constants thus derived:
C_{11}=139GPa (146GPa),C_{44}=66GPa (72.9GPa), C_{12}=59GPa (56GPa)
The density has been kept fixed at ρ=3.8gr/cm³. In brackets are shown for comparison the values obtained by the linear interpolation of ultrasonic measurements on Si and Ge single crystals. It seems possible to compute the elastic constants of the thinner films - (h=80Å,1170Å) but the stiffness tensors of both substrate and layer have to be included in the computations.

Acknowledgements
We wish to gratefully thank M.Elmiger for helpful discussions.

References
[1] M.W. Elmiger, Surface and Interface Analysis, 14, 18 (1989)
[2] J.R. Sandercock in "Light Scattering in solids II", p.173, Springer (1982)
[3] J.M. Karnikas, J. Appl. Phys. 65 (9), 3407, (1989)
[4] F. Nizzoli, Phys. Rev. B, Vol. 37, 2, 1007, (1988)
[5] M. Ospelt, Superlattices and Microstructures, 5, 71 (1989)
[6] G.W. Farnell in "Physical Acoustics", VI, p. 109; Ed.: Mason, Academic Press (1970)

SECOND SOUND AND GRAVITY WAVES IN AN OPEN CYLINDRICAL VESSEL – INTERACTING RESONANCES

P.W. EGOLF, S. DI NARDO, P. CAMINADA
Laboratorium für Festkörperphysik, ETH Hönggerberg, 8093 Zürich

Second sound resonances can be excited in a cylindrical vessel partly filled with liquid helium. Gravity waves in the bulk liquid can form resonances in the same container. The two wave systems interact and may be regarded as existing in two coupled resonators. When single frequency second sound beyond a certain critical intensity is supplied surface gravity waves are formed on the liquid. These have a wide range of frequency far below that of the second sound. The wave systems behaving as coupled oscillators and their quality factors are discussed.

Second sound of resonance frequency f_{2_r} (1000 Hz < f_{2_r} < 20'000 Hz) is introduced into the bulk of Helium II with a free surface contained in a cylindrical vessel. Values of the quality factor Q_2 of this vessel were deduced by Olsen from the widths of the resonance frequencies observed with a Schlieren technical device [1]. They proved to be of the order Q_2 = 300. According to the equation

$$Q_\alpha = \pi \, f_{\alpha_r} \, \tau_\alpha \quad \alpha \in \{1,2\} \qquad (1)$$

we obtain for f_{2_r} = 2308 Hz and a mean fluid temperature T=1.59 K a relaxation time τ_2 = 0.04 s. First crude observations confirm that τ_2 is less than 0.25 s.

Second sound of low intensity generates a stationary surface relief whose variation of the height η depends linearly on the square of the total energy input P into the axial second sound generator. Below a critical input P_c the surface is completely immobile. Above P_c an instability occurs [2] and gravity waves begin to develop.

The same cylindrical vessel also acts as a resonator for gravity waves. A new photometric detecting system for these surface waves has recently been described [2]. With this the relaxation times τ_1 of the gravity waves have been measured. An example is shown in fig. 1. Here $\tau_1 = 3.0$ s with a corresponding basic frequency $f_{1_r} = 11$ Hz (fig. 2) is found. From equation (1) we calculate $Q_1 = 104$.
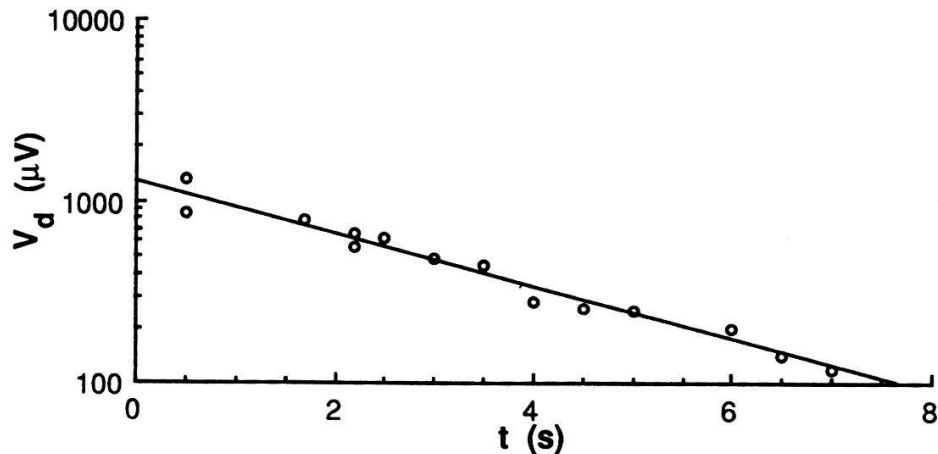
Fig. 1 - Output voltage of a photodiode $V_d \propto \eta$ as a function of time. Wave number $k = 702$ m^{-1}. Temperature T = 1.59 K
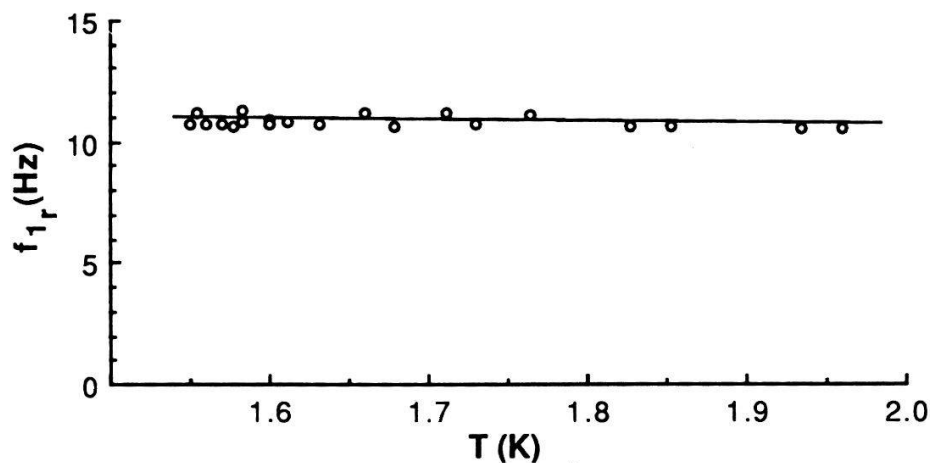
Fig. 2 - Basic resonance frequency f_{1_r} of gravity waves excited by second sound

In the resonant cavity Q_1 up to forty superharmonic frequencies with basic frequency f_{1_r} can be excited resulting in an irregular motion of the liquid surface.

[1] Olsen J.L., J. Low Temp. Phys. 61, 17 (1985)

[2] Egolf P.W. and Weiss D.A., Helv. Phys. Acta 63/4, 475 (1990)

DC size effects in Al : surface structure by XPS and SEM

J. Romero [1], M. Schmidt [2], S. Steinemann [2] and R. Huguenin [2]

[1] Present address : World Radiation Center / PMOD, CH-7260 Davos-Dorf
[2] Institut de Physique Expérimentale, Université de Lausanne, BSP CH-1015 Lausanne

Abstract : *In the case of size effects in the dc electrical resistivity $\rho(d,T)$ the bulk mean free path is of the order of the sample thickness d and the conduction electrons undergo multiple scattering at the sample surface. In this work we present X-ray photoelectron spectroscopy (XPS) and scanning electron microscopy (SEM) analyses of Aluminium samples in which $\rho(d,T)$ shows a strong dependence on the state (polished or rough) of the surface. In both cases the oxyde layer has a typical thickness of 80 Å. The oxide impurities detected by XPS depend on the chemical treatment used to modify the surface structure. The resistivity $\rho(d,T)$ was found to be strongly correlated with the surface condition whereas oxide ha no influence on it.*

Traditionnally, works on dc size effects in the electrical resistivity $\rho(d,T)$ on Al assumed that the surface, being oxidized immediately after production, scatters the conduction electrons diffusely (see e.g. [1]). This was attributed to the oxide layer supposed to have the same influence whatever treatment is used to prepare the surface. Notwithstanding, previous results [2] showed that $\rho(d,T)$ is influenced by the surface preparation and its behaviour could be interpreted in terms of size effects theories on dc resistivity including a specularity parameter p with values different from 0, i.e. with a fraction of the incident electrons specularly scattered at the surface. These theories have three parameters : ρ_∞, λ_∞ respectively the bulk resistivity and mean free path and the specularity p. In more refined theories p is function of the angle of incidence θ of the electron on the surface and of a roughness parameter $r = d/\lambda_e$ (λ_e being the electron wavelength) : $p(\theta) = exp(-(4\pi r)^2 \cos^2 \theta)$ [3]. For the determination of these three quantities, one measurement is not enough and sometimes artefacts and asymptotic results are employed. In order to analyze correctly the experimental data, Sambles [4] pointed out the necessity to carry out a structural analysis of the sample and particularly of its surface. This can help to attribute a reasonable value to the specularity parameter p. The aim of this work is to correlate structural analysis of the surface with results on the specularity deduced from resistivity measurements.

Two sets of samples were prepared with the same surface treatment as those whose electrical resistivity $\rho(d,T)$ was measured. One set was analyzed by XPS (Leybold EA10/100), the other by SEM (Cambridge Stereoscan 150) and pictures with magnifications up to 10000 of the sample surface were taken. Table 1 shows the surface preparation method and characteristics of each sample. The value of the roughness parameter r indicating the polished or diffuse (rough) state of the surface deduced from measurements of $\rho(d,T)$ is also given. Excepting R5 the samples were not annealed. After production by cold rolling from material of 5N purity, which took place ten years ago, samples R1, R3, R4 and R6 have been conserved with no particular precautions at room temperature exposed to air. Their structure is of course polycrystalline. Sample R5 was monocrystalline 6N purity and was annealed at 470°C . It is taken from the same matrix as Al3 of reference [2] where more details on surface treatments can be found.

As shown in Table 1, the "initial" state of the surface (R3) resulting from the preparation by cold rolling is polished. XPS analysis shows the oxidized surface state for all samples; the chemical shift of Al2p signals indicate Al_2O_3. The oxide layer thickness is estimated by comparing the Al2p(oxide)-overlayer signal with the Al2p(metal)-substrate signal, assuming the oxide as homogeneous Al_2O_3 and the surface being smooth. This limits the precision of the estimate of the layer thickness given in Table 1. XPS analysis also indicates the presence of contaminants which are characteristic for the surface preparation method (cf. Table 1). From angle resolved studies on rather smooth samples it can be concluded that the impurities are inbedded in the oxide film.

SEM images show the rough character of etched sample surface with pores of 20 μm whereas electropolished samples have a smooth surface on which no details can be distinguished on the scale of 1 μm. Figure 1 show typical results of resistivity measurements in samples with polished and etched surface. For a given

temperature and thickness, the roughness parameter r and the resistivity decrease in a sample whose surface is polished with one of the treatments indicated in Table 1, while both quantities increase in a sample with an etched surface.

Sample	Treatment	Layer (Å)	Impurities	r
R1	p, H_3PO_4, 20°C	70	PO_x, NO_x	0.30
R2	p, electropolished	>80	NO_x	0.30
R3	Initial (p)	60	C (surface)	0.30
R4	e, NaOH, 2g/l, 20°C	>80	Na	0.40
R5	e, NaOH, 2g/l, 65°C	40	Na	0.40
R6	e, $FeCl_3$, 65°C	>80	$FeCl_x$	3.0

Table 1. Results from XPS analysis and resistivity measurements. The polished (p) or etched (e) states of the surface are obtained with the treatments indicated. The thickness of the oxide layer is also given. The column "Impurities" gives the major impurities present in the oxide layer; the most probable values of x are in R1 4 for PO and 2 for NO, in R2 3 for NO, and in R6 3 for FeCl. The roughness parameter r of Soffer's theory is deduced from resistivity measurements [2].
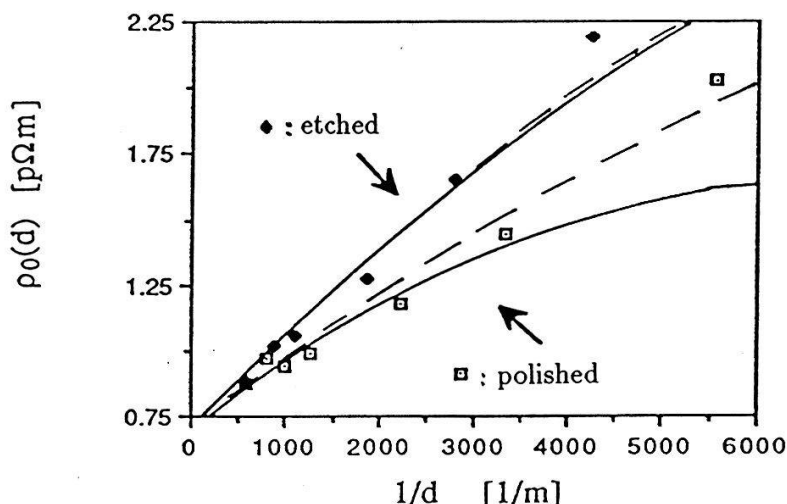

Figure 1. Residual resistivity $\rho_0(d)$ as a function of the inverse thickness $1/d$ for a sample whose surface has been alternatively electropolished and etched with $FeCl_3$. The curves are calculated with $\rho_\infty = 0.70 p\Omega m$ and $\lambda_\infty = 1050 \mu m$ with Soffer's theory (solid curve) yielding $r = 0.30$ (polished) and $r = 3.0$ (etched) and with Fuchs' theory (dashed curve) yielding $p = 0.24$ (polished) and $p = 0$ (etched).

The main conclusion which can be drawn from these surface analyses confronted with results on resistivity is that the specularity and hence the resistivity in thin Al samples is strongly dependent on geometrical roughness and is not much influenced by the oxide layer. The impurities present in this layer do not influence $\rho(d, T)$. The same behaviour is observed in polycrystals and monocrystals and for sample purity from 4N to 6N.

References

[1] Nakamichi I. and Kino T., 1988 J. Phys. F : Met. Phys. 18 2421
[2] Romero J. and Huguenin R., 1989 Helv. Phys. Acta 62 758
[3] Soffer S., 1967 J. Appl. Phys. 38 1710
[4] Sambles J.R. and Elsom K.C., 1985 J. Phys. F : Metal Phys. 15 161
[5] Fuchs K., 1938 Proc. Camb. Phil. Soc. 34 100

FABRICATION AND CHARACTERIZATION OF A Nd^{3+} DOPED MONOMODE FIBER LASER

J. Morel, D. Rosenfeld, F. Maystre, Institut de Microtechnique, Université de Neuchâtel, Breguet 2, CH-2000 NEUCHATEL, Switzerland

Abstract: In this contribution, we report the fabrication and characterization of a 1.09 µm Nd^{3+} fiber laser, pumped with a standard laser diode, at a wavelength of λ_p = 810 nm. The spectral characteristics of the fiber (absorption spectrum, fluorescence), and the characteristics of the laser (slope efficiency, threshold, emission spectrum) are presented.

The structure of the fiber laser [1] is shown in Fig. 1. The laser cavity is composed of a single-mode fiber, with two mirrors at both extremities. The reflectivities of these mirrors ($R_{M1} >$ 99%, $R_{M2} >$ 90%) are chosen to obtain a high finesse Fabry-Perot resonator at the lasing wavelength λ_l. The input mirror transmits all the pump power, and the output mirror reflects all the pump power. The active medium is obtained by introducing Nd^{3+} ions (500 ppm) into the SiO$_2$-GeO$_2$ fiber core, during the fabrication of the preform.

pump
(laser diode, λ_p= 810 nm)   doped fiber (length L = 3.15 m)

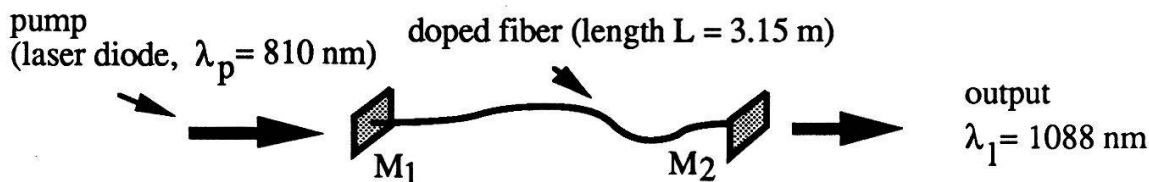output
λ_1= 1088 nm

M$_1$ M$_2$

Fig. 1 Fiber laser.

Two different optical transitions are present in this material. The first one, between the 4F$_{3/2}$ and the 4I$_{11/2}$ energy levels, gives a four level system, with an emission at a wavelength of 1088 nm; the second transition between the 4F$_{3/2}$ and the 4I$_{9/2}$ energy levels involves a three level system, with an emission at a wavelength of 938 nm. The optical fiber has been optimized to be monomode at wavelengths $\lambda \geq$ 950 nm. So, only the 4F$_{3/2} \Rightarrow$ 4I$_{9/2}$ transition can be chosen to obtain a monomode emission. The inversion of the electronic population in Nd^{3+} is achieved by optically pumping with a laser diode at the wavelength corresponding to the maximum absorption of the active medium. The absorption spectrum of the fiber has been obtained by measuring the attenuation as a function of the pumping wavelength, and is shown in Fig. 2 (left). The optimal wavelength for the pumping with a laser diode is of λ_p = 808 nm.

The fluorescence spectrum of a 3.15 m long fiber pumped at λ_p has been measured, as shown in Fig. 2 (right), where the contribution of the two transitions is evident.
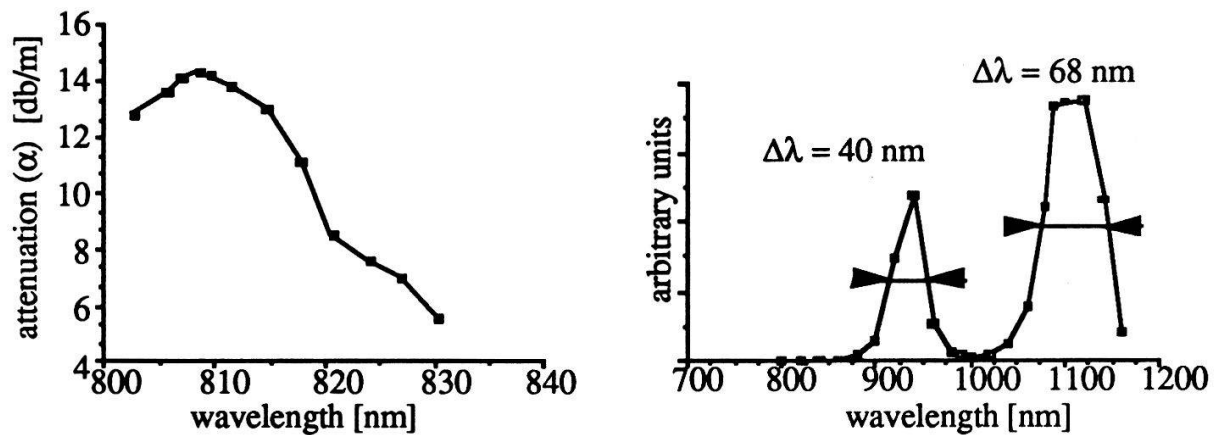

Fig. 2 (Left) : Attenuation spectrum of the fiber. The maximum absorption is obtained at $\lambda=808$ nm. (Right): Fluorescence spectrum; the transitions at 1088 nm and 938 nm are present.

The power and spectral characteristics of the fiber laser pumped with a 40 mW laser diode at $\lambda=810$ nm are shown in Fig. 3 (left) and (right). The threshold is at 0.75 mW. Slope efficiencies between 17 % and 23 % have been measured, depending on the optimization of the resonator. The structures present in the spectrum are given by the mirrors M_1 and M_2. These two mirrors have different thickness ($d_{M1}= 170$ μm, $d_{M2} = 1$ mm), and act as Fabry-Perot etalons. The longitudinal modes of the laser cavity ($\Delta v \cong 32$ MHz) are not resolved in this measurement.
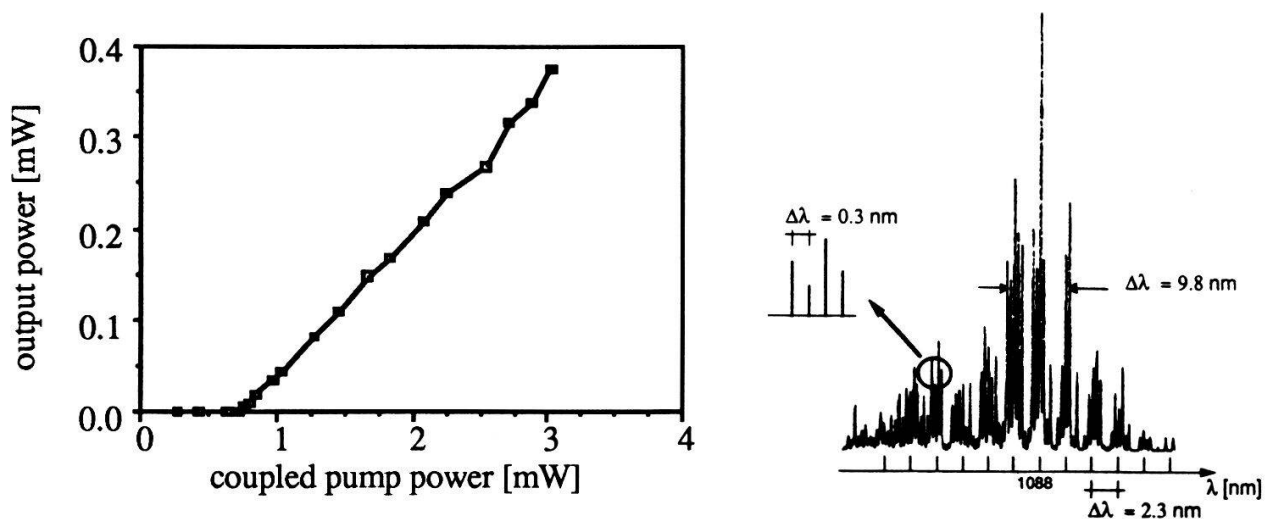

Fig. 3 (Left): Power characteristics of the fiber laser. (Right): Emission spectrum of the fiber laser; spectral selectivity [2] induced by mirrors M_1 and M_2 can be observed.

References

[1]   R. J. Mears et al., Electron. Lett. 25, 738-740 (1985)
[2]   M. Zürn et al., Opt. Lett., 5, 316-318 (1987).

RECURSIVE SYMBOLIC ENCODING AND HIERARCHICAL DESCRIPTION OF CHAOTIC SIGNALS

G. Broggi, Physik Institut der Universität, CH-8057 ZÜRICH-IRCHEL
R. Badii and M. Finardi, PSI-LUS, CH-5232 VILLIGEN PSI

Abstract: We perform a recursive encoding of chaotic signals and organise hierarchically the symbolic sequences in the general case of infinite grammars, thus reducing progressively the complexity of the description. The method provides rapidly converging estimates of the system's asymptotic scaling behaviour and allows for the construction of models based on Markov transition matrices.

1   Unfolding complexity and hierarchical modelling

Nonlinear dynamical systems produce complex temporal or spatial patterns by stretching and folding regions of phase-space in an iterative way. The topological and metric properties of this process can be described hierarchically by using symbolic dynamics, that is by introducing a mapping from the continuous trajectories to sequences of symbols which label the elements of a generating partition[1]. The problem is then reduced to the study of a one-dimensional (stationary) discrete signal which can be divided in subsequences S (of variable length, in general), corresponding to finite regions of phase-space. Hence, each sequence can be associated with its occurrence probability. The description of the dynamics consists of the hierarchical tree of all allowed transitions; a sequence of Markov models follows by constructing the transition matrix for each level of the tree, where the conditional probabilities are evaluated taking into account all memory effects[2]. The choice of the primitive sequences (codewords) on which the analysis is based is directed to obtaining the simplest possible description, i.e., to the minimisation of the number of transition (grammatical) rules. To the same end, one can procede recursively, defining codewords to be new symbols and grouping them to form new codewords; this allows to evidence low-order regularities at increasingly coarse levels of resolution in the time evolution. The iteration of this procedure is equivalent to an automatic renormalisation of the signal and corresponds to a progressive refinement of phase-space. An efficient method for the detection of relevant words is based on the definition of primitives as periodically extendable sequences which do not contain a prefix (initial subsequence) having the same property[2]. Predictions about the structure of the system (expected probabilities $P_0(S)$ of all sequences at level l) for increasing resolution ($l \to \infty$) are

made and compared with the observation (actual probabilities $P(S)$). The discrepancy between the two, evaluated through the information gain

$$C_1 = \lim_{l \to \infty} \sum P(S) \ln \frac{P(S)}{P_0(S)} , \qquad (1)$$

characterises the (metric) complexity of the description. This quantity is related to generalised scaling functions and can be progressively reduced by using improved inference schemes (at the expense of increased space-time extension of the unfolding program). Analogous measures of complexity can be introduced to characterise the scaling behaviour of various observables such as the number of allowed sequences (topological complexity C_0) or the effective Lyapunov exponents. Because of the relationship with the scaling functions[3], these measures yield vanishing values whenever "regular" (i.e., predictable) scaling asymptotically sets in and updated estimates are made. In such cases rapid convergence of invariant measures, dimensions, entropies and Lyapunov exponents can be achieved. Since the dynamics is interpreted as a succession of deterministic paths (primitive blocks of symbols), which appear at random in time with measurable transition probabilities, it is possible to construct global models of the system's evolution, possibly complemented by a fully nonlinear (analytical) treatment. Finally, the invariant features (under smooth coordinated changes) of power spectra are identified in terms of the levels of the tree and of the allowed transitions.

2   Applications

The method has been applied to systems at the transition to chaos (period-doubling and quasiperiodicity), where the recoding is equivalent to the renormalisation group treatment, and to generic maps and flows as the Lorenz system[4]. We plan to extend this approach to the analysis of embedded experimental signals and to patterns generated by parallel algorithms (such as cellular automata).

3   References

[1] J.P. Eckmann and D. Ruelle, Rev.Mod.Phys. **57**, 617 (1985).

[2] R. Badii, *"Unfolding Complexity in Nonlinear Dynamical Systems"*, in *"Measures of Complexity and Chaos"*, N.B. Abraham, A. Albano, T. Passamante and P. Rapp Eds., Plenum, New York, (1990).

[3] M.J. Feigenbaum, J.Stat.Phys. **52**, 527 (1988).

[4] G. Broggi, R. Badii and M. Finardi, *"Hierarchical Approach to Modelling of Nonlinear Flows: Application to Lorenz-like Systems"*, this issue.

HIERARCHICAL APPROACH TO MODELLING OF NONLINEAR FLOWS: APPLICATION TO LORENZ-LIKE SYSTEMS

G. Broggi, Physik Institut der Universität, CH-8057 ZÜRICH-IRCHEL
R. Badii and M. Finardi, PSI-LUS, CH-5232 VILLIGEN PSI

Abstract: We investigate Lorenz-like systems by locating all unstable periodic orbits (up to a given order) for different parameter values, and by using them for the approximation of a generating partition. The symbolic dynamics thereby extracted is organised hierarchically on a logic tree. This procedure suggests how to construct piecewise linear models which can be improved by suitable nonlinear perturbations and allows for improved estimates of the system's asymptotic scaling behaviour.

1   Introduction

We apply the procedure described in Ref. ([1]) to the analysis of the Lorenz and the Rössler differential flows [2]. The former system has been chosen for its relevance as a model of several physical phenomena (convective motion in fluids and lasing behaviour in nonlinear optical media); the latter, for the absence of simplifying symmetries. Both flows admit a 2-dimensional Poincaré map. The topological invariants (unstable periodic orbits) are first extracted numerically by means of a hybrid Newton method. Since the lengths of periodic orbits in a continuous-time system are, in general, different from one another and unknown, it is then necessary to discretise time into successive returns of the trajectory onto a suitably chosen Poincaré surface. In this way, all "period-n" orbits are assigned the same topological return time (n intersections): successively, they are labelled with integers, so that their neighbourhoods constitute a coarse-graining of phase-space. Longer cycles are then classified according to the domains they intersect. Hence, the original continuous dynamics is represented by a subshift on a symbolic sequence $S = s_1 s_2 \ldots$. The probabilities $P(S_n)$ of all subsequences S_n of S, for $n \in [1, n_{max}]$ are then estimated and the system's symbolic dynamics is described by allocating the relevant sequences on a logic tree [1].

2   Application to Lorenz and Rössler Systems

We have studied the Lorenz equations at standard parameter values ($\sigma = 10, b = 8/3, r = 28$) and at ($\sigma = 10, b = 1, r = 28$), and the Rössler system at ($a = 0.2, b = 0.2, c = 5.7$). The first example is topologically simple: a complete binary tree is found up to very large sequence lengths. In the second case, the dynamics is described by an infinite ternary
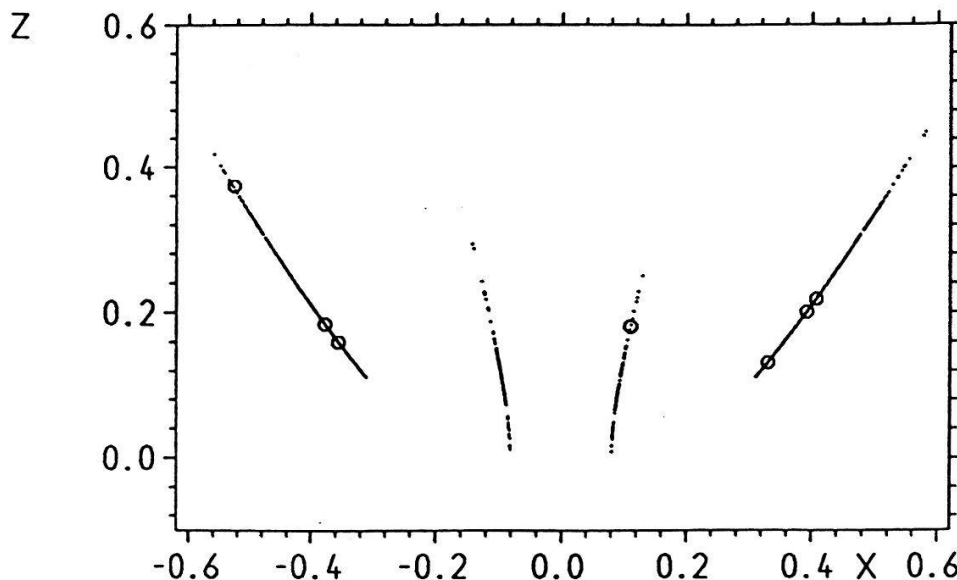
grammar, whereas Rössler's attractor is topologically equivalent to the logistic equation (just after the crisis of period-3) up to high-order cycles. This phenomenology covers a significant spectrum of possible dynamical behaviours of low-dimensional systems. The Poincaré sections have been chosen as follows: for the Rössler attractor, the $y - z$ coordinate plane, which is seen by inspection to intersect all trajectories; for the Lorenz system, the plane $\dot{x} = \sigma(y - x) = 0$, which contains the three fixed points and is also crossed by all trajectories. In the latter case, intersections are to be considered only for those orbits that cross the Poincaré surface in the direction $(1, -1, 0)$ for $x > 0$ and $(-1, 1, 0)$ for $x < 0$. In this way the symmetry properties of the flow and of the Poincaré map are the same and, above all, no relevant intersection are neglected (at variance with maps previously considered in the literature). In all cases we extracted Poincaré returns up to order 9. In the figure, the intersections of a period 7-orbit of the Lorenz system at $b = 1$ with the chosen Poincaré plane are shown as small circles superimposed on the map's strange attractor. Although the presence of four regions suggests that a four-element partition is needed to encode all orbits, three symbols suffice, because of the existence of obliged transitions (as suggested by the symmetry of the system). Accordingly, the topological entropy has been evaluated with high precision. The knowledge of the logic tree can be used to construct a (2-parameter) piecewise linear map which approximates the "topological dynamics" on the Poincaré section, while the metric properties can be more accurately reproduced by introducing suitable nonlinear perturbations. In this way, a complete characterisation of the system is obtained. We plan to extend the method to the much more challenging task of the characterisation of experimental signals.

3   References

[1] G. Broggi, R. Badii and M. Finardi, *"Recursive Symbolic Encoding and Hierarchical Description of Chaotic Signals"*, this issue.

[2] E.N. Lorenz, J.Atmos.Sci. **20**, 130 (1963); O.E. Rössler, Phys.Lett. **57A**, 397 (1976).

Escaping from an attractor close to a Hopf bifurcation

R. Holzner, A.W. McCord

Physik Institut der Universität Zürich

The NMR-laser with a small phase locked injected signal is modelled by a simple 2-dimensional nonlinear differential equation system [1] describing the time evolution of the dimensionless transverse (v) and longitudional (z) components of the nuclear magnetization

$$\frac{dv}{dt} = -vz + bz - \gamma v$$
$$\frac{dz}{dt} = v^2 - bz - z - \mu$$

For constant values of the phase locked signal amplitude (b) and the transverse magnetization decay rate (γ) at the critical value for the pump magnetization $\mu_k = -(1 + \gamma)(\gamma b^2 + 1)$ a subcritical Hopf bifurcation occurs at the phase space point

$$v_k = b(1 + \gamma)$$
$$z_k = -(1 + \gamma)$$

This leads to unstable periodic solutions around a branch of stable fixed points parametrized by μ.

All solutions originating from within the periodic orbit (basin of attraction) decay towards the stable fixed point, whereas solutions originating from outside the periodic orbit spiral outward and eventually cross the z axis to find a stable fixed point in the negative v half plane.

Interesting dynamic behavior occurs when one of the parameters is modulated, e.g. $\gamma = \gamma_0(1 + \alpha \cos(\omega t))$. Areas of attraction and areas of repulsion can form astonishing patterns (Fig. 1). We explore their topological structure by calculating "escape time" plots which indicate, for systematically varied initial conditions (v,z), the time needed by the solution to reach the "escape line" v=0. At present we are performing such calculations on Cray and Alliant computers in order to find fractal attractor structures (where escape times go to infinity) for various values of the modulation amplitude α and the modulation frequency ω.
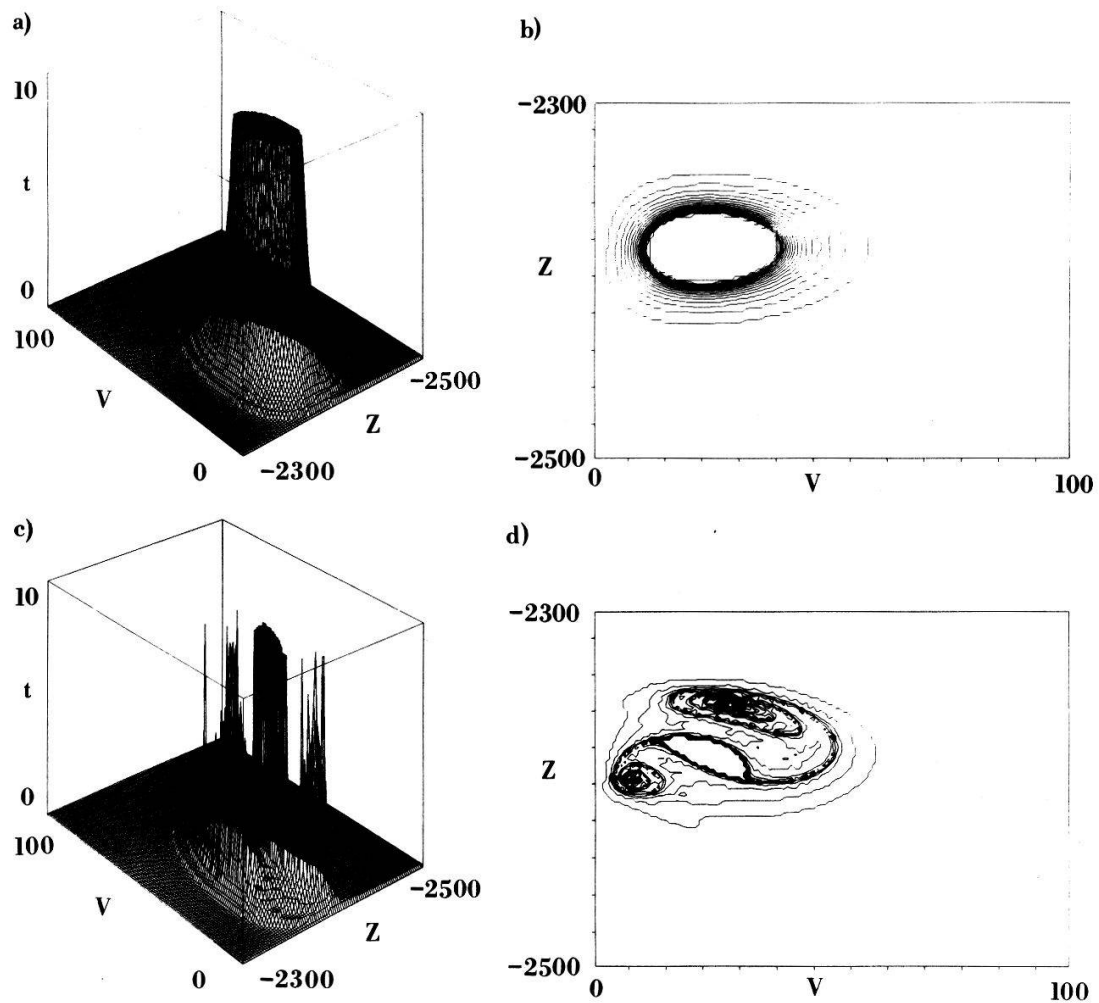
Figure 1: (a) "Escape time" plot for no modulation (b) "Escape time" contour plot for no modulation (c) "Escape time" plot for $\alpha = 0.002$, $\omega = 60$ (d) "Escape time" contour plot for $\alpha = 0.002$, $\omega = 60$. Escape times are only calculated up to 10 dimensionless units which correspond to one second. The spacing between contour lines is 0.5 dimensionless time units.

References

[1] R. Holzner, B. Derighetti, E. Brun, and M. Ravani. Observation of a subcritical Hopf bifurcation in a laser with injected signal. *Physical Review A*, 36(3):1280–1287, 1987.

Comparison of Three Different Numerical Methods
to Characterize the Geometry of Dendritic Structures

B.Merté[b], J.Müller, R.Rückerl, P.Hildebrand, † E.Lüscher

Physik-Department E 13 der Technischen Universität München, D - 8046 Garching

Abstract: Dendritic structures are ramified, simply connected and scale invariant over a certain range. Thus, the characterization of their geometry by a fractal dimension as a global quantity is possible. In the following three numerical methods for the evaluation of a fractal dimension that is approximately equal to the Hausdorff-Besikovitch dimension D_{HB} are presented and compared.

Laplacian and related growth phenomena lead to dendritic patterns that seem to play a crucial role in nature. There exists a multitude of experiments to produce dendrites in order to study their growth dynamics as well as their properties as a function of specific experimental conditions ([1], [2], [3]). The first step in this study is always a merely geometrical classification concerning the scaling behaviour of the mass distribution.

The Hausdorff-Besikovitch Dimension D_{HB} ([4], [2])

In order to measure the size of a set of points S in D_E-dimensional space one takes a test function $h(l) = \gamma l^d$ and covers this set to form the measure $M_d = \sum_S h(l)$. Here l is the "size" and d the dimension of the "boxes" which build up the coverage, wheras γ can be considered as a constant factor. A simplified[1] Hausdorff-Besikovitch dimension D_{HB} of the set S then is the critical dimension, where the measure changes from ∞ to 0. Only for $d = D_{HB}$ M_d does take a finite value W in the limit $l \to 0$:

$$M_d = \sum_S \gamma l^d = \gamma N(l) l^d \to_{l \to 0} \begin{cases} 0 & for \quad d > D_{HB} \\ W & for \quad d = D_{HB} \\ \infty & for \quad d < D_{HB} \end{cases} \tag{1}$$

$$D_{HB} = -\lim_{l \to 0} \frac{ln[N(l)]}{ln[l]} \tag{2}$$

The Boxcounting Dimension D_{BC}

For real systems it is impossible to take the mathematical limit $l \to 0$. Assuming that (2) holds for small l, one can plot $ln[N(l)]$ versus $ln[l]$ and thus evaluate the slope being the negative boxcounting dimension D_{BC}. From the above it is clear that for selfsimilar or scale invariant structures $D_{BC} \approx D_{HB}$ holds.

The Cluster Dimension D_{CL}

For a selfsimilar fractal composed of particles of finite size L_0 it is thus possible to define a cluster dimension D_{CL} by the scaling behaviour $N(L) \sim \frac{L}{L_0}^{D_{CL}}$, where $\frac{L}{L_0} \gg 1$. Again taking the logarithm, one finally finds that:

$$D_{CL} = \lim_{L \to \infty} \frac{ln[N(L)]}{ln[L]}. \tag{3}$$

The limit $L \to \infty$ means in practice taking a very large cluster. The numerical evaluation of D_{CL} is done by defining a center on the cluster and then counting the number of particles belonging to the cluster within successively growing distances from this center. In the limit $N \to \infty$ $D_{CL} \approx D_{HB}$ should hold.

[b]: Part of Ph.D.thesis

---

[1]in general one takes the infimum of covering "boxes" of different sizes

The Density-Density-Paircorrelation Function $c(r)$

The density-density-paircorrelation function is defines as

$$c(r) = \frac{1}{N} \sum_{r'} \rho(r + r')\rho(r'), \tag{4}$$

which is the expectation value that two particles separated by r belong to the structure. Here ρ is either 1 if there is a particle, or 0 if there is none. For ordinary (selfsimilar or scale invariant) fractals $c(r)$ should scale as $c(r) \sim r^{-\alpha}$. By comparing the scaling behaviour of the particle number with distance L for an ordinary selfsimilar cluster, one gets

$$N(L) \sim \int_0^L c(r)d^{D_E}r \sim L^{D_E - \alpha} = L^{D_{DC}} \approx L^{D_{HB}}. \tag{5}$$

From a plot of $ln[c(r)]$ versus $ln[r]$ one gets $-\alpha$ by fitting the slope, and then - for the planar case ($D_E = 2$) - $D_{DC} = 2 - \alpha$. In practice, one can calculate the $c(r)$ function starting from different points of the cluster and then taking the average, where the more peripheric points should be omitted.

Comparison of the Three Numerical Methods

- Method I, leading to D_{BC}, is the most general one, it is relatively fast, but not very sensitive; often it mimics fractal scaling behaviour, even if there is none (see fig.1)

- Method II, leading to D_{CL}, is best applicable to clusters grown around a well defined center; it shows clearly the range of scales, where fractal scaling seems to take place, but it is oversensitive to the chosen range of the fit (see fig.2)

- Method III, leading to D_{DC}, is - from a conceptual point of view - the most easily understandable one; but it efforts very much computation time and it is very hard to find out, which particles should be taken as centers and which range of r values should be chosen (see fig.3)
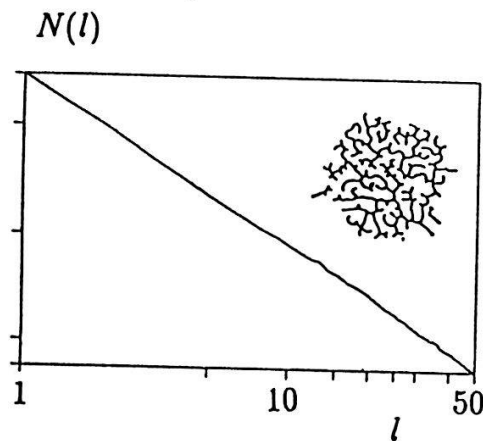

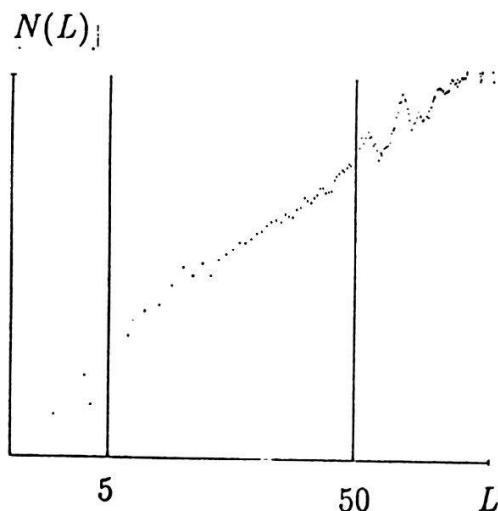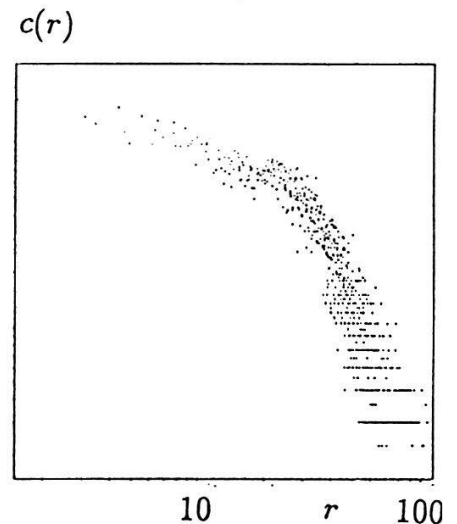Fig.1: $D_{BC} = 1.60 \pm 0.017$ Fig.2: $D_{CL} = 1.6 \pm 0.11$ Fig.3: $D_{DC} = 1.5 \pm 0.10$

[1] Vicsek, T.: Fractal Growth Phenomena, World Scientific, Singapore 1989

[2] Feder, J.: Fractals, Academic Press, New York 1988

[3] Merté, B.: Wachstum und Eigenschaften dendritischer Strukturen, Phys.Bl. 46 (1990) 21-22

[4] Mandelbrot, B.: The Fractal Geometry of Nature, Freeman, New York 1983

IMPROVEMENTS OF PROGRAMS TO RECONSTRUCT DIFFERENTIAL EQUATIONS FROM EXPERIMENTAL DATA

P. Pöschl, M. Athelogou[*], [†] E. Lüscher
Physic Dept. E13, Technical University Munich, D-8046 Garching

Abstract: We present improved FORTRAN-programs to reconstruct a differential equation (DEQ) from a measured time series. Following A. Hübler [4] we used a polynomial ansatz

$$\dot{y}(\vec{x}) = \sum_{|\vec{i}|=0}^{M} c_{\vec{i}} * x_1^{i_1} * \cdots * x_N^{i_N} \tag{1}$$

The coeffizients $c_{\vec{i}}$ are calculated with the method of least squares.
Existing programs have been improved
1. to fit DEQ-systems of arbitrary dimensions
2. to ease elimination of coefficients which contribute only very little to the fit.

1. INTRODUCTION

Simple systems of explicit DEQ's $\dot{\vec{x}} = \vec{F}(\vec{x})$ can be reconstructed from experimental data [4,5]. With estimates $\dot{\vec{x}}_n, n = 1, \ldots, N_{dat}$, for tangential vectors and a polynomial ansatz

$$F_j = \sum_{|i|=0}^{N_{deg}} c'_{\vec{i},j} \prod_{k=1}^{N_{dim}} L_j(z_{n,k}, i_k) \qquad j = 1 \ldots N_{dim} \tag{2}$$

coefficients $c'_{\vec{i},j}$ can be calculated by a least squares method. $L(z_n, i)$ are Legendre–Polynomials of order i and $z_{n,k} = a_k x_{n,k} + b_k$ with a_k, b_k so, that $-1 < z_{n,k} < 1$ for all n. After the fit the Legendre-Coefficients $c'_{\vec{i},j}$ are converted to coefficients $c_{\vec{i},j}$ of eqn. (1).

We present a method to fit a DEQ even if only noisy data from the vicinity of a limit cycle are available.

2. CALCULATION OF TANGENTIAL VECTORS

The estimation of derivatives is very critical because experimental time series are allways contaminated with noise. Therefore we fit our data with Splines [1] of appropriate order, so that all necessary derivatives can be calculated from them.

3. IMPROVEMENTS OF THE DEQ FITTING PROGRAM

An existing FORTRAN–program was able to fit data of a special dimension N_{dim} up to a maximal polynomial degree N_{deg}. We implemented recursive mechanisms to get indices for the polynomials and recursion formulas for Legendre–Polynomials and their derivatives [2]. Now we can fit data of any dimension, specified at runtime of the program.
If data are distributed in phase space very uneven, absolute values of Legendre–Coefficients are no good measure of their importance. Using the fact that if $F = \sum c_k f_k(\vec{x}_n)$ is a least squares approximate to data y_n, the sum of square errors can be written as

$$\sum_n (y_n - F(\vec{x}_n))^2 = \sum_n y_n^2 - \sum_k c_k \sum_n y_n f_k(\vec{x}_n) = \sum_n y_n^2 - \sum_n F(\vec{x}_n)^2 \tag{3}$$

---

[*] Part of Ph.D.thesis

Therefore we calculate $w_k = \frac{c_k \sum_n y_n f(\vec{x}_n)}{\sum_n F(\vec{x}_n)^2}$. Big negative values of w_k indicate an uneven distribution of data in phase space and a bad contribution of the according coefficient to the fit, small values indicate unimportant coefficients.

4. FITTING NOISY DATA ON A LIMIT CYCLE

The attempt to reconstruct a DEQ very often fails when only data from the close vicinity of a limit cycle are available, i.e. if data contain no transients. We found that creating artificial transients improves the ability of the fit to "recognize" the presence of a stable limit cycle. This is accomplished by multiplication of the starting part of the time series with a linear function ascending from zero to one.

We demonstrate this with phase space trajectories based on a numerically integrated Van der Pol system [3] with Gaussian noise ($\sigma = 0.05 * (x_{max} - x_{min})$) added (Fig. 1).
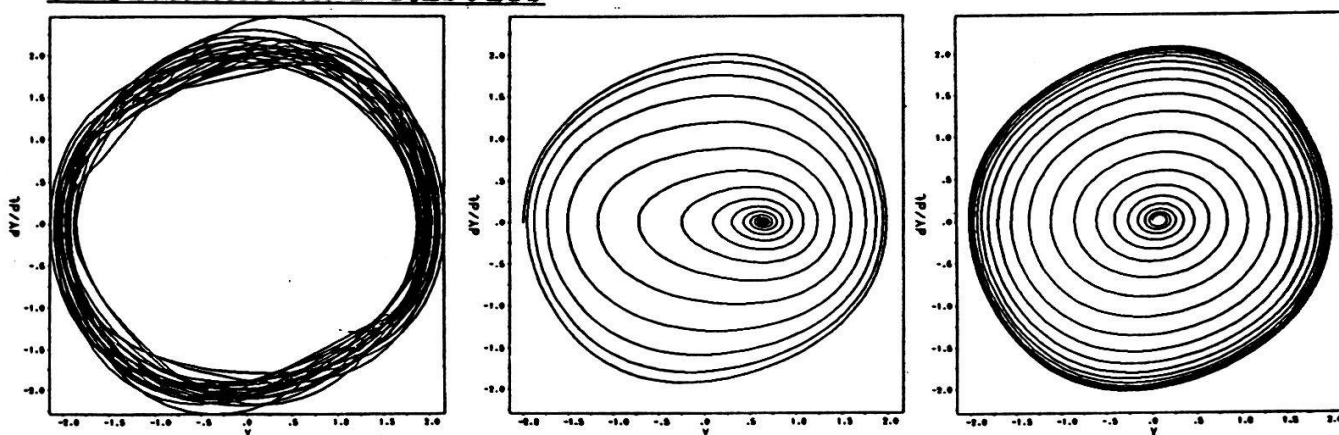
5. SUMMARY AND RESULTS

Figure 1: a) original data   b) reconstructed system   c) simulation of data with transient

With our new FORTRAN-programs we can reconstruct DEQ's of arbitrary dimension and polynomial degree. If only noisy data on a limit cycle (Fig. 1 a) are given, often the stability of the limit cycle is not recognized (Fig. 1 b). Generating artificial transients "guids" the fit to the right behavior (Fig. 1 c))

REFERENCES

[1] *IMSL Math/Library, Vers. 1.1, Vol 2.* Aug. 1989.

[2] M. Abramowitz and I. A. Stegun, editors. *Handbook of Mathematical Functions.* Dover Publications, Inc., New York, 1968.

[3] P. Bergé et al. *Order within Chaos.* John Wiley, 1986.

[4] A. Hübler. *Beschreibung und Steuerung nichtlinearer Systeme.* Ph.D. thesis, Technische Universität München, 1987.

[5] T. Kautzky et al. Rekonstruktion von Differentialgleichungen chaotischer und experimenteller Oszillatoren. *Helvetica Physica Acta*, 60:222, 1987.

THE ROLE OF DIFFRACTION IN OPTICAL NONLINEAR DYNAMICS

A.W. McCord,   Physikinstitut der Universitaet Zuerich, Irchel, Winterthurerstrasse 190, CH-8057 ZURICH, Switzerland

ABSTRACT: Examples of diffractive and vector nonlinear optics are presented.

In the semiclassical formalism, the behavior of nonlinear optical systems is described by Maxwell's equations of electromagnetism where the nonlinear polarization $\mathbf{P}$ induced in the medium by the light field is calculated quantum mechanically. By making a slowly varying envelope approximation in time and space, the following nonlinear vector wave equation for the electric field arises

$$\frac{\partial \mathbf{E}}{\partial z} + \frac{1}{2ik}\left[\frac{\partial^2 \mathbf{E}}{\partial x^2} + \frac{\partial^2 \mathbf{E}}{\partial y^2}\right] + \frac{1}{c}\frac{\partial \mathbf{E}}{\partial t} = \frac{ik}{2\epsilon_0}\mathbf{P} \ . \tag{1}$$

At this point two further approximations are almost always introduced. Firstly, the effect of transverse *diffraction* is neglected (the two terms in square brackets). Secondly, by assuming a fixed direction or sense of light polarization, this *vector* equation is projected to a *scalar* equation. Below we present two examples to illustrate the extremely rich behavior possible when these final two approximations are *not* made. The nonlinear medium under consideration here is a vapor of atoms with total electronic angular momentum quantum number $J=1/2$.

Fig 1 shows the spatial switching dynamics of the vector and diffractive generalization [1] of the well-known phenomenon of Optical Bistability in a passive ring cavity. The intensities of left (labelled '+') and right ('-') handed circular field components are shown as a function of the radial coordinate r (in cylindrical symmetry), and time scaled to the inverse cavity decay rate. Initially both beams rapidly switch up to a linearly polarized ($I_+ = I_-$) transverse structure, but a subsequent (+)switch-up wave and (-)switch-down wave cause the

fields to switch again to a stable but unbalanced final structure (with a factor of 9 increase in total power).

The second example shows a 'collision' of two laser beams of opposite polarization without the assumption of cylindrical symmetry [2] and with no external cavity feedback. Fig 2 shows the beam cross section (a) before, and (b) after collision. For the parameters of this simulation, the beams have mainly passed through each other. However, fragments of pure circularly polarized radiation have formed around the collision point. By doing this the system has organized itself so as to minimize the total power loss from either beam by spontaneous emission.
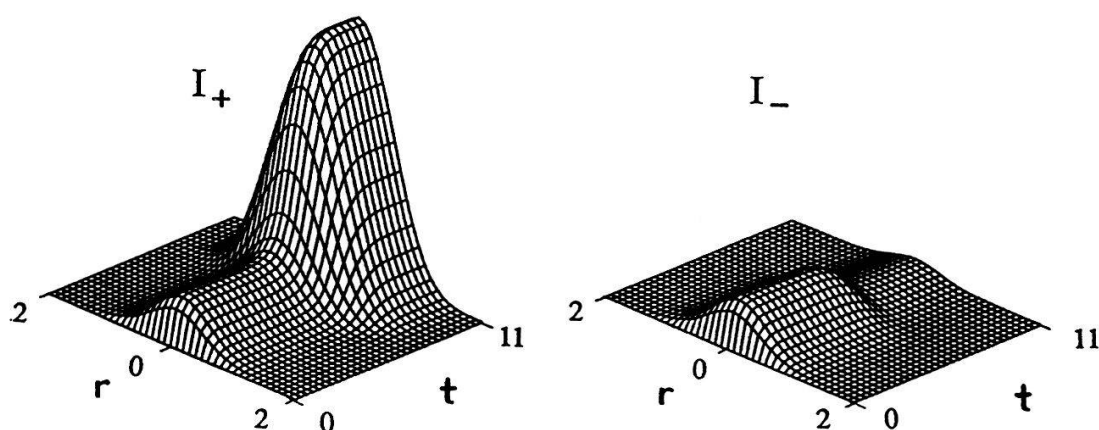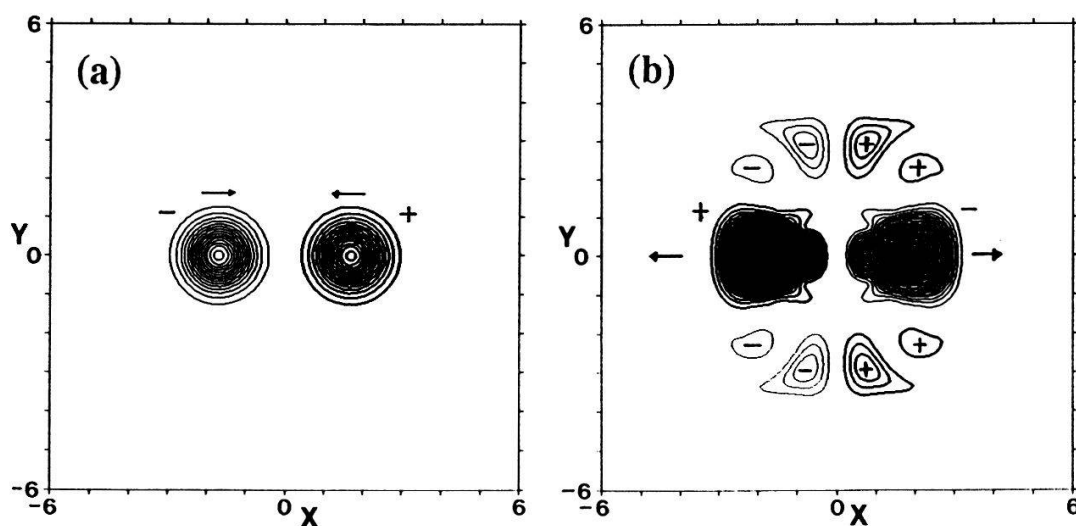

Figure 1

Figure 2

[1] A.W.McCord (To appear).

[2] A.W.McCord and R.J.Ballagh, J.Opt.Soc.Am.B, 7,73(1990).

DESIGN OF AN OPTICALLY BISTABLE FABRY-PEROT DEVICE BASED ON ALL-EPITAXIALLY GROWN AlGaAs

B. Acklin[1] and M.A. Dupertuis[2]

[1]Institut de Microtechnique de l'Université, Rue A.-L. Breguet 2, 2000 Neuchâtel

[2]Institut de Micro- et Optoélectronique, Ecole Polytechnique Fédérale, 1015 Lausanne

Abstract: A bistable Fabry-Perot (FP) device consisting of an optically nonlinear semiconductor spacer layer sandwiched between two Bragg mirrors has been optimized for use in reflection. Using a self-consistent carrier density model based on published experimental data for the nonlinear material the operating wavelength and spacer width have been numerically optimized for minimum threshold intensities. A prototype device has been designed, and its sensitivity to variations of the design parameters has been investigated.

1.   Introduction

Optically addressable 2-dimensional spatial light modulators in combination with free-space propagation may be an issue in telecommunications and parallel processing applications, where a large number of channels have to be routed or switched in parallel.

Nonlinear FP devices grown all-epitaxially in semiconductor materials [1] have two advantages compared to waveguides: Due to their short interaction length, they can take advantage of the large resonant refractive nonlinearities close to the absorption edge in direct gap semiconductor materials. Using standard processing techniques, 2-dimensional arrays with a large number of independent devices can be implemented on the same chip.

2.   Analytical optimization of the cavity mirrors

The reflectivity at resonance (on-state) of a dissipative linear FP cavity, including a spacer layer of length D with absorption coefficient α vanishes, if the reflectivities R_f and R_b of the front and back mirrors are chosen according to the condition

$$R_f = R_b \cdot (1-A_f)^2 \cdot e^{-2\alpha D} , \tag{1}$$

where A_f is the absorption in the front mirror. Hence a high switching contrast and, together with $R_b \approx 1$, a high signal efficiency can be achieved, as the corresponding off-resonance reflectivity (off-state) $R \approx 1-A_f$ is close to unity.

3.   Numerical optimization of the wavelength and the spacer width

A numerical model based on the self-consistent iteration of the steady state rate equation

$$\partial N/\partial t = \alpha(N,\lambda)<I_{cav}>D - (N-N_{th})/\tau_{rec} = 0 \tag{2}$$

for the carrier density N, using interpolated experimental data for the nonlinear optical properties

$\alpha(N,\lambda)$, $\Delta n(N,\lambda)$ of GaAs [3] and a longitudinal average intensity $\langle I_{cav}\rangle_D$ inside the FP spacer, was implemented to determine the optimum operation wavelength λ, as well as the spacer width D. In a first step the model neglects diffraction, carrier diffusion and standing wave effects.

The simulations predict bistable optical behavior with about $10kW/cm^2$ threshold and 10ns switching time for a reflective FP-cavity enclosing a $2\mu m$ bulk GaAs spacer. The optimum FP-resonance is located about 20meV below the GaAs gap energy, independent of cavity length. The model confirms the expected [2] lower switching threshold intensities for shorter cavities (Fig. 1), but the price to pay is an increased sensitivity of threshold and contrast on the wavelength detuning and growth parameters, which makes spacer widths below about 0.5 μm unrealistic.
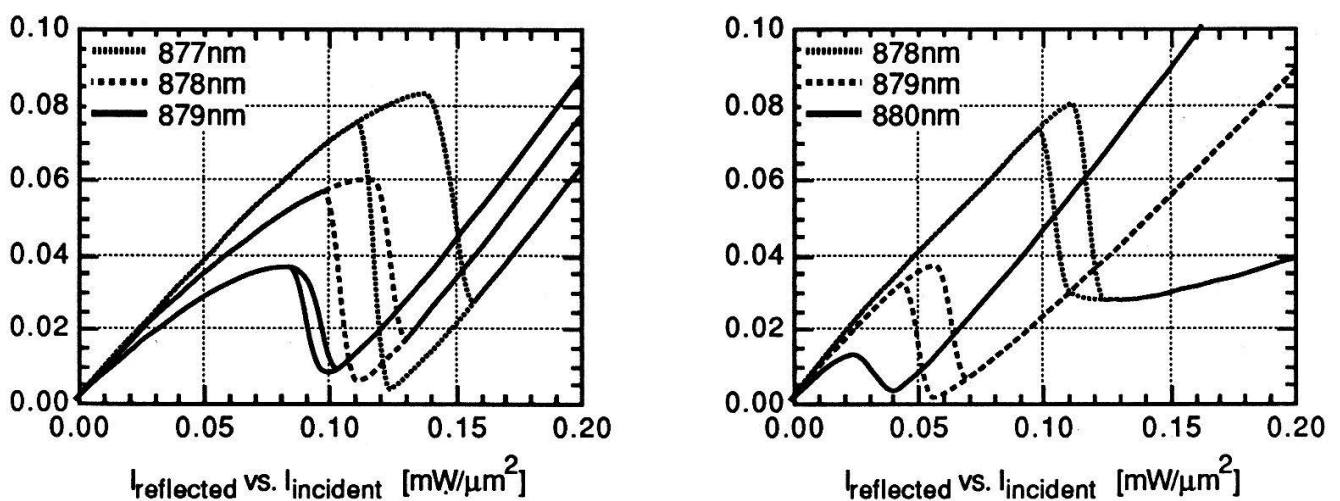

Fig.1   Response of a $2\mu m$ (left) and a $.5\mu m$ (right) cavity at various detunings from $\lambda_{res}=882nm$.

4.   Conclusions

Refractive nonlinear FP devices can be optimized for use in reflection by appropriate choice of the Bragg mirror reflectivities. Low threshold operation of bistable GaAs FP devices is expected for resonance wavelengths around 882nm and spacer widths between 0.5 and $2\mu m$. Two such devices were designed to verify the theoretical predictions related to short cavities. The limiting parameters for device design and growth appear to be in the exact knowledge of the refractive index and the reproduction of the spacer width within 0.5%.

5.   References

[1]   Jewell J.L. et al., "GaAs-AlAs monolithic microresonator arrays," Techn. Digest OSA meeting on Photonic Switching **PDP1-1**, 3 (1987).

[2]   Miller D.A.B., "Refractive Fabry-Perot bistability with linear absorption: theory of operation and cavity optimization," IEEE J. Quantum Electron. **QE-17**, 306 (1981).

[3]   Lee Y.H. et al., "Room-temperature optical nonlinearities in GaAs," Phys. Rev. Lett. **57**, 2446 (1986).

A MECHANICALLY TUNED ULTRASONIC CALORIMETER.

O.Oehler, J.Wieland, D.Raillard and M.Schumacher, Institute for Quantum Electronics, Swiss Federal Institute of Technology, CH-8093 Zurich, Switzerland.

Abstract: The calorimeter allows the detection of periodic heat signals. The device is based on a mechanically tunable ultrasonic resonator. Investigations with a heat source represented by an optical wave guide showed a temperature resolution of 0.05 mK and a colorimetric resolution of less than 1 μW.

1.   Introduction

As described earlier [1, 2, 3] the temperature dependence of the velocity of sound (dv/dT = 0.59 m/s K in air at 300 K) can be used for calorimetric investigations. They are based on the temperature detection of the gas surrounding the sample by measuring the change in tuning of an ultrasonic resonator.

2.   Apparative layout

The ultrasonic resonator was generated by two identical ultrasonic transducers [4] which were arranged opposite of each other in a thermally controlled metal tube M (Fig. 1). The latter was representing the calorimeter housing. The transducers (one used as an emitter E, the other as a receiver R) were operated in acoustic resonance at a frequency of 220 kHz (O). One of them was fixed to a piezo-driven translator T. The phase of the signal from the receiver was compared to the one of the input signal. A signal proportional to the phase difference (P) was used to control the translator via a device Q which impose a charge. It was also fed to a digital storage oscilloscope D.
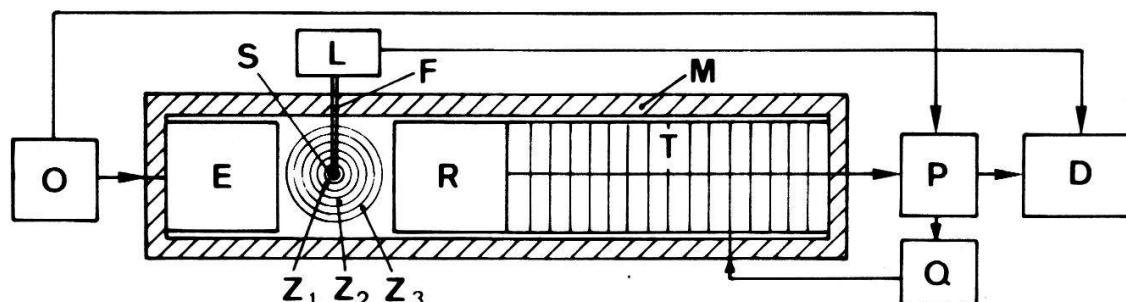

Fig. 1 Layout of the calorimeter

3.   Calorimetric investigations

The light absorbing end (black paint) of a glass fiber F was positioned at the center of the ultrasonic resonator. By guiding the 633 nm radiation of a He-Ne laser L through the fiber the black spot S and the surrounding air was periodically heated.

The spreading of the heat signal was calculated [5] by using the heat conductivity and the specific heat of the air on the basis of a shell model. This model describes the temperature variations inside the ultrasonic resonator at the zones Z_1, Z_2, Z_3 which are arranged concetrically around the heat spot at an equidistance of 1 mm (Fig. 1). These zones are separated by heat conducting layers of a width of 0.5 mm. The results given in Table 1 correspond to an absorbed light power of 103 μW at a chopping frequency of 0.22 Hz. The interaction between the partially heat conducting fiber and the zones Z_1, Z_2, Z_3 was taken into account in column I and was disregarded in column II.

From these values the volume-weighted averaged temperature variations in the temperature sensitive range of the ultrasonic resonator [3] were calculated. These averages are in satisfactory agreement with the experimental results obtained from the length variaton of the piezo-driven translator.

A heat power resolution of 1 μW and a corresponding temperature resolution of 0.05 mK was found with an integration time of 80 sec.

Table I Temperature variations in mK at the zones (103 μW, 0.22 Hz)

Zone	with fiber-zone interaction (I)	without fiber-zone interaction (II)
Z_1	28.6	12.6
Z_2	10.2	3.9
Z_3	3.5	1.3
average	13.2	5.5
exp.	6.3	

4.   References

[1]   O.Oehler, J.Wieland and S.Friedrich, Helv. Phys. Acta, **61**, 885 (1988).

[2]   O.Oehler, S.Friedrich and A. Schäppi, Springer Series in Optical Sciences, in press.

[3]   O.Oehler, P.Rusch and S. Dornbierer, Helv. Phys. Acta, in press.

[4]   Model E-188/220, Massa Products Corp., Hingham, Mass 02043, USA.

[5]   Computer program: Bionik, Dr. H. Weber, Vorstadt 6, CH-5200 Brugg.

LUMINESCENCE STUDY OF Zn DIFFUSED GaAs

Ky N.H., Araujo D., Pavesi L., Ganière J-D and Reinhart F.K.

Institut de Micro-et optoélectronique, Dept de Physique
Ecole Polytechnique Federale de Lausanne
CH 1015 LAUSANNE

1/Abstract

Zinc diffusions on Si-doped GaAs (n = 10^{18} cm-^{3}) samples were carried out in sealed evacuated quartz tube with $ZnAs_2$ source at 575 °C, 600 °C , 650 °C and 700 °C to study the influence of diffusion on the optoelectronic properties of the samples. We confirm that the mechanism of Zn diffusion involving gallium vacancies (V_{Ga}) plays an important role.

2/ Introduction

Diffusion of Zn into GaAs and AlGaAs is an important process for the fabrication of double heterostructure lasers, integrated optical devices, etc... Hence, the investigations of the physical mechanism for the Zn diffusion in GaAs is indispensable . For this purpose we have carried out Zn diffusions on Si doped GaAs (n = 10^{18} cm^{-3}) samples with the sealed - ampoule technique.

3/ Experiment

We sealed the prebaked at 750 °C ampoules at about 10^{-7} torr, and we used various diffusion temperatures and times: 700 °C (41min), 650 °C (5h20min), 600 °C (15h) and 575 °C (62h). The diffusion depth was measured by scanning electron microscopy (SEM), and the diffusion coefficient was determined from:

$$x = 2\sqrt{Dt} \quad (1)$$

where x is diffusion depth, D is diffusion coefficient and t the diffusion time. Figure 1 shows the dependence of the diffusion coefficient D with temperature. Our data are fitted by the relation:

$$D = D_0 \exp(-E_a/kT) \quad (2)$$
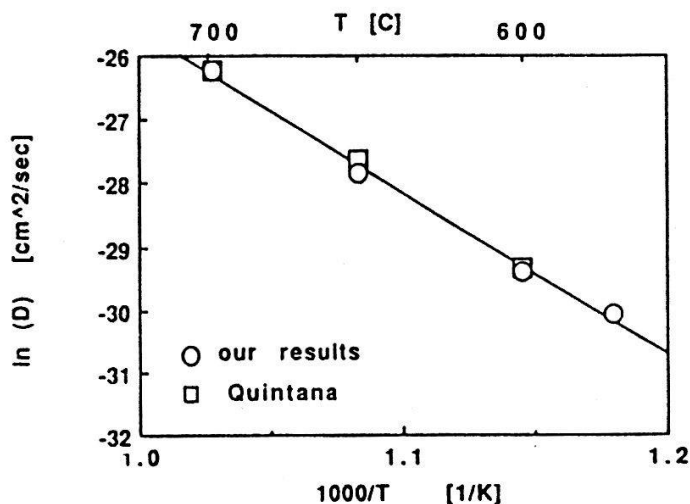
where D_0 = 1,1 cm^2/sec is the diffusion constant, E_A = 2,2 eV, k and T are the Boltzmann constant and the diffusion temperature respectively. Our values of D are close to the results obtained by Quintana V. and al.[1]. The difference in the values of D_0 (in their study D_0 = 42 cm^2/sec.) could be due to the different diffusion conditions. Our diffusions were carried out at a relatively high As-overpressure which enhances the Ga-vacancy concentration[2].

In Fig.2 we compare the PL spectra of the GaAs samples before Zn diffusion (Fig.2a) and after Zn diffusion (Fig.2b). The PL measurements were carried out at 300 K and 77 K.

Fig.1:dependence of D with T

The high energy bands at 1,485 eV (77 K) and 1,43 eV (300 K) in Fig.2a are probably due to band to band transitions and are shifted towards low energies with respect to the unperturbed band gap. The band gap narrowing is induced by the high doping density[3]. The band labeled '2' at 1.22 eV in Fig.2a is associated with a Ga vacancy donor complex[4]. After the Zn diffusion

(Fig.2b) this band disappeared and only the band to band transitions remains. The shoulder on the high energy side of the spectra is due to the Fermi edge[3]. Its appearance in the spectra at an energy close to the Fermi edge is a consequence of the Coulomb interaction between the photoexcited hole and the sea of electrons.
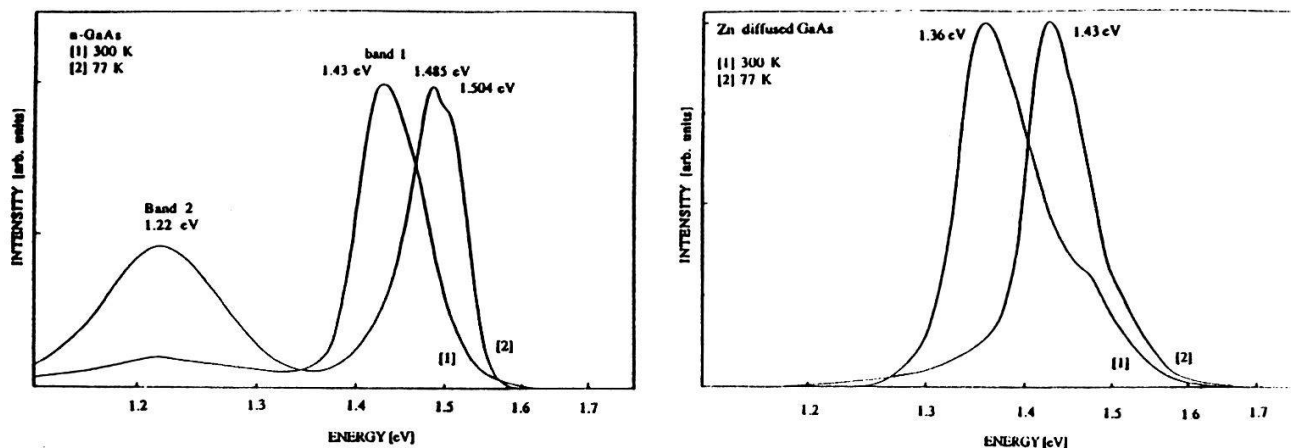
Fig.2: PL spectra A/ of the n-GaAs before diffusion and B/ of the p type after diffusion

4/ Discussion and Conclusion

We now discuss the mechanism of Zn diffusion into GaAs. Zn atoms may occupy substitutional sites on the GaAs sublattice as shallow acceptors (Zn^-_s) or intersititial sites as a shallow donor (Zn^+_i). The solubility of Zn_s is much greater than that of Zn_i, while the diffusitivity of Zn_i exceeds that of Zn_s by several orders od magnitude. The interchange between Zn_s and Zn_i can be explained by two models.
The Franck-Turnbull (or Longini) model[2] gives:

$$Zn_i^+ + V_{Ga} \Leftrightarrow Zn_s^- + 2h^+ \quad (3)$$

(where h^+ indicates holes, the concentration of which is determined by the concentration of Zn_s). The "kick-out" model involves gallium interstitials I_{Ga}[5] and it yields

$$Zn_i^+ \Leftrightarrow Zn_s^- + I_{Ga} + 2h^+ \quad (4)$$

Our results favor the first model. The disappearance of the band labelled "2" in our PL spectra after Zn diffusion is an evidence for the Franck-Turnbull (or Longini) mechanism of Zn diffusion involving Gallium vacancies V_{Ga} (2).
The PL results were confirmed by the other measurement: cathodoluminescence (CL), electron beam induced current (EBIC).

References:

[1] Quintana V. and al. J.Appl.Phys. 63, 2453 (1988)
[2] Tuck B. "Atomic diffusion in III-V semiconductors" (1988)
[3] Borghs G. and al. J.Appl.Phys. 66(9), 4381 (1989)
[4] Williams E.W. and Barry Bebb H. "Semiconductors and Semimetals" Vol.8, 195 and 359, (1972)
[5] Gösele U. and al. J.Appl.Phys. 52(7), 4617 (1981)

RF-sputter deposition of waveguiding LiNbO$_3$-layers

S.Schwyn, H.W.Lehmann

PSI c/o Laboratories RCA, Badenerstr. 569, 8048 Zürich

Abstract: Thin epitaxial films of LiNbO$_3$ of optical quality have been deposited by r.f.-sputtering on (001)-sapphire and (001)-LiTaO$_3$ substrates. TE$_0$ und TM$_0$ modes with moderate losses can be excited by prism coupling into a film deposited on (001)-sapphire. According to X-ray experiments the films are crystalline with c-axis aligned perpendicular to the substrate. TEM and electron diffraction measurements show anti-phase structures. Best films with least surface roughness are obtained at 500°C on both substrates. ESCA measurements show that the films have stoichiometric composition.

1. Introduction

LiNbO$_3$ is a key material for electrooptic, acoustooptic and nonlinearoptic applications. In integrated optics applications there is a considerable demand for single crystalline thin films of LiNbO$_3$. One of the most promising ways to fabricate these layers is r.f. sputtering. Waveguiding in single crystalline sputtered LiNbO$_3$-films has been reported by Takada et al. in 1974 [1], but could not yet be duplicated. In our paper we will report detailed characterization of the films as well as a waveguiding experiment.

2. Experimental

The LiNbO$_3$ films were grown in a conventional r.f. diode sputtering system. In order to obtain highly crystalline films, extremely low deposition rates of a few Å/min and high substrate temperatures are required to increase the surface diffusion of the arriving particles. We have therefore built a heater, which allows to reach substrate temperatures of up to 700°C even in a strongly oxidizing Ar/O$_2$ plasma. With the load-lock it is possible to exchange samples without venting the chamber. This results in a better vacuum in terms of basic pressure and residual gas composition.

Table I summarizes the usual sputtering parameters:

Target	LiNbO$_3$ stoichiometric, hotpressed (ø = 150 mm)
Target/Substrat spacing	40 mm
Basic/process pressure	10^{-6} mbar, 2×10^{-2} mbar
Gas/Flow	60% Ar, 40% O$_2$, 20 sccm
Power	50 W
Temperature	100°-600°C

With these conditions the deposition rate is as low as 2 Å/min.

3. Characterization

So far we have concentrated our experiments on the preparation of thin films of LiNbO$_3$ on (001)-sapphire and (001)-LiTaO$_3$ (substrate diameter 25 mm). The main parameter, which has

been varied was the temperature. SEM investigations show that films with minimum surface roughness are obtained at 500°C on either substrate (size of visible features ~0.1 μm).

The crystal structure of the films has been studied by X-ray and electron beam diffraction. θ-2θ diffraction show that films deposited at temperatures above 450°C are crystalline with a strong (006) peak indicating highly preferred orientation with the c-axis aligned perpendicular to the substrate.

In addition to these results, TEM investigations reveal a domain structure. The two alternating regions differ in their diffraction patterns only in the reflexes of the ± 1st and ± 3rd order in the c-direction, which in one case has a starlike pattern (Fig. 1.). This pattern can be interpreted as anti-phase structure [2]. Diffraction patterns at the interfaces show that there are areas, in which the layer is growing epitaxially and others where it relaxes.
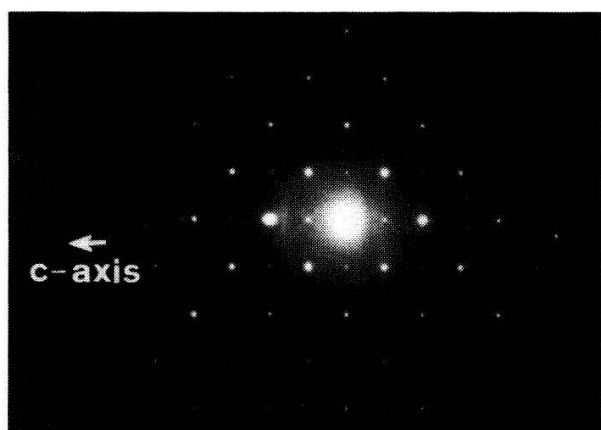

Fig. 1. Diffraction with starlike pattern in ± 1st and ± 3rd order in c-axis.
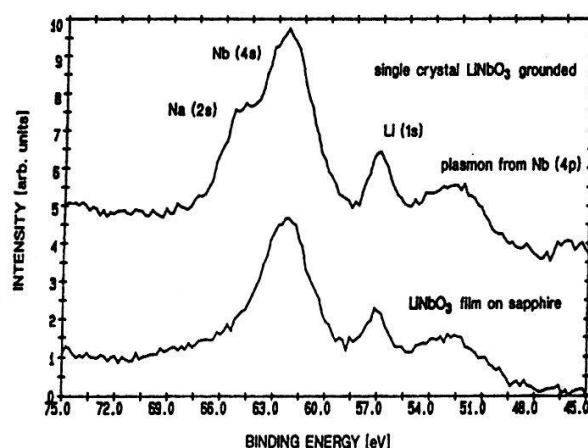
Fig. 2. ESCA spectrum of film deposited at 550°C on sapphire. The Na-peak is due to surface contamination of the reference crystal.

In order to determine the chemical composition of the films, ESCA measurements were performed. These showed a perfect agreement between spectra obtained from films and from single crystalline reference samples independent of the deposition temperature (Fig. 2.).

Films grown as described above can be used as waveguiding layers. TE_0 and TM_0 modes can be excited in these films by prism coupling. Due to the birefringence of the films the refractive indices could not be determined yet. The optical losses have not yet been accurately determined. However, it can be concluded from visual appearance, that the losses are relatively small and that sputtered films could be useful for applications in integrated optics.

Acknowledgements

References

[1]   S.Takada, Appl. Phys. Lett., 23, 490, (1974).

[2]   J.W. Edington, Practical electron microscopy in material science, Vol.2, p. 66, MacMillan, 1975.

Measurement of the electro-optic coefficients of GaAs at 1.32μm and 1.52μm

C-A Berseth, C. Wüthrich et F. K. Reinhart.
Institut de Micro- et optoélectronique, EPF Lausanne,
CH-1015 Lausanne

The linear (r_{41}) and quadratic (R_{11} and R_{12}) coefficients of GaAs are known for wavelengths up to 1.15μm. To study their dispersion, we have measured these coefficients for λ=1.32μm and λ=1.52μm. For the linear effect, we find good agreement with the tight-binding model. The results for the quadratic effect also agree qualitatively with the model based on electroabsorption.

Introduction

The linear electro-optic effect is thought to show little change with wavelength, whereas the quadratic term falls off rapidly with increasing wavelength. There is also a refractive index modulation due to free carriers which increases with wavelength. As this effect is not known with good precision, the structures used in these measurements are optimised to reduce its magnitude.

Principle of the measurements

The devices used are MBE-grown GaAs/AlGaAs rib waveguides on a [001]-oriented substrate. The direction of the waveguides is [110] or [1$\bar{1}$0]. The guiding layer is 0.44μm undoped GaAs. The claddings are $Al_{.26}Ga_{.74}As$. The first 0.3μm of the claddings are undoped. The dopings are then n=8x10^{17} cm^{-3} for the lower and p=1.8x10^{17} cm^{-3} for the upper cladding. This structure allows to apply a static electric field along [001] while reducing the overlap between free carriers and the optical field to a few percents. The maximum electric field is about 300 kV/cm.

The rib structure has been made by wet etching of the upper cladding, leaving 0.5μm of it on top of the GaAs layer. The ribs are 5μm wide. Length of the devices is 1.6mm for the [1$\bar{1}$0] direction and 2.8mm for the [110] direction.

Laser beams (HeNe for 1.52μm, YAG for 1.32μm) are used as probes to measure the refractive index (or rather its change).The waveguides act as Fabry-Perot cavities and a change of the refractive index will result in a change of the interference at the output of the device. From this intensity we calculate the phase change as a function of the electric field.

Results

Depending on the direction of propagation [110] or [1$\bar{1}$0] and the polarization (TE : electric field//GaAs layer , TM : $\perp$) the phase change has different terms :

- TE, [1$\bar{1}$0]   : $\phi(E) = \phi_0 + ar_{41}E + bR_{12}E^2 + \phi_{fc}(E)$
- TE, [110]   : $\phi(E) = \phi_1 - ar_{41}E + bR_{12}E^2 + \phi_{fc}(E)$
- TM , [1$\bar{1}$0] and [110] : $\phi(E) = \phi_2 \qquad + cR_{11}E^2 + \phi_{fc}(E)$

where a, b and c are known constants depending on the geometry of the devices and the wavelength. The signs and the absence of a linear term for the TM polarization are due to the symmetry ($\bar{4}$3m) of the GaAs cristal.

The analysis is done in the following way :

- subtraction of the two $\phi(E)$ relations for TE polarization leaves only the linear electro-optic effect. The results are

$r_{41}(1.52\mu m) = (-1.49 \pm 0.08)\times10^{-10}cm/V$ $r_{41}(1.32\mu m) = (-1.57 \pm 0.08)\times10^{-10}cm/V$

- addition of the same relations eliminates the linear term. It is not possible to separe the quadratic and free carrier terms. This is also the case for the TM measurements. We use a model [1] to estimate the magnitude of the free carrier effect. As this model is not very precise, the uncertainty for the quadratic effect will be quite large. The results are

$R_{11}(1.52\mu m) = (-3.2 \pm 2.5)\times10^{-17} cm^2/V^2$ $R_{11}(1.32\mu m) = (-9.2 \pm 3.0)\times10^{-17} cm^2/V^2$

$R_{12}(1.52\mu m) = (-4.1 \pm 2.5)\times10^{-17} cm^2/V^2$ $R_{12}(1.32\mu m) = (-5.1 \pm 3.0)\times10^{-17} cm^2/V^2$

Figure 1 shows the linear coefficient measured here along with those at shorter wavelengths from [1] and a theoretical calculation based on the tight-binding model from [2]. The dispersion of the measured coefficients agrees well with the model.

Figure 2 shows the quadratic coefficients R_{11} and R_{12} from this work with those from [1] and a model based on electro-absorption from [1]. This model does not include a difference between the two coefficients. As the results are not very precise, we cannot compare the magnitude of the coefficients. However, the dispersion (rapid fall-off with increasing wavelength) agrees well with the model.
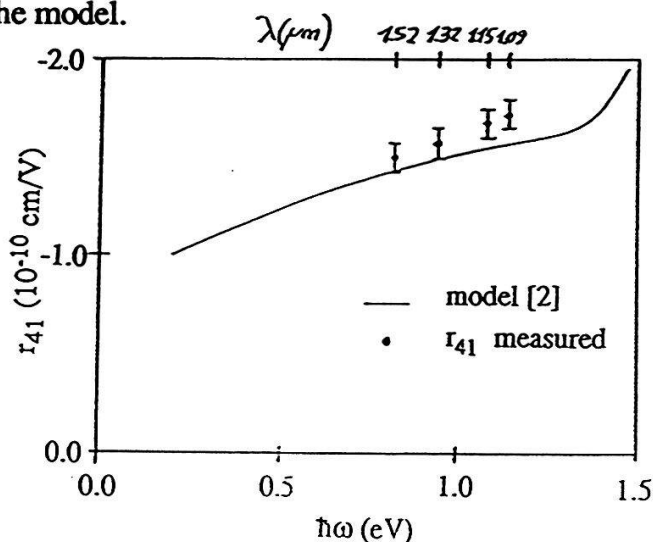

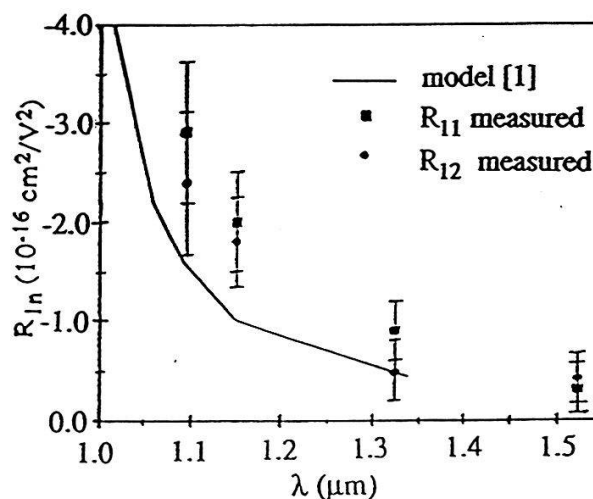Fig.1 Linear electro-optic effect   Fig.2 Quadratic electro-optic effect

Conclusion

The linear and quadratic electro-optic coefficients of GaAs have been measured at the wavelengths 1.32 and 1.52μm. These results show good agreement with theoretical models.

A more precise evaluation of the quadratic terms would require waveguides tailored to the wavelengths under investigation, and also other structures enabling a precise measurement of the free carrier modulation.

References

[1] J. Faist, Thesis report "Etude théorique et expérimentale de la modulation de phase dans les doubles hétérostructures GaAs/Al$_x$Ga$_{1-x}$As", EPFL 1988
[2] A. Hernandez-Cabrera, C. Tejedor and F. Meseguer, J. Appl. Physics 58(12) p.4666 (1985)

Fabrication et caractérisation de lasers à semiconducteur destinés au pompage optique d'étalons de fréquence au Cs.

S.Cao, C.Wüthrich, C-A.Berseth, J-D.Ganière, D.Martin, F.Morrier-Genoud et F.K.Reinhart
Institut de Micro et Optoélectronique
Ecole Polytechnique Fédérale de Lausanne
CH-1015 Lausanne

Les lasers à semiconducteur ont toujours plus d'applications [1] car ils sont efficaces, de petites dimensions et bon-marchés. Ils peuvent être utilisés par exemple pour pomper optiquement des étalons de fréquence [2], ce qui permet d'améliorer le rapport signal sur bruit de l'étalon. Les lasers à simple puits quantique sont de bons candidats pour le pompage optique du césium (λ=852.11 nm) car il est possible de contrôler la longueur d'onde d'émission en choisissant la bonne épaisseur pour le puits quantique. De plus les lasers à puits quantique ont un faible courant de seuil, une raie étroite [3] et un bon rendement quantique.

Nous avons réalisé des lasers AlGaAs/GaAs à simple puits quantique et à gradient d'indice (laser SQW-GRINSCH) à partir de croissances épitaxiales par jets moléculaires (MBE). Le puits quantique de GaAs a une épaisseur de 7,5nm. Le coeur du guide a une épaisseur de 300nm et est en $Al_xGa_{1-x}As$ de type n et p dont la valeur de x varie de 15% à 45%. Les claddings font 1.5 μm d'épaisseur et sont en $Al_{0.45}Ga_{0.55}As$. Un cap layer en GaAs de 200nm d'épaisseur, fortement dopé bérilium, permet d'obtenir de meilleurs contacts ohmiques.

Le processing utilisé est simple et ne demande aucun alignement précis des masques. Un masque de polyimide sert à la fois à l'attaque du guide pour le confinement latéral et au dépôt de la couche isolante de Si_3N_4. Pour le contact électrique, côté p, on dépose du Ti/Pt/Au et côté n du AuGe/Ni/Au. Les lasers ainsi réalisés ont des largeurs de 5,7 et 10μm; ils sont clivés aux longueurs de 300, 600, 750 et 1000 μm.

Les mesures électriques ont indiqué une résistance série de 10 ohm pour une diode de 5250 μm^2. Cette résistance a été abaissée à 3 ohm après diffusion de zinc dans le cap layer, ce qui montre la difficulté d'obtenir un dopage p élevé par croissance. La tension de claquage en inverse est de -8V. Les mesures optiques ont révélé un rendement quantique de 76% pour des lasers de 5μm de large et 300μm de long fonctionnant en mode pulsé (1μsec. , 200Hz). Le rendement quantique est plus faible en mode continu car la chaleur n'était pas évacuée de façon satisfaisante par le porte-échantillon. La densité de courant de seuil typique est de 1000A/cm^2 mais a pu être abaissée à 550A/cm^2 pour de longues structures (L=750μm). En mode continu nous avons obtenu une puissance maximum de 55mW par face pour une largeur de stripe de 10μm.

Suivant l'emplacement dont les lasers proviennent sur la croissance, la lumière émise a une longueur d'onde comprise entre 850 et 860 nm. Le champ à grande distance (Far-field) des lasers de 5 µm de large correspond à une gaussienne, ce qui démontre l'absence de mode latéraux. Les spectres obtenus à l'aide d'un monomochromateur de 1 mètre de focale montrent une bonne monomodicité, le taux de réjection des modes adjacents est supérieur à 10dB.

Nous avons réalisé des lasers SQW en GaAs/AlGaAs à l'aide d'un processing simple. Les structures obtenues ont une faible densité de courant de seuil (550 A/cm2) un rendement quantique différentiel élevé (76%) et une puissance maximale de 55mW. Par ailleurs nous avons obtenu un fonctionnement monomode, latéralement et longitudinalement. Des mesures préliminaires ont montré que la largeur de la raie était inférieure à 10 MHz.

[1]   A.Yariv, "Quantum Well Semiconductor Laser are taking over", IEEE Circuits and Devices Magazine, 1989, Vol.5, No6, pp 25-28.

[2]   P.Thomann, F.Hadom, "Short-term stability of a commercial optically pumped Cs tube,3rd European Frequency and Time Forum, Besançon, 21-23 mars 1989.

[3]   C.H. Henry, "Theory of the Linewidth of Semiconductor Lasers", IEEE Journal of Quantum Electronics, QE-18, No2, février 1982

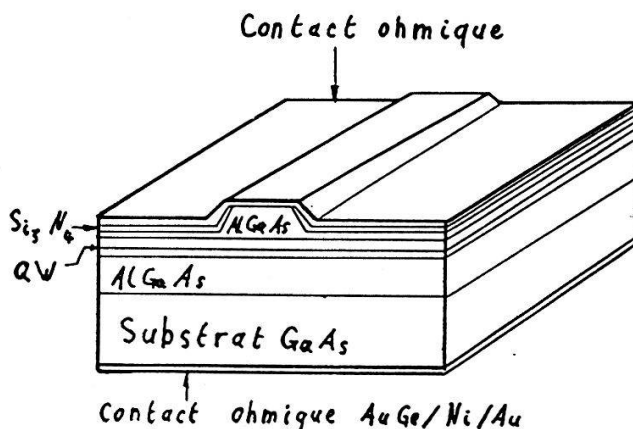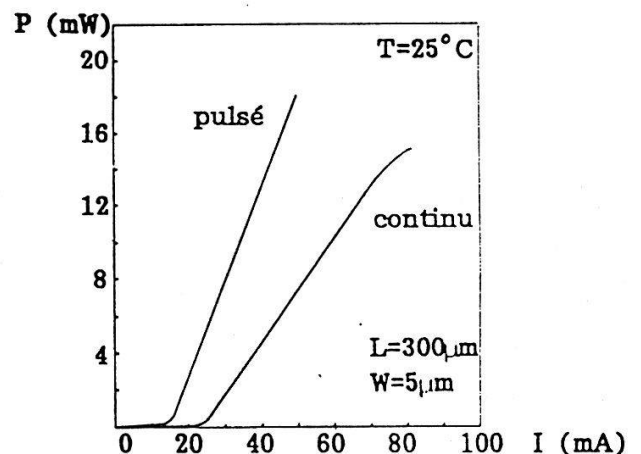[4]   H.C.Casey, M.B.Panish, "Heterostructure Lasers", Academic Press, New-York, 1978

Fig.1

FIG.2

Fig.1: Structure schématique d'un laser
Fig.2: Puissance lumineuse en fonction du courant injecté

AN EFFICIENT ALGORITHM FOR SOLVING SYSTEMS OF EQUATIONS

Gérard Schibler
Institut de physique théorique, Université de Lausanne, CH-1015 Lausanne, Switzerland.

Abstract: In many physical applications, systems of equations have to be solved numerically. Starting from a procedure used in molecular dynamics, we devised and present here an iterative algorithm for solving linear systems and, in certain cases, non-linear systems. The algorithm, based on the contracting map principle, deals with one equation at a time, and will converge for any system which has a solution. One version of the method proves effective for solving large sparse systems.

1. INTRODUCTION

One procedure [1] for performing dynamical simulations of complicated molecules is such that, many times during each simulation, a system of (non-linear) equations has to be solved. The present work deals with a justification, improvement, and generalization of the technique used in the solution of these equations.

2. THE ALGORITHM IN THE LINEAR CASE

The main tool we use is the following lemma, whose proof is simple and is omitted. E denotes a real, finite-dimensional vector space, equipped with a scalar product (symmetric, positive-definite bilinear form).

Lemma. Let $V_1, \ldots, V_k$ be subspaces of E, $V = \bigcap_{i=1}^{k} V_i$, P_i the orthogonal projection of E onto V_i ($1 \leq i \leq k$) and P the orthogonal projection of E onto V.
Then: $P_k \cdots P_1 = P + S$, where $\|S\| < 1$ and $PS = SP = 0$.

Note that, as a consequence of this result : $(P_k \cdots P_1)^l \to P$ exponentially as $l \to \infty$, the error being $\sim \|S\|^l$.
Now, let

$$\sum_{j=1}^{n} a_{ij} x_j = b_i \quad (1 \leq i \leq m) \tag{1}$$

be a linear system. We assume that no line of the matrix (a_{ij}) is identically zero. For all $1 \leq i \leq m$, let $H_i = \{x \in \mathbf{R}^n | a_{i1} x_1 + \ldots + a_{in} x_n = b_i\}$ be the set of points in $\mathbf{R}^n$ satisfying the i-th equation of (1), and $H_i^0 = \{x \in \mathbf{R}^n | a_{i1} x_1 + \ldots + a_{in} x_n = 0\}$. H_i^0 is a hyperplane of $\mathbf{R}^n$ (subspace of dimension $n-1$) and H_i is obtained from H_i^0 by a translation by any vector in H_i. Suppose that (1) *has* a solution z, i.e. $z \in \bigcap_{i=1}^{m} H_i$. We have $H_i = z + H_i^0, \forall 1 \leq i \leq m$. Consequently, the geometry of the H_i's with respect to z is the same as the geometry of the H_i^0's with respect to the origin. We now show how this fact allows us to use the lemma. First note that, for the usual scalar product on $\mathbf{R}^n$, $(H_i^0)^\perp$ is the line spanned by a_i, where $a_i = (a_{i1}, \ldots, a_{in})$. For $1 \leq i \leq m$ and $y \in \mathbf{R}^n$, define $f_i(y)$ as the intersection of H_i with the line parallel to $(H_i^0)^\perp$ passing through y. Explicitly :

$$f_i(y) = y + \lambda_i(y) a_i \quad \text{where} \quad \lambda_i(y) = \frac{b_i - y \cdot a_i}{\|a_i\|^2} \tag{2}$$

Denote by F the composition $F = f_m \circ \ldots \circ f_1$ and by P the orthogonal projection of $\mathbf{R}^n$ onto $\bigcap_{i=1}^m H_i^0$. Then a few simple calculations and the lemma show that, for all $y \in \mathbf{R}^n$, $F^l(y)$ converges exponentially to $\bar{y} := z + P(y - z)$ as $l \to \infty$; now $\bar{y}$ is easily seen to be the solution to (1) closest to y, and we can state the

Algorithm. a) Starting from any $y \in \mathbf{R}^n$, compute $f_1(y), f_2 \circ f_1(y), \ldots, f_m \circ \cdots \circ f_1(y)$;
b) Replace y by $f_m \circ \cdots \circ f_1(y)$ in a) and apply a) again.

Remarks : a) Contrarily to some existing iterative methods for solving linear systems (e.g. Jacobi, Gauss-Seidel ([2], vol.1)), here no condition is required on the matrix (a_{ij}).
b) Because it is based on a contraction principle, the algorithm is numerically stable, i.e. small computational errors do not prevent it from converging.
c) There are cases where the convergence is very slow (which corresponds to $\|S\|$ near 1).

The difficulty raised in remark c) can be remedied by using appropriate projections instead of orthogonal ones. For simplicity, assume that $\mathrm{rank}(a_{ij}) = m$, i.e. that the vectors a_i are linearly independent. Let $v_1, \ldots, v_m$ be vectors obtained by Gram-Schmidt orthogonalisation of $a_1, \ldots, a_m$. Note that if a_{ij} is sparse, obtaining the v_i's is easy. Let us modify the above algorithm by using these new vectors as directions of projection. The expressions in (2) are replaced respectively by: $g_i(y) = y + \mu_i(y)v_i$ and $\mu_i(y) = (b_i - y \cdot a_i)/(a_i \cdot v_i)$. Then it can be shown that $\forall y \in \mathbf{R}^n : g_m \circ \ldots \circ g_1(y) = \bar{y}$ ($\bar{y}$ as above). In other words, with this modified algorithm, $\bar{y}$ is found in a finite number (m) of steps. In practice, because of numerical errors, one can use the point found after m steps as a new initial point and start again; about $3m$ steps may be necessary to reach a good accuracy.

A comparison was conducted with the conjugate-gradient (CG) method ([2], vol.2) which is also a generally applicable, "finite-iterative" method. We considered a 200×200 matrix with 20% non-zero elements. For a given computation time, the accuracy reached with the modified algorithm surpassed that of the CG method.

3. Non-Linear Systems

Let $\{\varphi_i(x) = 0\}$ $(1 \leq i \leq m,\ x \in \mathbf{R}^n)$ be a non-linear system. We suppose that the vectors $\mathrm{grad}\varphi_i$ $(1 \leq i \leq m)$ are linearly independent in a certain region. An algorithm of solution can be deduced from the linear algorithm by a suitable linearization : a) Choose an initial point $y^{(0)} \in \mathbf{R}^n$; b) For $1 \leq i \leq m$, define $y^{(i)}$ inductively as follows: Linearize φ_i at $y^{(i-1)}$ and solve the correponding linear equation as above, i.e. moving from $y^{(i-1)}$ in the direction of $\mathrm{grad}\varphi_i(y^{(i-1)})$. Explicitely : $y^{(i)} = y^{(i-1)} - (\varphi_i(y^{(i-1)})/\|\mathrm{grad}\varphi_i(y^{(i-1)})\|^2) \cdot \mathrm{grad}\varphi_i(y^{(i-1)})$.
c) Replace $y^{(0)}$ by $y^{(m)}$ in b) and start b) again.
It can be shown that this algorithm converges to a solution to the system, provided $y^{(0)}$ was close enough to the set of solutions.

REFERENCES
[1] J.P. Rickaert et al. *Numerical Integration of the Cartesian Equations of Motion of a System With Constraints.* J. Comput. Phys. **23** (1977), 327.
[2] J. Stoer, R. Bulirsch. *Einführung in die Numerische Mathematik.* Springer, 1983 (vol.1) and 1978 (vol.2).

Numerical simulations of the one-dimensional t-J model.

F.F. Assaad and D. Würtz
IPS-IFWD29.2, ETHZ, 8092 Zürich, Switzerland

Abstract. *We investigate the physics of the one-dimensional t-J model through the use of the quantum transfer matrix technique and the quantum Monte Carlo world line algorithm. We present preliminary results on thermodynamic quantities, as well as on charge and spin correlation functions.*

$$H = -t \sum_{i,\sigma}(1 - n_{i+1,-\sigma})c^{\dagger}_{i+1,\sigma}c_{i,\sigma}(1 - n_{i,-\sigma}) + 2J \sum_i (\vec{S}_{i+1}\vec{S}_i - \frac{1}{4}n_{i+1}n_i)$$

defines the Hamiltonian of the one-dimensional t-J model. Here, $c^{\dagger}_{i,\sigma}$ creates an electron on site i with z-component of spin σ, $n_{i,\sigma} = c^{\dagger}_{i,\sigma}c_{i,\sigma}$, and $\vec{S}_i$ is the spin operator at site i. Electrons on the ring (we assume periodic boundary conditions) are thus submitted to a next neighbour Heisenberg interaction and are allowed to hop between adjacent sites. Since double occupancy is prohibited the model reduces to the Heisenberg chain in the special case of one electron per site (i.e. half band filling). For small values of J/t, H is equivalent to the large U Hubbard model, which scales to the Tomonaga-Luttinger model [1]. At $J/t = 1$, the t-J model may be solved exactly by means of the Bethe-Ansatz [2]. The aim of this work is to provide an understanding of the electronic structure as a function of the coupling J/t and the band filling. In order to do so, we have used two algorithms: the quantum M.C. world line method (large lattices but results submitted to statistical uncertainty) and the quantum transfer matrix method (small lattices but exact results) [3]. Both algorithms evaluate the canonical partition function and thus produce thermodynamic quantities.

We present preliminary results obtained with the world line algorithm for the charge and spin structure factors at quarter band filling (i.e. $\rho = 0.5$) and values of J/t ranging from 0.5 to 1.625. For $J/t < 1$, the spin and charge structure factors show the same qualitative structure as in the large U Hubbard model: a cusp at $4k_f$ ($k_f = \rho\pi/2$) in the charge and one at $2k_f$ in the spin. The magnitude of both cusps is reduced as the coupling J/t is enhanced. For $J/t \geq 1$ a set of very interesting phenomena occur. First of all, at $J/t = 1$, the $4k_f$ charge cusp disappears leaving place to a $2k_f$ one. The $2k_f$ spin cusp is however still present. As J/t is enhanced away from 1, the spin structure factor looses its $2k_f$ cusp and develops a maximum at wave vector $k = \pi$. At $J/t = 1.5$, no evident structure is detectable in both the spin and charge structure factors. (A differentiable charge (spin) structure factor leads to an exponential decay of the real space charge (spin) correlations). Finally, for $J/t \geq 1.625$ phase separation occurs. A caricature of the phase separated state may be obtained by placing the electrons antiferromagnetically on one side of the lattice and the holes on the other side. The Heisenberg energy is thus minimized at the expense of the kinetic energy. We are presently carrying out further simulations in the range $1 \leq J/t < 1.6$ so as to clarify the nature of the apparent transitions in this parameter range.

Figure Captions
Fig 1a, 1b. Spin structure factor. The wave vectors k are denoted in units of $2\pi/L$ ($4\pi/L$) for the 24 (48) site ring. For both lattice sizes one has: $2k_f \equiv 6$ and $4k_f \equiv 12$.
Fig 2a, 2b. Charge structure factor. (Same units as above.)

References

[1] S. Sorella, A. Parola, M. Parrinello, E. Tosatti, Sissa Preprint 127CM October 1989.
M. Ogata, H. Shiba Preprint 1989 Submitted to Phys. Rev. B.
[2] P.A. Bares, G. Blatter ETHZ Preprint 1989.
[3] Proc. of the Int. Workshop on Quantum Simulations of Condensed Matter Phenomena. Los Alamos 1989, World Scientific publications. and references therein.

Fig. 1a

Fig. 1b

Fig. 2a

Fig. 2b
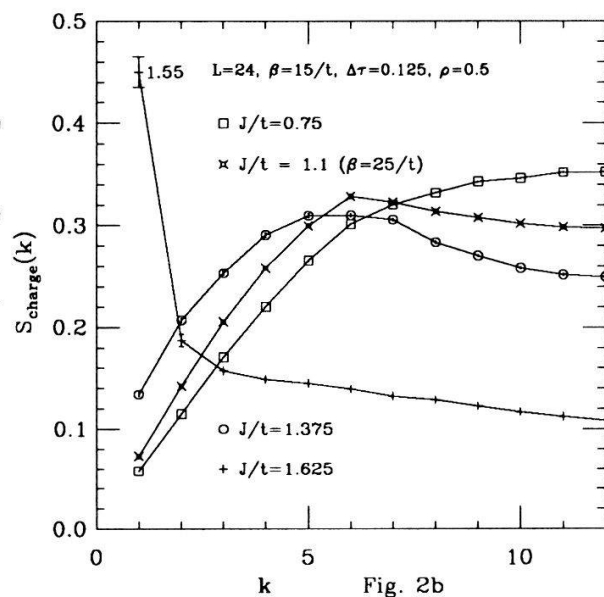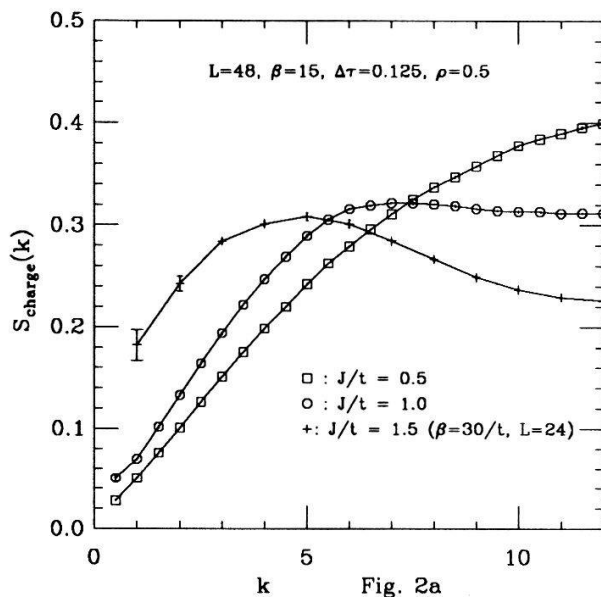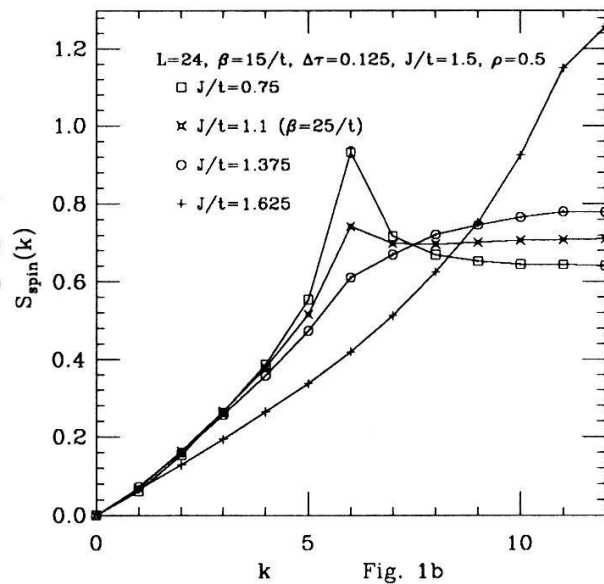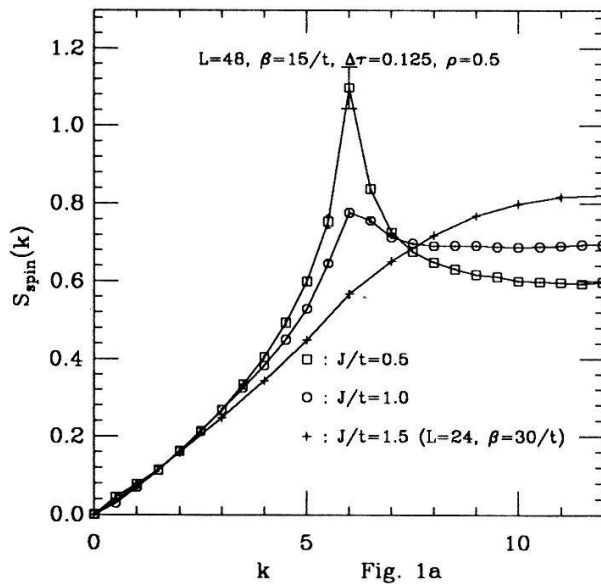
Simulated annealing and evolution strategy — a comparison

Claas de Groot[1], Diethelm Würtz[1], and Karl Heinz Hoffmann[2]
[1]*IPS D29.2, ETH-Zentrum, CH-8092 Zürich*
[2]*Institut für theoretische Physik, Universität Heidelberg, D-6900 Heidelberg*

Abstract: We compare two optimization algorithms which glean their heuristic from nature: simulated annealing and evolution strategy. These algorithms are applied to two different difficult optimization problems which present themselves in a physical context as calculations of ground states with respect to certain Hamiltonians. Our two Hamiltonians belong to short range two dimensional spin glasses and an autocorrelation function on a linear binary sequence which can be considered as a chain of long range interacting spins. Our results show a problem dependence of the behaviour of the algorithms. While simulated annealing performs slightly better in the case of spin glasses, our evolution strategy for the autocorrelation function finds better results than ever obtained by other stochastic methods.

Optimization is a very common task in many areas ranging from daily life to theoretical physics. It can be stated very generally in mathematical terms considering a configuration space S, a cost function f, and restrictions or boundary conditions B (e.g. minimization):

$$\text{Find } s_0 \in S: \qquad f_{opt} = f_{min} = f(s_0) = \min_{s \in S} f(s)\big|_B.$$

The standard problem solvers such as linear programming often require certain mathematical properties of the mathematical model at hand. Thus there is the need for more general optimization algorithms which were developed especially to cope with two of the most common algorithmic difficulties in the optimization process: local optima and premature convergence. The *simulated annealing* algorithm [1] is based on the idea of interpreting the solidification of a crystal as an optimization process. The *evolution strategy* algorithm [2] gets its ideas from the observation that nature performs an optimization process while selecting creatures to a higher and higher level. We performed a comparison of these two algorithms by applying them to physical problems. For these problems were able to compare the optimization to the exact results which we gained from complete enumeration of the configuration space. The criterion for these comparisons was the number of function evaluations per optimization. This seems to be a reasonable criterion for theoretical comparisons of algorithmic performance.

First we investigated the two dimensional spin glass Hamiltonian [3]

$$-\beta H = \sum_{\{i,j\}} J_{ij} S_i S_j$$

where the $S_{i,j}$ are Ising-spins and the J_{ij} are nearest-neighbour interactions either gauss-distributed or discrete. The results show a slight advantage of the simulated annealing algorithm (see Table 1 and 2).

Our second problem was the minimization of the autocorrelation of a binary sequence which can be characterized by an "energy" E, or a "merit factor" F respectively:

$$R_k = \sum_{i=1}^{N-k} S_i S_{i+k}; \qquad E = \sum_{k=1}^{N-1} R_k^2; \qquad F = N^2/(2E).$$

This originally technical problem can be seen as a four spin long range interaction on a one dimensional chain [4]. We compared our evolution strategy to results obtained by Bernasconi using simulated annealing [5]. We also performed a complete enumeration of the configuration space to visualize its complicated structure [6] (see Fig. 1). The results show that our evolution algorithm is performing better on this problem than simulated annealing. The extrapolation to an infinite population size comes much closer to the presumable optimum than the limit of infinite slow cooling with simulated annealing (see Fig. 2). Our results thus show a problem dependence. One also has to state that the optimization results strongly depend on the effort one undertakes to obtain them. So general statements about the performance of algorithms have to be set up with some care.

Table 1

$\pm J$-model, 14 × 14 sites, $J \in \{\pm 1\}$

Degeneracy	Exact	Evolution	Annealing
1718496	-1.4176	-1.3848	-1.3974
1215648	-1.4286	-1.3938	-1.4040
812903040	-1.3956	-1.3710	-1.3807
73462548	-1.4396	-1.4185	-1.4303
3888128	-1.4396	-1.4123	-1.4277
1673280	-1.4396	-1.4086	-1.4204
3654000	-1.4396	-1.4055	-1.4187
589510350	-1.4176	-1.3829	-1.4075
139033752	-1.4066	-1.3870	-1.3974
4202880	-1.3956	-1.3514	-1.3743
Mean	-1.4220	-1.3916	-1.4058

Fig. 1 $N=47$

Table 2

Gauss-model, 14 × 14 sites, $\bar{J} \approx 0$, $\sigma_J^2 \approx 1$

Degeneracy	Exact	Evolution	Annealing
2	-1.3165	-1.2710	-1.2809
2	-1.3377	-1.2891	-1.2946
2	-1.3297	-1.2774	-1.2920
2	-1.4384	-1.3922	-1.4006
2	-1.4346	-1.3929	-1.3948
2	-1.4098	-1.3633	-1.3673
2	-1.3665	-1.3309	-1.3320
2	-1.4465	-1.3832	-1.4134
2	-1.4207	-1.3725	-1.3788
2	-1.4231	-1.3864	-1.3852
Mean	-1.3923	-1.3459	-1.3540

Fig. 2 $N=49$ (skew-symmetric)
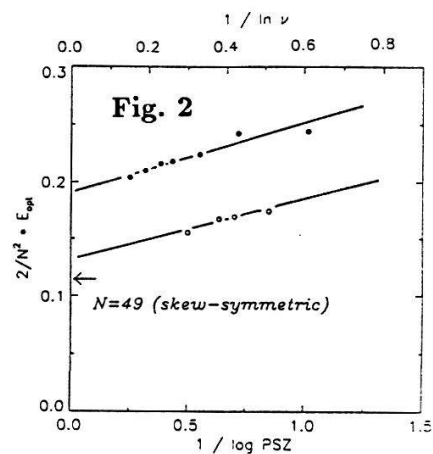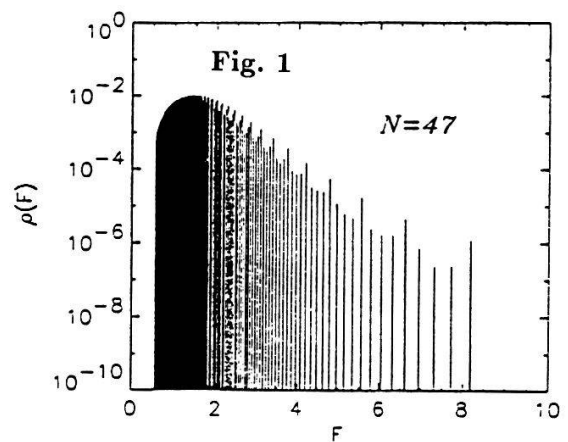
References

[1] S. Kirkpatrick, C.D. Gelatt, M.P. Vecchi, Science 220, 671 (1983). P. van Laarhoven, E. Aarts, Simulated Annealing: Theory and Applications, Reidel, Dordrecht, 1987.

[2] I. Rechenberg, Evolutionsstrategie, Frommann-Holzboog, Stuttgart, 1973. H.-P. Schwefel, Numerische Optimierung von Computer-Modellen mittels der Evolutionsstrategie, Birkhäuser, Basel, 1977.

[3] I. Morgenstern, J.L. van Hemmen [ed.], Heidelberg Colloquium on Glassy Dynamics, Springer, Heidelberg, 1986/1987.

[4] M.J.E. Golay, IEEE Trans. Inf. Theory, IT-18, 449 (1972). IT-23, 43 (1977). IT-28, 543 (1982).

[5] J. Bernasconi, J. Physique 48, 559 (1987).

[6] C. de Groot, D. Würtz, K.H. Hoffmann, IPS Research Report No. 89-09. C. de Groot, Diploma Thesis, Heidelberg, 1989.

PROBABILITY DENSITIES FOR DISCRETE DYNAMICAL SYSTEMS WITH WEAK NOISE

P.Reimann, Institut für Physik, Klingelbergstr. 82, CH-4056 BASEL, Switzerland
P.Talkner, Paul Scherrer Institut, CH-5232 VILLIGEN, Switzerland

Problem and Model

The determination of stationary probability densities in multidimensional non-equilibrium systems in the presence of weak noise is of great importance in many cases [1] but plagued by notorious difficulties. It is widely believed that often useful predictions for the full system can be obtained by the restriction on a stroboscopic time-discretization of a single state-variable. As a model system we consider the following Langevin equation in discrete time n for the single variable x

$$x_{n+1} = f(x_n) + \xi_n = x_n + \frac{b}{2\pi} \sin(2\pi x_n) + \xi_n \tag{1}$$

where the noise term ξ_n represents an analogue of the random force in the time-continuous case. For the sake of simplicity ξ_n is assumed to be independent and identically Gaussian distributed: $P(\xi_n \in [\xi, \xi + d\xi]) = (2\pi\epsilon)^{-1/2} exp(-\xi^2/2\epsilon) \, d\xi$ with small noise strength $\epsilon \ll 1$ [2]. Under these assumptions the stationary probability density $W_\epsilon(x)$ satisfies the following integral equation [2]

$$W_\epsilon(x) = \frac{1}{\sqrt{2\pi\epsilon}} \int_{-\infty}^{+\infty} e^{-(x-f(y))^2/2\epsilon} \, W_\epsilon(y) \, dy \tag{2}$$

The usual analytic and numerical methods for solving integral equations fail to give the correct asymptotic behaviour for weak noise.

Results

By means of a new geometrically motivated concept we find for the stationary probability density a WKB-like result

$$W_\epsilon(x) = N_\epsilon \, Z_\epsilon(x) \, e^{-\phi(x)/\epsilon} \tag{3}$$

where the nonequilibrium potential $\phi(x)$ is ϵ-independent and $Z_\epsilon(x)$ may depend on ϵ algebraically at most. N_ϵ represents a normalization factor. For $b \leq 2$ the deterministic map $f(x)$ in eq.(1) has stable fixed points at $x = 0.5 \, mod \, 1$ and unstable fixed points at $x = 0 \, mod \, 1$. In the neighbourhood of the stable fixed points $\phi(x)$ has a parabolic shape with curvature $1 - f'(0.5)^2$ and thus in Gaussian approximation we have $N_\epsilon = \sqrt{(1 - f'(0.5)^2)/2\pi\epsilon}$ if we choose $Z_\epsilon(0.5) = 1$. In the neighbourhood of unstable fixed points $\phi(x)$ consists of straight lines whose slopes and matching points both geometrically converge to zero at the rate $f'(0)^{-1}$ as an unstable fixed point is approached . Each straight piece touches an enveloping parabola

with curvature $1 - f'(0)^2$ from above. Analogous results for continuous time systems in more than one dimension have been obtained previously [3]. The prefactor $Z_\epsilon(x)$ in eq.(3) turns out to be ϵ-independent for most x, except for those in the vicinity of the bends of $\phi(x)$ where cusps occur with ϵ-independent heights and widths proportional to ϵ. Outside an $\epsilon^{1/2}$-neighbourhood of $x = 0$ there are plateaus between two cusps. Their heights decrease geometrically with a rate $f'(0)^{-1}$ if $x = 0$ is approached. Within the $\epsilon^{1/2}$-neighbourhood cusps and plateaus merge and the value of the prefactor at $x = 0$ becomes proportional to $\epsilon^{1/2}$. In the expression (3) for the stationary probability density the singularities of $\phi(x)$ and $Z_\epsilon(x)$ compensate each other resulting in a smooth behaviour of $W_\epsilon(x)$ for all x and ϵ. The Figure below shows $\phi(x)$ and $Z_\epsilon(x)$ for $b = 1.4$ and $\epsilon = 10^{-3}$.

Details of the novel geometrical method will be published elsewhere. Within this concept generalisations to more complicated cases as e.g. maps with periodic or chaotic attractors and to non-Gaussian white noise are straightforward.

References
[1] R.Graham, Springer Tracts in Modern Physics 60, Springer Berlin (1973)
[2] P.Talkner, P.Hänggi, E.Freidkin, D.Trautmann, J. Stat. Phys. 48, 231 (1987);
    P.Talkner, P.Hänggi in 'Noise in Nonlinear Dynamical Systems', Vol.2, edited by
    F.Moss and P.V.E.McClintock, Cambridge University Press (1989)
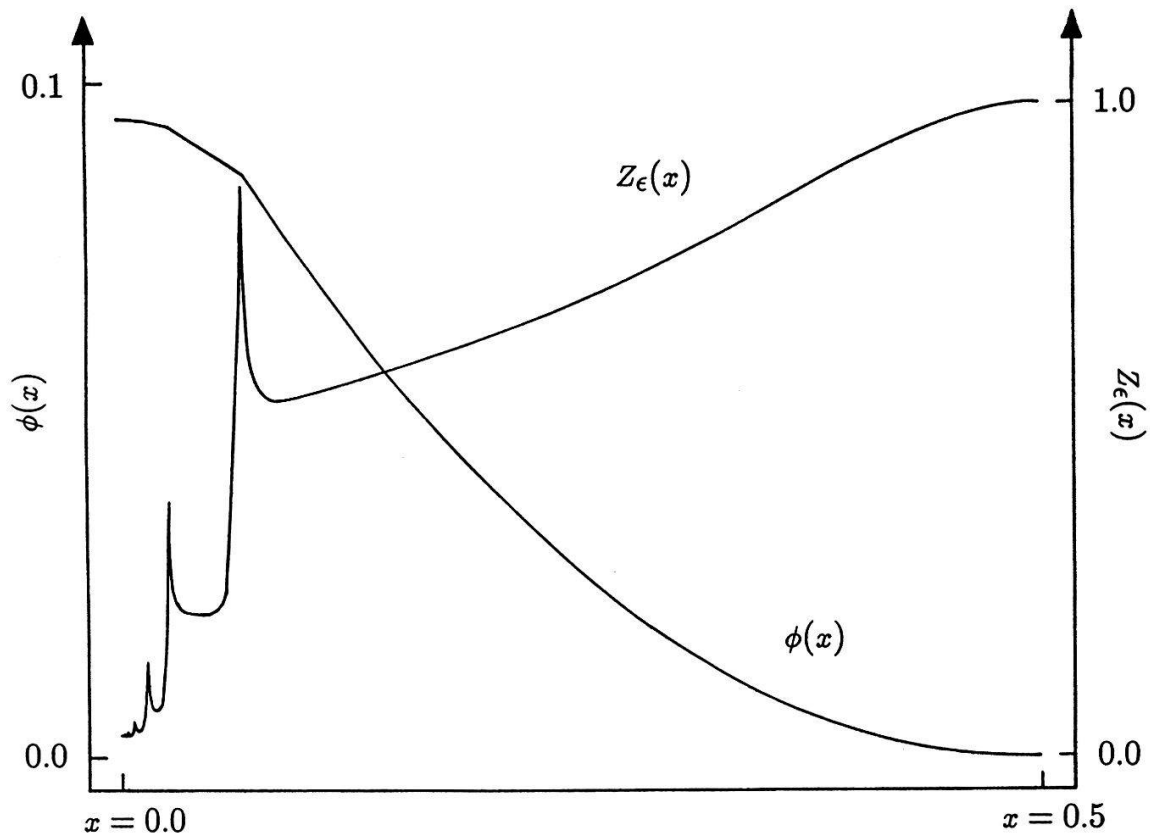[3] R.Graham and T.Tél, Phys. Rev. A 31, 1109 (1985)

Figure: Nonequilibrium-potential $\phi(x)$ and prefactor $Z_\epsilon(x)$. For further discussion see text.

Un modèle de morphogénèse

A.-J. Koch, J. Guerreiro et F. Rothen,
IPE Université de Lausanne, CH–1015 Lausanne

A.M. Turing est le premier à avoir invoqué la diffusion et les réactions chimiques de substances encore inconnues—les morphogènes—pour décrire la morphogénèse et l'embryologie[1]. Il a montré que l'interaction de deux de ces substances pouvait donner naissance à des structures spatio-temporelles capables de briser la symétrie du tissu d'origine et d'induire ainsi des spécialisations locales dans une zone d'abord non différenciée. Ces morphogènes sont aujourd'hui connus. On parle d'activateurs ou d'inhibiteurs qui déclenchent ou contrôlent la croissance d'un tissu particulier.

Nous avons étudié numériquement une équation fonctionnelle proposée par Marzec et Kappraff[2] et qui simule le processus de morphogénèse de la phyllotaxie (arrangement de feuilles sur une tige, des écailles d'un ananas ou d'une pomme de pin, des inflorescences d'une marguerite). La géométrie de ces arrangements est due au fait que les pousses nouvelles apparaissent successivement et à distance angulaire constante—la divergence—sur un anneau situé au voisinage de l'apex de la plante. Cette équation, définie sur le cercle $0 \le x \le 1$, s'écrit

$$F_{k+1}(x) = \lambda F_k(x) + f(x - x_k) \qquad (1)$$

- $F_l(x) \ (= F_l(x + 1))$: concentration totale d'inhibiteur ($l = 1, 2, \dots$)

- x_l ($=$ minimum absolu de $F_l(x)$) est la position de la pousse $l + 1$

- $f(x) \ (= f(x+1) = f(-x))$: concentration d'inhibiteur due à l'apparition d'une pousse en $x = 0$

- $0 \le \lambda \le 1$: paramètre décrivant la dégradation de F_l entre l'apparition des pousses l et $l + 1$

Si le processus décrit par (1) converge vers un état stable, on a, pour un paramètre $0 \le \theta < 1$,

$$\lim_{k \to \infty} [F_{k+1}(x - \theta) - F_k(x)] = 0 \qquad (F_\infty(x) \equiv F(x))$$

Autrement dit, chaque nouvelle pousse ne fait que translater de l'angle θ la concentration d'inhibiteur due à toutes les pousses : θ est la divergence cherchée. Il faut noter cependant que la simplicité de la relation (1) pourrait permettre une interprétation plus générale que celle que nous donnons à partir de la présence de morphogènes.

Dans la figure 1, on donne le profil de $F(x)$ pour un choix particulier de λ et $f(x) = 64\,(x - 0.5)^6$, $(0 \leq x < 1)$. La figure 2 représente, dans le même cas, la valeur de θ pour le même $f(x)$ et plusieurs valeurs de λ. On remarque (c'est un comportement observé pour une large classe de $f(x)$) que, lorsque λ augmente, θ prend essentiellement trois types de valeurs : $1/2$, τ^{-1} (angle d'or) et $1 - 1/(3 + \tau^{-1})$ (angle de Lucas), ce qui correspond aux divergences observées dans la nature. On note que (1) ne converge pas pour toutes les valeurs de λ.

<u>Références</u>

[1]   A.M. Turing, Phil. Trans. Royal Soc. London B <u>237</u>, 37 (1952)

[2]   C. Marzec et J. Kappraff, J. Theor. Biol. <u>103</u>, 201 (1983)
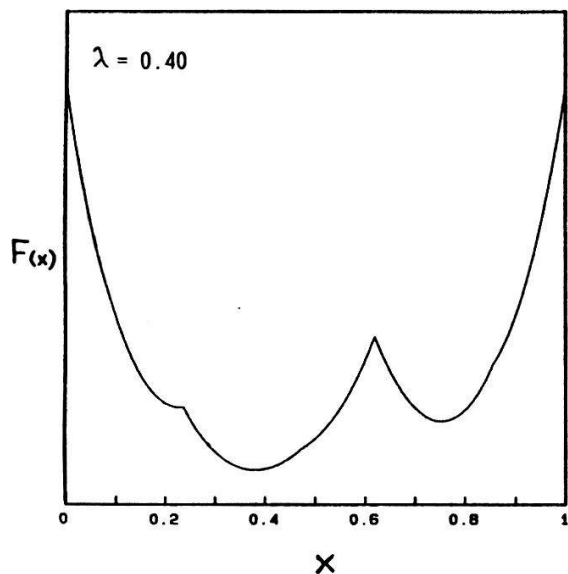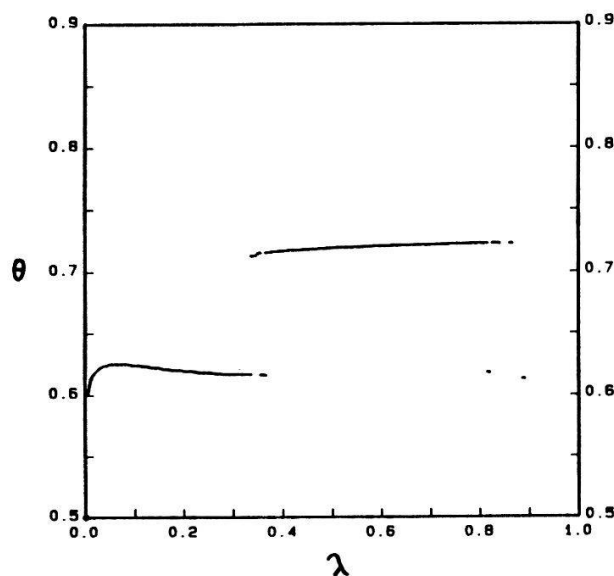

Figure 1

Figure 2